

RAM

● ROBOTICS
AND
MECHATRONICS

CONTROLLING DEFORMATIONS OF A 3D-PRINTED VIBRATING BEAM USING STIFFNESS MODULATION

S. (Sander) Roodink

MSC ASSIGNMENT

Committee:

prof. dr. ir. G.J.M. Krijnen
A.P. Dijkshoorn, MSc
dr. ir. F. Califano
dr. ir. J.P. Schilder

November, 2020

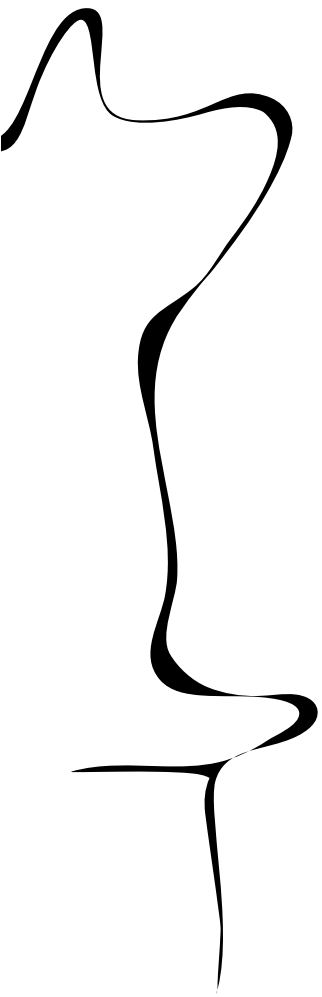
055RaM2020
Robotics and Mechatronics
EEMCS
University of Twente
P.O. Box 217
7500 AE Enschede
The Netherlands

UNIVERSITY
OF TWENTE.

TECHMED
CENTRE

UNIVERSITY
OF TWENTE.

DIGITAL SOCIETY
INSTITUTE



Contents

1	Introduction	1
1.1	Portwings project	1
1.2	Problem Statement	1
1.3	Related work	2
1.4	Research objective	3
1.5	Report Structure	4
2	Analysis	5
2.1	Variable stiffness actuation	5
2.2	Energy-based control	9
2.3	Conclusion	12
3	Design	13
3.1	Design requirements	13
3.2	Embedded 3D-printed strain sensors	13
3.3	Stiffness actuation	18
3.4	Control	22
3.5	Conclusion	29
4	Implementation	31
4.1	Fabrication & Assembly	31
4.2	Experimental structure	35
4.3	Conclusion	38
5	Experimental Results	39
5.1	Characterization of the sensors	39
5.2	Dynamic behaviour of the beam	42
5.3	Validation by video	44
5.4	Effect of damping-injection	48
5.5	Adaptability using control timing	51
5.6	Conclusion	53
6	Discussion & Conclusion	55
6.1	Discussion	55
6.2	Conclusion	56
6.3	Future work	57
A	Euler-Bernoulli beam theory assumptions	59

B Tables of eigenfrequency change by axial load	60
C 20-Sim code	61
D CAD drawings	63
E Damping of a beam by parametric stiffness	66
E.1 1 Degree of Freedom approximation cantilever	66
E.2 Parametric stiffness	66
E.3 Harmonic balancing	67
F Amplifier circuit	69
Bibliography	70

1 Introduction

This master thesis is written for the master Systems and Control directed to Robotics and Mechatronics (RaM) at the University of Twente.

The research is done in context of the Portwings project. One of the project goals is to control the variable stiffness of a mechanical bird wing. To achieve this the curvature can be measured with embedded sensing in advanced fabrication techniques (3D-printing). The 3D-printing research is accommodated under the RaM-chair in the NIFTy-group.

This report explains the steps which have been made to investigate different topics contributing to a closed-loop controlled bird wing.

1.1 Portwings project

The PortWings Project is working on flapping flight systems [University of Twente, 2020]. Not only is this project dedicated to understanding how birds fly, but also to creating flapping-wing robots. The Robird (figure 1.1) has been partly developed at the University of Twente, this has led to the Portwings project. The Robird is a mechanical bird that can stably fly at 80 km/h using a flapping motion. At this moment, the Robird is an open-loop system and has to be controlled by a pilot. The Robird is also unable to take off on its own and its flapping motion is symmetrical, therefore steering is done by the tail.

To improve the Robird, a closed-loop control system could be implemented. In this way the bird becomes multi-modal, it can fly at different velocities, take off, land and can adapt to external variables. To get a closed-loop flapping motion, the sensing, actuation and control needs to be studied, designed, implemented and tested.



Figure 1.1: State-of-the-art mechanical bird called the 'Robird', which is able to fly with a pilot. ©Aerium and Clear Flight Solutions

1.2 Problem Statement

Recently it has become possible to 3D-print multi-material structures with varying physical properties [Nassar et al., 2018]. An example that can be printed in principle is a robotic bird wing. Some of the materials which are available for 3D-printing are flexible materials, fiber-reinforced filaments, (flexible) conductive materials and multi-material prints. Using fused deposition modeling (FDM), sensors can be embedded in flexible structures. At the RaM-chair capacitive and resistive sensors are already being investigated [Schouten et al., 2020]. Using these new technologies, new challenges arise. Amongst others, these sensors tend to be sensitive to creep and drift, furthermore they could behave non-linearly and have a hysteresis [Kosmas et al., 2020]. This makes that the 3D-printed sensors are hard to characterize and apply.

Still, these sensors can be very useful. They can be embedded in the wing, so the sensors do not have to be added to the wing in a post-fabrication step. Furthermore, there is large degree of freedom with respect to the packaging and placement. Embedded sensors will influence aerodynamic shape of the wing less than added external sensors.

Looking at an example in nature, birds can use proprioception to sense the position of their wings, proprioception is the sense of self-movement [Han et al., 2016]. A beam with multiple embedded sensors can be seen as a simplified mechanical bird wing. Even though it is hard to characterize, embedded sensors can be used as input to control a structure.

In a bird wing morphing occurs during flight, which is described in [Douglas et al., 2015]. Morphing can be done by varying the stiffness and angle of the bone hinge joint. If a mechanical bird wing can actively vary the stiffness of the wing, then it would allow for varying flapping patterns during flight.

Desired is to vary the stiffness of the wing during flight, a closed-loop control system is proposed. Controlling the deformation of the wing will increase the flying capability of the mechanical bird. The proposed control will be energy-based, because this methodology can allow complex systems to be controlled properly. The proposed control is suitable for controlled interaction with the environment, for instance the air.

To close the loop, all different aspects should be connected. The embedded sensors, variable stiffness actuator and the control loop should be designed, combined and tested.

1.3 Related work

Before research questions can be defined, relevant theory and research have to be investigated. The Robird can be enhanced by combining theory on 3D-printed beams with embedded sensors, variable stiffness modulation, and energy-based control into a single experimental setup. Relevant literature regarding this thesis involve: theories for deforming beams, simulation models for deforming beams, types of stiffness modulation, (conductive) 3D-printed structures, and models of energy-based control.

1.3.1 3D-printed beam with embedded sensors

3D-printed thermoplastic could reduce the structural weight compared to composite or lightweight metal alloys, making it potentially favorable for wing structures. In the work of Pecho [Pecho et al., 2019] the weight - load distribution relation of a UAV (unmanned aerial vehicle) wing is researched. The weight - load distribution relation of a 3D-printed wing is competitive against composite materials and light metal alloys, making it a suitable choice for the Robird as well.

Not only the weight of a 3D-printed structure is of interest. Using multi-material printers, an electrically conductive material can be printed into a non-conductive structure. The conductive material can be printed as a piezo-resistive strain sensor. A differential piezo-resistive sensor setup, as described by [Schouten et al., 2020], can improve the linearity of the sensors to be used for the curvature measurement of a structure. The dynamic performance of a differential piezo-resistive sensor printed into a beam is analysed in the work of Maurizi [Maurizi et al., 2019]. This paper proves that the piezo-resistive sensor can capture dynamic behaviour up to 800Hz. The sensors are found to be linear in the linear-response region of the structure. However, Schouten concludes that the sensors have non-linearities. Those non-linearities can decrease the accuracy of the sensors, this limitation must thus be addressed in the following research.

1.3.2 Variable stiffness modulation

Many technologies are already using variable stiffness solutions, often applied in soft robotics [Sun et al., 2020]. Those variable stiffness solutions are studied by Melandri [Melandri et al., 2020]. A literature study is conducted on an experimental structure, which can vary the stiffness of a simplified wing. In their work, two experimental setups are validated, one mechanism with sliding segments and the other system is using a rotary movement (see figure 1.2). Both systems did work, however the tests are performed with a static stiffness, therefore more research should be done focusing at the actuation and working in continuous time.

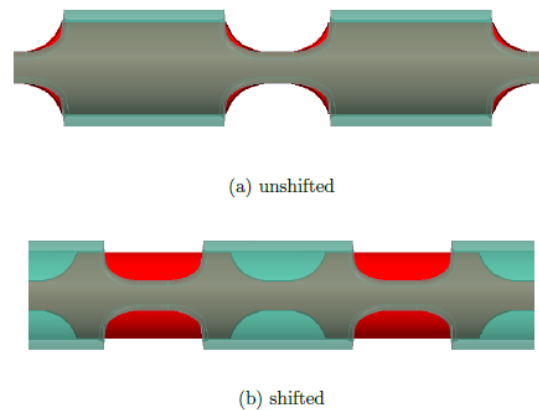


Figure 1.2: The sliding segment model of [Melandri et al., 2020]

Another variable stiffness solution is using an axial load to stiffen or soften the simplified wing. The effect of an axial load on a vibrating beam is studied in the book of Rao [Rao, 2017]. However, this is done for a supported-supported beam model whereas a wing can be modelled like a fixed-free beam. This theory should be developed and tested.

1.3.3 Energy-based control

A beam can be modelled using the Euler-Bernoulli beam theory, see chapter A. This partial differential equation can be written in a more structured way, which plays a major role in the control design. A proposal is made to explicitly study the variation of energy in the beam, this can be done using the port-Hamiltonian (pH) model. This model is also used in the work of [Malzer et al., 2019]. In this research the pH model is used to develop a dynamic controller for an Euler-Bernoulli beam actuated by a pair of piezoelectric patches. The article is concluded with simulations. Experiments are not conducted in this work. Therefore a setup should be built to continue this research.

1.4 Research objective

The scope of this work will be measuring the deformation of a beam using embedded sensors and indirectly manipulating this deformation using an energy-based control loop. The loop will control this deformation by altering the stiffness of the beam.

The research questions of this Master Thesis are:

1. *How can stiffness variations of a beam be influenced?*
2. *How can 3D-printed embedded sensors be used to determine the flapping dynamics?*
3. *What beam behaviour (modifications) can be obtained by using controlled beam stiffness variations?*

4. *Can port-Hamiltonian modelling be used to design a stabilising control law for flexible beams and how can this be achieved?*

Answering these questions is the first step to understand and fabricate an actively controlled bird wing. The wing will be simplified to a beam, which allows for simple and accurate modelling. To actively control a bird wing via a closed-loop system, control input and output signals are required. Sensors are implemented in the wing to measure the bending of the beam and serve as input. This input will control the stiffness of the beam accordingly. In order to control the bird-wing system via this method, the wing must first be stabilized. If damping is introduced via a control-loop, the system stability can be increased [Ortega et al., 2001]. Damping is thus proposed as the method to stabilize the system. Preferred is to get to critical damping by controlling the system. To get a better understanding of these aspects listed above, a test setup will be designed and tested.

Therefore, three sub-objectives are formulated:

- Design and test a prototype 3D-printed beam with embedded sensors, allowing the modelling of the wing and measuring a controller input.
- Design a variable stiffness actuator for the experimental beam set-up, which translates the control output to a change in effective stiffness.
- Design a controller using an energy-based method to stabilize the system.

The research is starting off with exploring related work. In the next step, different beam bending theories will be analysed. This step gives information regarding the bending behaviour of static and dynamic beams. Using this information, the variable stiffness modulation is analysed. Another analysis is done on 3D-printed sensors and flexible structures. The stiffness modulation by energy-based control is the last part of this section. Here, the dynamics of beam are the basics of this topic, and are important for the stiffness modulation. Before a control-loop can be analysed, the method of stiffness modulation should be known. This is due to the fact that the method determines how the stiffness modulation enters the energy equation.

After the analysis, the design process is being described. The different design methods are being divided into the following subjects: The 3D-printed design with additional electric circuits, variable stiffness mechanism and the control-loop. These different designs should be connected to each other, which is ensured in the experimental setup. Subsequently, this setup is analysed and validated. The different experiments are being discussed and concluded afterwards.

1.5 Report Structure

Chapter 2 gives an overview of the design challenges, initially focusing on the sub-research topics and FDM 3D-printed structures. But also on which questions arise when multiple topics are being combined.

Chapter 3 describes the design of the 3D-printed beam, variable stiffness mechanism and control loop.

Chapter 4, considers the implementation. In this chapter, the complete setup is reviewed and the experimental strategy is introduced.

Chapter 5 will focus on the experimental results: characterization of the sensors, dynamic behaviour of the beam, validation by visual recording, efficiency of damping-injection and adaptability using control timing.

In the final Chapter the results will be concluded and discussed.

2 Analysis

To answer the research questions the stiffness actuation and energy-based control are analyzed. The first requirement is understanding how the stiffness of the beam can be modified. If the stiffness can be varied, the behaviour of the beam can be adjusted to the desired movement. Secondly, the stiffness actuation must be controlled, which can be done via an energy-based control method.

2.1 Variable stiffness actuation

First, the variable stiffness actuation is discussed. This is the concept of changing the effective stiffness of a beam. The stiffness of the beam can be varied by applying an axial load, which is proven in [H. Jayasinghe, 2013].

2.1.1 Longitudinal load induced softening

Although it is known that axial load influences the effective stiffness of a beam, the exact relationship between these two needs to be analysed. This is required in order to accurately control the effective stiffness through the axial load. If a defined critical axial load is applied on a beam it buckles. Right before buckling, longitudinal load induced softening occurs. This means that the stiffness of the beam decreases. Understanding longitudinal load induced softening can lead to finding the exact relationship between the axial load and stiffness of the beam. To understand what is happening in the deforming beam during longitudinal load induced softening, the Euler-Bernoulli beam model is introduced in this section. This beam theory is a computationally efficient approximation of a slender deforming beam. Despite the simplicity, the approximation is considered to be sufficiently accurate. This is shown in the background information in A.

To get to the Euler-Bernoulli beam model, first a free body diagram has to be drawn. This is shown in figure 2.1. The beam is modelled as small segments which can have a deflection in the y-direction, this method is from the work of [Rao, 2017].

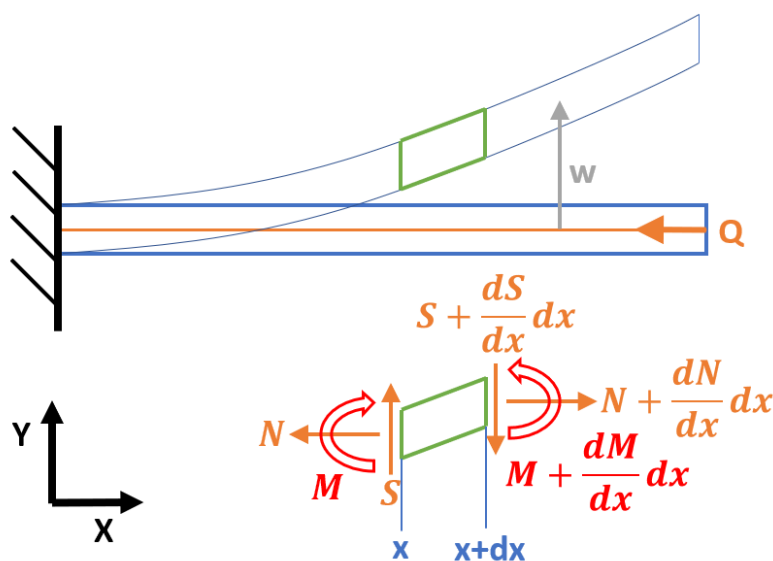


Figure 2.1: Free body diagram of a section of a cantilever beam with an applied axial force

From the free body diagram the force and moment equations are defined. The forces in x and y -direction are important, as well as the moment around the origin.

$$\begin{aligned}\sum F_x &= 0 \\ &= N + \frac{dN}{dx} dx - N \\ \rightarrow \frac{dN}{dx} &= 0 \\ \rightarrow N(x) &= -Q\end{aligned}\tag{2.1}$$

with N the force in x -direction.

$$\begin{aligned}\sum M_z &= 0 \\ &= M + \frac{dM}{dx} dx - S \cdot dx + Q \cdot \frac{dw}{dx} dx - M \\ \rightarrow S(x) &= \frac{dM}{dx} + Q \cdot \frac{dw}{dx}\end{aligned}\tag{2.2}$$

with S being the force in y -direction, Q the applied axial load, and w is the displacement of the beam in y -direction

$$\begin{aligned}\sum F_y &= \rho \cdot A \cdot \frac{d^2 w}{dt^2} dx \\ &= -\frac{dS(x)}{dx} dx\end{aligned}\tag{2.3}$$

where ρ is the density of the beam, A is the intersection area of the beam

By substituting equation 2.2 into equation 2.3, the Euler-Bernoulli beam theory is derived including the axial load:

$$\rho A \frac{\partial^2 w}{\partial t^2} + \frac{\partial^2 M}{\partial x^2} + Q \cdot \frac{\partial^2 w}{\partial x^2} = 0\tag{2.4}$$

When $M = EI \cdot \frac{\partial^2 w}{\partial x^2}$ and $\rho A = \mu$ are substituted into the equation:

$$\mu \frac{\partial^2 w}{\partial t^2} + EI \frac{\partial^4 w}{\partial x^4} + Q(t) \frac{\partial^2 w}{\partial x^2} = 0\tag{2.5}$$

With μ the linear mass density, and EI the flexural rigidity. This equation includes the Euler-Bernoulli dynamic equations, with an added term: the axial load. This equation is called the free vibration equation.

2.1.2 The correlation between the eigenfrequency and the stiffness of the beam

Two different methods of loading the beam in an axial direction are checked, the Beck and Euler type. The difference between these methods is the axial load angle. In the Euler-type softening the load is always parallel to the x -axis, while in the Beck-type softening load will be parallel to the curvature of the beam, which is called a 'following load'. This is shown in figure 2.2. The Beck-type softening will change the stiffness differently than the Euler-type softening.

Based on longitudinal load induced softening and Beck- or Euler-type softening, it still not possible to see how the stiffness of the beam is behaving exactly. There is a strong correlation between the beam's effective stiffness and its eigenfrequency. Quantifying stiffness by using the eigenfrequency allows for effective evaluation of the impact of Beck- or Euler-type softening.

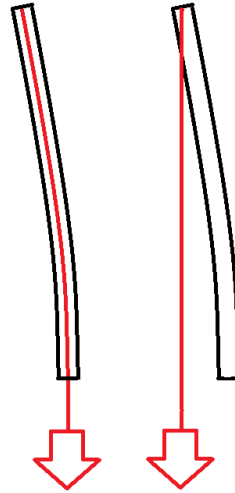


Figure 2.2: Cantilevered beam deformation (A) Beck-type (follower loading) (B) Euler-type (vertical axial loading)

To find possible solutions of the free vibration equation 2.5 we assume the following equation cited from [T. Iwatsubo, 1972], see equation 2.6. In this equation the viscous damping is included in the setup. This is not done in equation 2.5.

$$EI(t) \frac{\partial^4 w}{\partial x^4} + Q(t) \frac{\partial^2 w}{\partial x^2} + C(t) \frac{\partial w}{\partial t} + m(t) \frac{\partial^2 w}{\partial t^2} = 0 \quad (2.6)$$

With EI the flexural rigidity, $Q(t)$ the axial force, $C(t)$ the viscous damping coefficient and $m(t)$ the mass of the beam per unit length. If the time axis is divided into small intervals Δt and the coefficients are constant. Equation 2.6 becomes the partial differential equation with constant coefficients:

$$EI_i \frac{\partial^4 w}{\partial x^4} + Q_i \frac{\partial^2 w}{\partial x^2} + m_i \frac{\partial^2 w}{\partial t^2} + C_i \frac{\partial w}{\partial t} = 0 \quad (2.7)$$

its solution can be written as $w = W(x)T(t)$. This is known as separation of variables. Equation 2.6 can be reduced to the next two differential equations:

$$\begin{aligned} EI_i \frac{d^4 W}{dx^4} + Q_i \frac{d^2 W}{dx^2} - m_i \omega_i^2 W &= 0 \\ \frac{d^2 T}{dt^2} + 2\zeta_i \lambda_i \frac{dT}{dt} + \omega_i^2 T &= 0 \end{aligned} \quad (2.8)$$

With $C_i/m_i = 2\zeta_i \lambda_i$

To solve the eigenfunctions W_i from the first equation of 2.8, the viscous damping is not used. Therefore this first equation can also be used to find the eigenfrequency from equation 2.5.

The next general solution is used [T. Iwatsubo, 1972]:

$$W_i(x) = A_1 \cos s_2 x + A_2 \sin s_2 x + A_3 \cosh s_1 x + A_4 \sinh s_1 \quad (2.9)$$

where

$$s_1^2 = \frac{-\gamma_i + \sqrt{\gamma_i^2 + 4k_i^4}}{2}, \quad s_2^2 = \frac{+\gamma_i + \sqrt{\gamma_i^2 + 4k_i^4}}{2} \quad \text{with } \gamma_i = \frac{Q}{EI} \quad \text{and } k_i^4 = \frac{m\omega_i^2}{EI}$$

The Beck and Euler type cantilever stability have different boundary conditions. First the Euler type cantilever boundary conditions are given:

$$\begin{aligned}
0 &= w(0, t) \\
0 &= \frac{\partial w(0, t)}{\partial x} \\
0 &= \frac{\partial^2 w(l, t)}{\partial x^2} \\
0 &= EI \frac{\partial^3 w(l, t)}{\partial x^3} + Q(t) \cdot \frac{\partial w(l, t)}{\partial x}
\end{aligned} \tag{2.10}$$

With $\cos \theta \approx 1$, because of the small deformations.

For Beck-type cantilever the boundary conditions are:

$$\begin{aligned}
0 &= w(0, t) \\
0 &= \frac{\partial w(0, t)}{\partial x} \\
0 &= \frac{\partial^2 w(l, t)}{\partial x^2} \\
0 &= \frac{\partial^3 w(l, t)}{\partial x^3}
\end{aligned} \tag{2.11}$$

By substituting the different boundaries into equation 2.9, a coefficient matrix for the used boundary conditions can be formed. From this matrix the determinant is used and set equal to zero, so the eigenfrequencies can be solved. The Euler-type determinant of the coefficients is:

$$\begin{aligned}
\det_E &= s_1 s_2^5 + s_1^5 s_2 - \gamma_i s_1 s_2^3 + \gamma_i s_1^3 s_2 + 2s_1^3 s_2^3 \cos(l s_2) \cosh(l s_1) + s_1^2 s_2^4 \sin(l s_2) \sinh(l s_1) \\
&\quad - s_1^4 s_2^2 \sin(l s_2) \sinh(l s_1) + \gamma_i s_1 s_2^3 \cos(l s_2) \cosh(l s_1) - \gamma_i s_1^3 s_2 \cos(l s_2) \cosh(l s_1) \\
&\quad - 2\gamma_i s_1^2 s_2^2 \sin(l s_2) \sinh(l s_1)
\end{aligned} \tag{2.12}$$

The Beck-type determinant of the coefficients is:

$$\begin{aligned}
\det_B &= s_1 s_2^5 + s_1^5 s_2 + 2s_1^3 s_2^3 \cos(l s_2) \cosh(l s_1) + s_1^2 s_2^4 \sin(l s_2) \sinh(l s_1) \\
&\quad - s_1^4 s_2^2 \sin(l s_2) \sinh(l s_1)
\end{aligned} \tag{2.13}$$

2.1.3 Static eigenfrequency approximation

The static eigenfrequencies can be approximated using the the Beck and Euler-type determinant defined in the section above. The following beam properties are used to determine the determinant:

Value	unit	Type
0.300	m	Length (chapter 3.2.1)
0.0150	m	Width (chapter 3.2.1)
0.0005	m	Height (chapter 3.2.1)
861	MPa	Youngs modulus [Chamil Abeykoon, 2020]
0.0223	kg	Mass
1.5625e-10	kgm ²	Moment of inertia

Table 2.1: Properties of the beam, derived from the final experimental beam. See chapter 4.1.4

Using the determinant of both models, the eigenfrequencies of different axial loads are numerically approximated in Matlab. The results of the Beck and Euler-type beam softening is shown

below in figure 2.3. For the Euler-type softening the critical buckling load is reached before 4 N. This is not the case for the Beck-type softening, the first eigenfrequency increases. The second mode eigenfrequency curves are both decreasing, However the Euler-type eigenfrequency decreases faster than the Beck-type softening.

In this project, the behaviour of the first two eigenmodes are analysed and tested. To check if the complete setup can work in different configurations.

However, when a variable stiffening actuator is used for a wing, the wire should be implemented into the wing, because this does not affect the aerodynamics. Furthermore, the chance of wire related issues like it getting stuck or breaking is decreased. If the wing is slender, the wire shaft is narrow and Beck-type softening theory can be applied. If Euler-type beam softening is used, the wire cannot be implemented in the wing. Therefore Beck-type softening is favored.

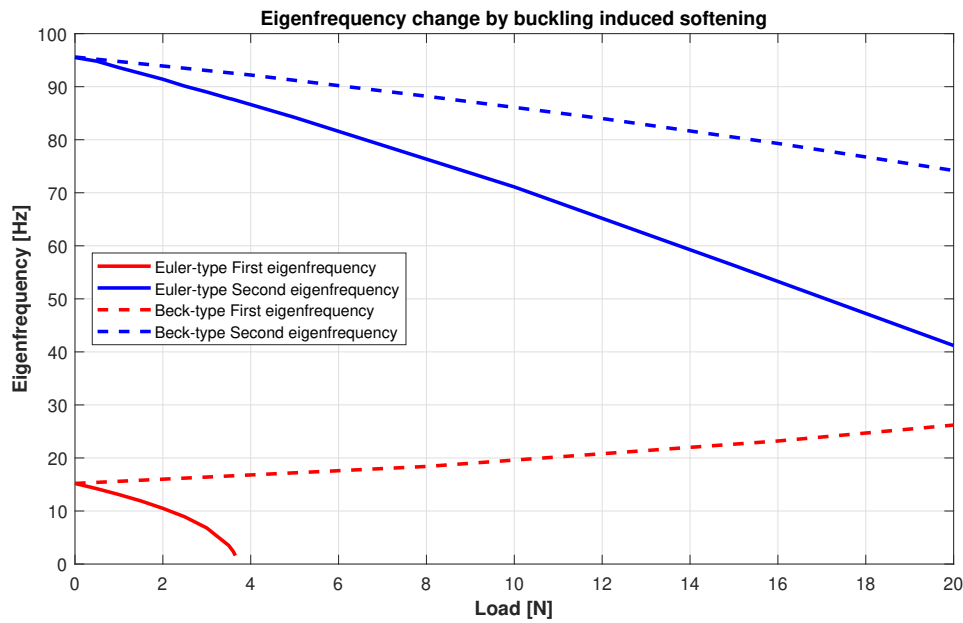


Figure 2.3: Eigenfrequency change by longitudinal load induced softening (tables in Appendix B)

2.2 Energy-based control

The idea is to use energy flows to control a physical system. In this thesis the deforming beam is the system which is to be controlled. This will start with the Euler-Bernoulli beam theory and using the Port-Hamiltonian model an energy balance equation to control the deforming beam is found.

2.2.1 Dynamic beam theory

In this project a slender beam is used, so the Euler-Bernoulli beam theory in chapter A can be used as framework. From the Euler-Bernoulli beam theory the dynamics of the beam can be found. This is already done, and is shown in equation 2.5. The equation is shown again:

$$\mu \frac{\partial^2 w}{\partial t^2} + EI \frac{\partial^4 w}{\partial x^4} + Q(t) \frac{\partial^2 w}{\partial x^2} = 0 \quad (2.14)$$

Here x is the position along the beam, E is the elastic modulus, I is the second moment of area of the cross-section, w is the displacement of the beam in the x -axis, μ is the linear mass density, t is the time and Q is the distributed load on the beam in the z -axis. It is assumed that the beam is made of a homogeneous material and the cross-section is constant, which

means EI is constant. To make the equation more convenient to use, the axial load is rewritten: $Q(t) \frac{\partial^2 w}{\partial x^2} = EIk \frac{\partial^2 w}{\partial x^2}$. So the rewritten equation becomes:

$$\mu \frac{\partial^2 w}{\partial t^2} + EI \frac{\partial^4 w}{\partial x^4} + EIk \frac{\partial^2 w}{\partial x^2} = 0 \quad (2.15)$$

This equation is rewritten:

$$w_{tt} + \mu EI w_{xxxx} + EIk w_{xx} = 0 \quad (2.16)$$

with $\frac{\partial^4 w}{\partial x^4} = w_{xxxx}$ and $\frac{\partial^2 w}{\partial t^2} = w_{tt}$. $q(t)$ is assumed to be distributed equally over the beam, so this is not dependent of x . This equation is the base for the energy-balance equation.

2.2.2 Implementing beam theory by Port-Hamiltonian modeling

To track the variation of energy in the beam, the Port-Hamiltonian model is used. The Hamiltonian is a mechanical energy equation, which is the sum of the potential energy and the kinetic energy. The potential energy is stored in the elastic deformation of the beam and hence in the derivative of the displacement (curvature of the beam). The kinetic energy is stored in the velocity of the beam, which is defined beforehand: $w_t(x, t) = \frac{p(x, t)}{\mu}$. The potential and kinematic energy density over the length of the beam is:

$$\begin{aligned} U_{\text{Potential}} &= \frac{1}{2} EI w_{xx}^2 \\ U_{\text{Kinetic}} &= \frac{1}{2} \mu w_t^2 = \frac{1}{2} \frac{p^2}{\mu} \end{aligned} \quad (2.17)$$

To find the total energy of the beam, the energy density is integrated over the beam. This results in the Hamiltonian shown in equation 2.18.

$$H(t) = \frac{1}{2} \int_0^L \left(\frac{p^2}{\mu} + EI w_{xx}^2 \right) dx \quad (2.18)$$

This expression suggests to choose new variables for the model, i.e. the energy variables are the momentum p and the curvature w_{xx} . The co-energy variables are associated with the energy variables. The co-energy variables can be derived from the functional derivatives of the Hamiltonian with respect to the energy variables. The co-energy variables are the velocity (w_t) and stress ($EI w_{xx}$):

$$\begin{aligned} \frac{\delta H}{\delta p} &= \delta_p H = \frac{p}{\mu} = w_t \\ \frac{\delta H}{\delta w_{xx}} &= \delta_{w_{xx}} H = EI w_{xx} \end{aligned} \quad (2.19)$$

The co-energy variables are implemented in the Port-Hamiltonian model [Folkertsma and Stramigioli, 2017]:

$$\begin{pmatrix} \dot{w}_{xx} \\ \dot{p} \end{pmatrix} = \begin{pmatrix} 0 & \frac{\partial}{\partial x^2} \\ -\frac{\partial}{\partial x^2} & 0 \end{pmatrix} \begin{pmatrix} \delta_{w_{xx}} H \\ \delta_p H \end{pmatrix} \quad (2.20)$$

From the Port-Hamiltonian model is stated that:

$$\begin{aligned} \dot{w}_{xx} &= \frac{\partial}{\partial x^2} \delta_{w_p} H \\ \dot{p} &= -\frac{\partial}{\partial x^2} \delta_{w_{xx}} H \end{aligned} \quad (2.21)$$

The derivative of the Hamiltonian is needed to find the conditions under which energy is added or taken from the system. The derivative of the Hamiltonian is shown in 2.22. The variables \dot{w}_{xx}

and \dot{p} are used to find a simplification of the derivative of the Hamiltonian. Because it will be integrated by parts.

$$\begin{aligned}
\dot{H}(t) &= \int_0^L \left(\frac{\delta H}{\delta p} \dot{p} + \frac{\delta H}{\delta w_{xx}} \dot{w}_{xx} \right) dx \\
&= \int_0^L \left(-\delta_p H (\delta_{w_{xx}} H)_{xx} + \frac{\delta H}{\delta w_{xx}} (\delta_p H)_{xx} \right) dx \\
&= -[(\delta_p H) (\delta_{w_{xx}} H)_x]_0^L + [(\delta_{w_{xx}} H) (\delta_p H)_x]_0^L \\
&= EI(-w_t(L) w_{xxx}(L) + w_t(0) w_{xxx}(0) + w_{xx}(L) w_{tx}(L) - w_{xx}(0) w_{tx}(0)) \\
&= \partial\Gamma
\end{aligned} \tag{2.22}$$

This balance is only dependent on the time and position derivatives at the boundaries $x = 0$ and $x = L$. This is more convenient and efficient to compute than solving the Euler-Bernoulli differential equations. The balance gives insight in the control method.

2.2.3 Implementing stiffness control in the Port-Hamiltonian cantilever model

The axial load applied on the tip of the beam is distributed through the whole beam. This distributed transversal load is dependent on curvature w_{xx} , gain of the control k and the flexural rigidity EI . Because the load is distributed over the beam, this term is added in the Euler-Bernoulli free vibration equation:

$$w_{tt} + \mu EI w_{xxxx} + EI k w_{xx} = 0 \tag{2.23}$$

The energy and co-energy variables are not changed by the added distributed axial load. However, the interconnection matrix is:

$$\begin{pmatrix} \dot{w}_{xx} \\ \dot{p} \end{pmatrix} = \begin{pmatrix} 0 & \frac{\partial}{\partial x^2} \\ -\frac{\partial}{\partial x^2} + k & 0 \end{pmatrix} \begin{pmatrix} \delta_{w_{xx}} H \\ \delta_p H \end{pmatrix} \tag{2.24}$$

The derivative of the Hamiltonian is shown below and integration by parts is used:

$$\begin{aligned}
\dot{H}(t) &= \int_0^L \left(\frac{\delta H}{\delta p} \dot{p} + \frac{\delta H}{\delta w_{xx}} \dot{w}_{xx} \right) dx \\
&= \partial\Gamma + EI k \int_0^L w_t w_{xx} dx
\end{aligned} \tag{2.25}$$

The derivative of the Hamiltonian should be negative, $\dot{H} < 0$, to have damping-injection, which is wanted to have a stable control-loop. Therefore equation 2.25 will be rewritten to:

$$\dot{H} = \partial\Gamma + EI k \int_0^L w_t w_{xx} dx < 0 \tag{2.26}$$

With:

$$\partial\Gamma = EI(-w_t(L) w_{xxx}(L) + w_t(0) w_{xxx}(0) + w_{xx}(L) w_{tx}(L) - w_{xx}(0) w_{tx}(0)) \tag{2.27}$$

All variables in equation 2.27 are dependent on the boundaries conditions. The studied model is a cantilever beam. In this case the boundaries of the beam are at $x = 0$ and $x = L$. The beam is excited to first or second mode, by moving $x(0)$ in the Y-direction. At $t = 0$, $x(0)$ is clamped, therefore $w_t(0) = w_{tx}(0) = 0$. So all boundary conditions at $x(0)$ are zero. At the tip of a cantilever the curvature is always zero. This can also be seen in figure 3.5. therefore

$w_{xx}(L) = 0$. The slope of $w_{xx}(L)$ is also zero (again see figure 3.5), so $w_{xxx}(L) = 0$. Knowing this $\partial\Gamma$ will become zero. Equation 2.26 is chosen to be negative and EI is constant, therefore k is :

$$k = - \int_0^L w_t w_{xx} dx \quad (2.28)$$

Equation 2.28 is the control design, which is used in this work.

2.3 Conclusion

Using the Euler-Bernoulli beam theory and the port-Hamiltonian Model a control law is found, which can apply damping-injection on a vibrating beam with small deformations. This can be used by designing a setup, so the analyses can be validated in practice.

3 Design

This chapter treats the design choices which are made to have a working setup. The design is divided into three sections: Embedded 3D-printed strain sensors, the variable stiffness modulation, and the implementation of the Hamiltonian control-loop. But first the requirements are established.

3.1 Design requirements

The requirements are established from the information given in the introduction 1 and the analysis 2. As there are limited time and resources, the requirements are ranked using the MoSCoW (Must, Should, Could, Will not) criteria to be able to prioritize between the requirements. The prioritisation is based on the following question: "Is this requirement needed to stabilize a vibrating 3D-printed beam using stiffness modulation?"

The design of the 3D printed beam ...

- ... must have embedded sensors, which can measure the curvature (section 1.3.1).
- ... must allow an attachment to modulate the stiffness (section 1.3.2).
- ... should have dimensions such that the first two modes can be measured (section 2.1.3).
- ... should handle small deformations (section A).
- ... could use a material which can be fabricated easily (section 1.3.1).

The design of the stiffness modulator ...

- ... must be controlled continuous real-time (section 1.3.2).
- ... must change the effective stiffness by a distributed load (section 2.1.1).
- ... could be implemented in the bird wing (section 2.1.3).

The design of the control-loop ...

- ... must be controlled using energy variables (section 2.2.2).
- ... should be stabilized by damping-injection (section 2.2.3).
- ... should control the first two eigenmodes (section 2.1.3).
- ... could decrease the damping of the beam (section 2.2.3).

3.2 Embedded 3D-printed strain sensors

The beam for this project is printed using fused deposition modelling (FDM), shown in figure 3.1. This type of printing is used because it is affordable, easy accessible, and multi-material printing is possible. Various 3D-printers are available in the lab, not all of them capable of printing the beam as is required.

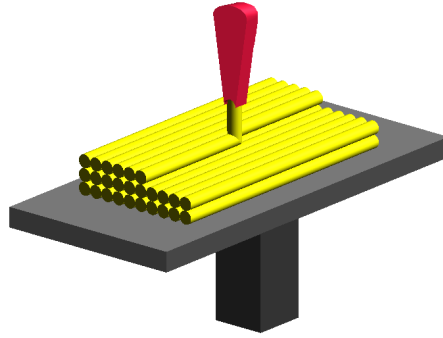


Figure 3.1: Schematic drawing of used deposition modelling printing [3Dilla, 2020]

The beam deformation is measured using embedded strain sensors. In this section, the design choices for these embedded strain sensors are elaborated. As tested by [Schouten et al., 2020], a good way to measure the curvature of a 3D-printed structure, while dealing with the non-linear properties of the material, is using differential strain sensors. Differential measurements increase the linearity of the sensors by compensating ideally for the odd orders of non-linearity.

3.2.1 Beam dimensions

In order to set the dimensions of the beam, multiple factors have to be taken into account. The beam design is dependent on a multitude of factors, including materials and eigenfrequencies. There are also constraints in place on the possible dimensions of the beam, determined by the 3D-printer, strain sensors and experimental setup.

Materials

When printing embedded sensors with FDM it is possible to print a stiff material or a flexible material. There are two parts in the beam, a piezo-resistive part which can be used as strain sensor, and a non-conductive part to create the rest of the beam structure. These two parts should be constructed from materials with similar mechanical properties to ensure uniform behaviour along the beam [Dumstorff et al., 2014]. Not only the uniform behaviour is important, if two similar materials are used, larger stresses around the sensors are avoided [Dumstorff et al., 2014]. There are two material combinations available; the stiffer non-conductive PLA with conductive Proto-pasta [Dijkshoorn et al., 2018], and the softer non-conductive TPU (NinjaFlex) with conductive ETPU [Schouten et al., 2020]. Those materials have different properties in stiffness, flexibility, damping and print quality. The Young's modulus of PLA is around 3.5 GPa [Makeitform, 2020]. For FDM 3D-printing this is a relative high Young's modulus. On the other hand, TPU has a low Young's modulus, which is around 12 MPa [NinjaTek, 2020]. Based on this two prototype-beams are printed, shown in figure 3.2. One is built from PLA with Proto-pasta sensors and one is built from TPU with ETPU.



Figure 3.2: Orange: TPU with ETPU sensor; Blue: PLA with Proto-pasta sensor, which is used for the sensor characterisation in section 5.1

A low damping coefficient is preferred. This is due to the fact that in the experiments, the damping will be analysed. If a beam has a high damping coefficient, it quickly stops vibrating after excitation and yields insufficient data. This makes it difficult to analyse, requiring a low damping coefficient to obtain useful results. The PLA with Proto-pasta beam has a lower damping coefficient than TPU. Besides this, the Euler-Bernoulli beam theory is only applicable for small deformations. Due to its higher elasticity, TPU has significantly higher tip displacement when vibrating, and thus relatively large deformations take place. As a result, PLA with Proto-pasta is the material of choice for the final setup.

Piezo-resistive measurement

Strain sensors are already common in many applications, for instance load cells. The most commonly used strain sensors are metal film strain gauges. When a beam bends, the resistance of the film strain gauge at the convex side of the beam increases. At the same time, the sensor at the concave side of the beam will decrease in resistance due to compression. This is due to the geometrical effect. As shown in figure 3.3, a Wheatstone half-bridge would be an accurate way to measure the curvature in this case [Peter Myler, Leslie M. Wyatt, 1994]. This setup will also be used for the 'Proto-pasta sensors'.

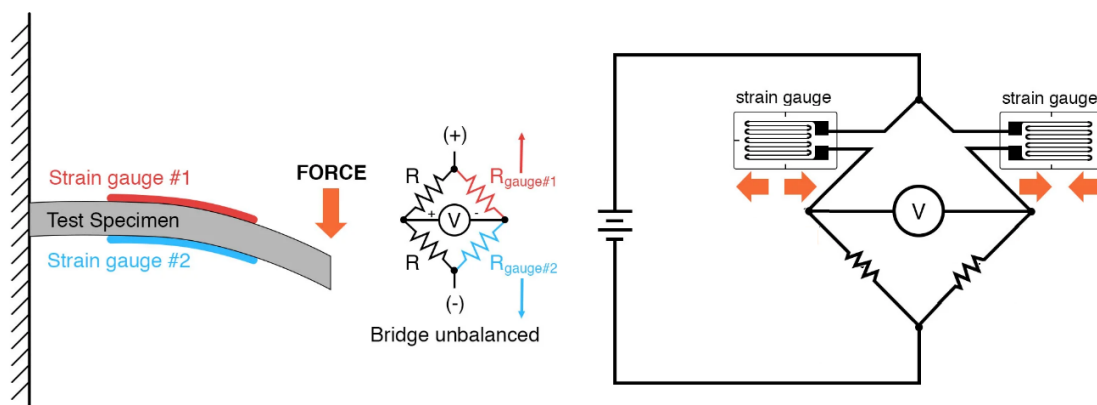


Figure 3.3: Half-bridge metal film strain gauge setup [Tony R. Kuphaldt, 2006]

Strain gauge design

The conductive Proto-pasta is used for the piezo-resistive sensors. In previous work [Maurizi et al., 2019], meandering sensors were used. This meandering increases the total length of the gauge channel; which increases the sensitivity if the cross-sectional area is constant. However,

this also increases resistance, which reduces the sensitivity if it becomes too high. A trade-off is thus made between the length of the gauge and the resistance, with a maximum resistance set at 100 k Ω . By iteration it is found that a meander of four lines with a total length of 100 mm has a resistance around 80 k Ω depending on the printing quality of the sensor and the cross-sectional geometry. This is considered satisfactory for this research.

In FDM-printing the lines can vary in width due to printing quality, which decrease the reliability of the sensor. By printing multiple parallel lines the relative effect of these printing liabilities is reduced. These lines can be printed next to each other and on top of each other to keep the sensor channel compact. After tuning the channel width and height of the sensor, the material was stable and had no defects when the gauge channel had four lines in a 2 x 2 layout with a line width of 0.4 mm and height of 0.2 mm.

In other work, the meandering channels are connected by thicker perpendicular channels. If this thicker channel is printed more lines are printed, which results in a disrupted line. If current flows through a continuously printed line the electric conductivity is homogeneous. If current flows perpendicular through the lines, the electric conductivity changes [Dijkshoorn et al., 2020]. Therefore a curved bridge is chosen to connect the channels. So now the meandering channels are printed in one line.

The sensor will have a total length of 40 mm and is 12 mm thick, including the soldering paths. The first and final sensor design is shown in figure 3.4.

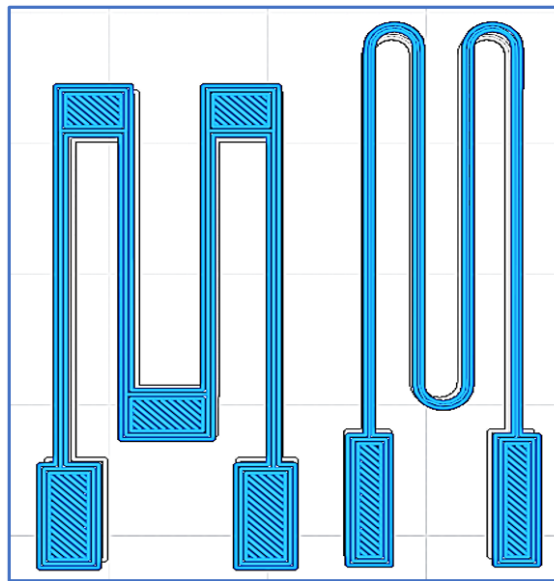


Figure 3.4: (A) First iteration; visible are the non-continuous lines (B) Final sensor design; continuous printing lines

Eigenfrequency

The eigenfrequency of the beam is determined by its material and dimensions. The desired eigenfrequency can be found by looking at the median wing-beat frequency of different birds [Bruno Bruderer, Dieter Peter, Andreas Boldt, Felix Liechti, 2010], the flapping frequencies are between 2 and 17 Hz. The peregrine falcon, which is researched by the PortWings project, has median frequency of 5.1 Hz. As the project aim is to simulate this bird species flight, the eigenfrequency of the beam should be as close as possible to this 5.1 Hz. With the desired eigenfrequency and materials known, the beam dimensions can be determined through FEM

(finite element method) simulations in Solidworks. The minimum height and width are determined based on the following items:

- The variable stiffness wire must be implemented in or around the beam.
- The electrical wires of the strain gauges are implemented into the beam. If the wires are at the normal line of the beam, the wires will affect the beam stiffness the least.
- The strain gauges are embedded into the beam, on both sides of the beam two layers of conductive material are printed, to ensure the sensor will not have an internal misprint. These have a height of 0.4 mm. Because a differential measurement is done two sensors are needed.
- When the beam is removed from the printer, the beam will deform a bit. If the beam is too slender, the beam has an offset curvature in the beam. This is not desired, because the critical buckling load will be decreased. The offset curvature can be reduced by heating the beam in an oven. The residual stress decreases in this process. This process is described in the implementation, chapter 4.1.4.
- When reducing height and width, buckling may become a threat. This threat can be mitigated by adapting the axial load on the beam based on the dimensions.
- The 3D-printer has a bed size of 416 mm (the used 3D-printer is described in chapter 4). 50 mm from the edges was avoided, because the printing quality decreases at the edges. The maximum length of the beam is thus 316 mm.
- The sensors are printed in a meander way, which is 12 mm width (including contact pads). An additional 1.5 mm edge is printed for stability, making the minimum width 15 mm.

In Solidworks the first simulations of a PLA beam are performed with dimensions 200 x 7 x 20 mm, showing a first eigenfrequency of 30 Hz. A slender beam has a lower eigenfrequency than a thicker beam. So, to lower the eigenfrequency closer to the desired 5.5 Hz, the beam is made as slender as possible. The height is decreased to the minimum of 5 mm. The total length of the beam is increased to 315 mm. The first 15 mm of the beam is used to clamp the beam, therefore the effective length is 300 mm. Finally, the width of the beam is also reduced to the minimum 15 mm. Using these new dimensions 315 x 5 x 15 mm, another simulation is run in Solidworks. This yields a first eigenfrequency of 15.3 Hz minimum frequency for the first eigenmode without axial load.

3.2.2 Strain sensor positions

Not only the materials and the differential measurement are important to measure the curvature of the beam. Also the location of the gauges at the beam are important. Because the first two eigenmodes will be analysed, the curvature of those modes are important to find the best location for the strain gauges.

To find the best locations the first and second eigenmode shapes are needed. Because the strain sensors are measuring the curvature, the lateral curvature shape is needed. The lateral displacement shape of a cantilever is calculated using the Matlab script of E. Cheynet [E. Cheynet, 2020]. The lateral curvature shape can be found by differentiating the lateral displacement twice. The result is shown in figure 3.5. In this figure the green vertical lines will be the position of "sensor 1" and the cyan vertical lines is the position of "sensor 2".

To measure the maximum curvature, the sensors should be located at the peaks of the graph. For first mode this is at $x = 0$ and for the second mode this is at $x = 50$. The two sensors are also

shown in the graph, by the vertical green and cyan lines. With those locations also the different modes can be identified. This is used in the control-loop, and explained in chapter 3.4.2.

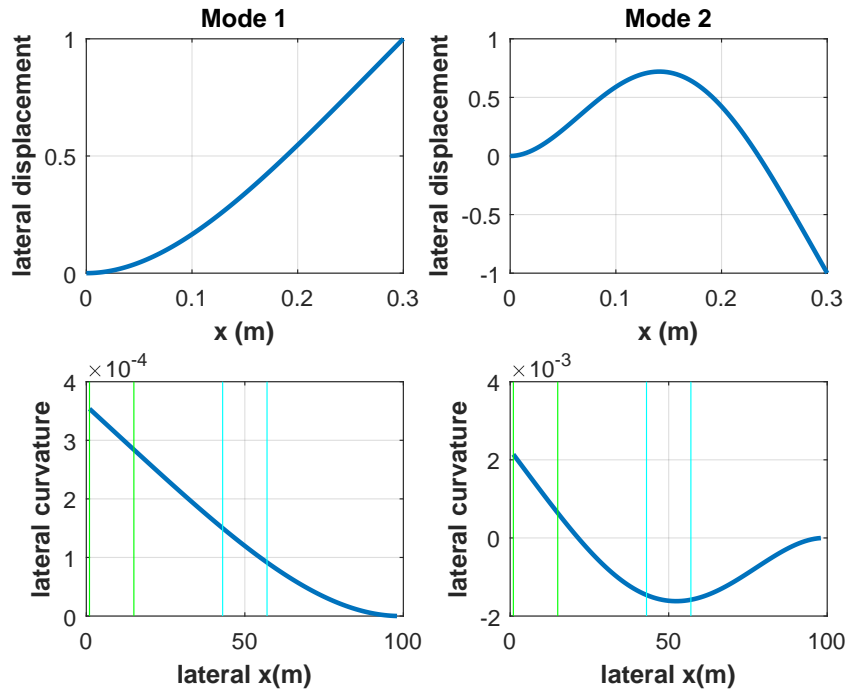


Figure 3.5: Sensor positions targeted to highest curvature for first and second mode. The green vertical lines will be the position of sensor 1 and the cyan vertical lines is the position of sensor 2

3.3 Stiffness actuation

From the variable stiffness actuation analysis in chapter 2 two different longitudinal load induced softening theories can be used to change the stiffness of the beam. The first one which is analysed is the Beck-type softening and the second one the Euler-type softening. This design, is comparable with a tendon actuation, which is lightweight. The weight of a setup is very important the mechanical bird.

3.3.1 Wire through a shaft

To get a correct implementation of the Beck-type softening a wire should be placed on the neutral line of the beam, this can be achieved by incorporating a shaft through the length of the beam. This is shown in figure 3.6. The shaft can directly be built into a slender beam using FDM 3D-printing.

3.3.2 Wire implement by bow wire principle

The second setup which is built and tested is based on the Euler-type softening. This can be seen as a bow, where the wire is the bowstring and the beam the bow itself. Although it comes close to the Euler-type softening, it is not exactly the same due to a force component in the y -direction in the setup, which is not present in the Euler-type formulation. The three different implementations are shown in figure 3.6

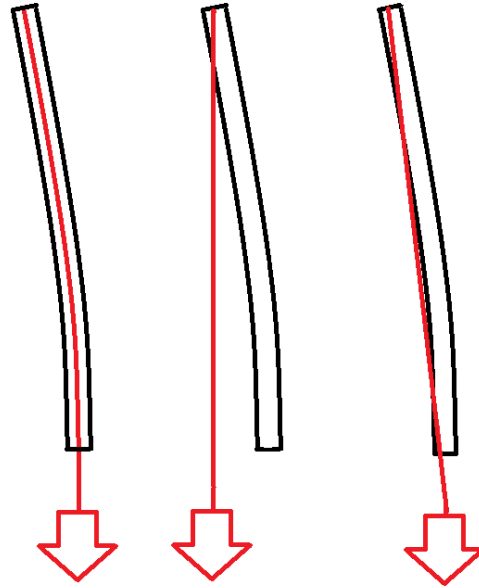


Figure 3.6: beam softening methods (A) Beck-type (B) Euler-type (C) Bow principle

In the analysis the difference between the Euler- and Beck-type softening (see equations 2.10 and 2.11) is visible in the shear force boundary, the difference is:

$$\begin{aligned} 0 &= \frac{\partial^3 w(L, t)}{\partial x^3} \\ 0 &= EI \frac{\partial^3 w(L, t)}{\partial x^3} + Q(t) \cdot \frac{\partial w(L, t)}{\partial x} \end{aligned} \quad (3.1)$$

The first equation is shear force boundary of the Beck-type and the second equation is the shear force boundary of the Euler-type. Shown is, that Euler-type also dependent on the load multiplied with the slope of the beam and not only on the third derivative of the beam. This can be implemented in equation 2.22, the derivative of the port-Hamiltonian model. This results in:

$$-\frac{Q(t)}{EI} w_t(L) w_x(L) - EIk \int_0^L w_t w_{xx} dx < 0 \quad (3.2)$$

This equation can also be implemented into the control-loop which is designed. By using deformation models, $w_t(L)$ and $w_x(L)$ can be approximated. However this is the Euler-type solution. The bow principle is a bit different, instead of using the slope of the free end, the slope of the wire should be used. Therefore the following shear force boundary is proposed for the bow principle:

$$0 = EI \frac{\partial^3 w(L, t)}{\partial x^3} + Q(t) \cdot \tan^{-1} \frac{w(L, t)}{L} \quad (3.3)$$

This results again in a change of the proposed control equation:

$$-\frac{Q(t)}{EI} w_t(L) \cdot \tan^{-1} \frac{w(L)}{L} - EIk \int_0^L w_t w_{xx} dx < 0 \quad (3.4)$$

3.3.3 Wire tension actuator

The wire tension needs to be adjustable to actively control the stiffness of the beam. The mechanism needs to be able to pull on the wire to create a predetermined level of tension in the

string. This could be done by a winch driven by a DC-motor. In figure 3.7 the angular velocity-torque gradient of a DC-motor is shown. When the angular velocity is zero, the torque is at its maximum. In this research only the torque is important, because the DC-motor will be stalled during the experiments. To control the stall torque, the current can be limited. The current is linear with the torque of the motor as shown in equation 3.5. Using a pulley the torque will be converted to a force. This force will pull on the wire, which in turn changes the stiffness of the beam. As a result, stiffness of the beam can be changed as desired by using a specific current.

$$M_R = k_M \cdot I_0 \quad (3.5)$$

With M_R the torque of the motor, I_0 is the current which flows through the motor and k_M is the motor constant.

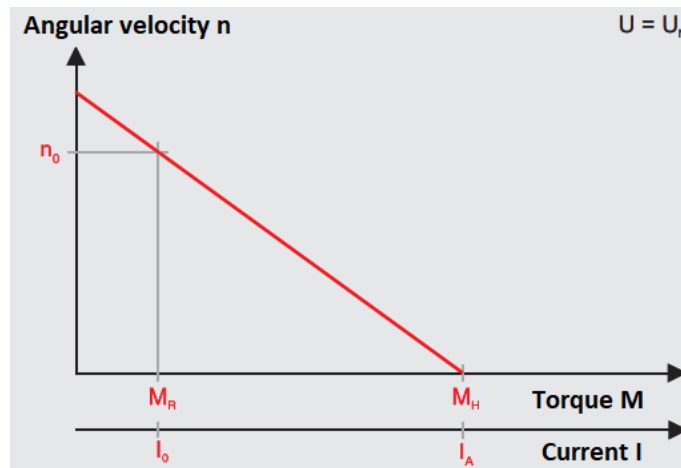


Figure 3.7: Angular velocity vs. torque of a DC motor [Maxon motors, 2014]. In this project the DC motor will be driven at zero angular velocity, at stall

3.3.4 Design of the stiffness modulator

Now all the different components of the modulator can be connected. To get from a current to a modulation in stiffness the following components are needed:



Figure 3.8: Block-diagram of the variable stiffness modulator

The Maxon 142733 DC-motor is used in this project. In previous work [Roodink, 2017] this DC-motor is characterized. In this work, the stalling torque is around 0.15 Nm when the torque-angular velocity line is extended to an RPM of 0.

From the Solidworks simulations of the beam, the critical buckling load is 12 N. This is the maximum load which can be applied on the beam. Knowing the torque and the critical buckling load, the maximal length of the pulley arm can be calculated. Chosen is an arm length of 0.01 m, now the beam could not buckle and the beam will not deform.

$$r = \frac{T}{F} = \frac{0.15}{12} = 0.0125m \quad (3.6)$$

All parameters are known, which means the variable stiffness modulator can be designed using Solidworks. The beam brackets, motor bracket, and pulley are 3D-printed. The drawings are shown in Appendix A. In Solidworks, simulations are done to see the eigenfrequency of the different brackets. The lowest eigenfrequency of the brackets must have a safe margin between the eigenfrequency of the beam to avoid interference resonance. The second eigenfrequency of the beam is 86.2 Hz (experimentally tested in 5.2). So to be safe the lowest eigenfrequency of the brackets should be at least 200 Hz. The build setup is shown in figure 3.9.

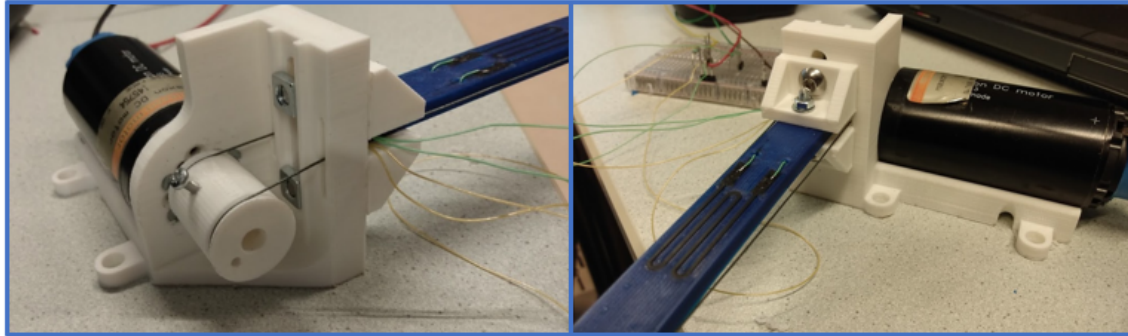


Figure 3.9: Variable stiffness modulator with: The DC motor axle is connected to the pulley by a screw; the bracket is holding the motor and beam at its place; the pulley could easily be changed so the torque arm length is changed; around the pulley the wire is visible

3.3.5 Variable stiffness modulation characterisation

Before the variable stiffness modulator can be used, the setup should be characterised. First, the linear load-current relation will be measured. If this is known, the beam can be actuated to different static loads, to see if the eigenfrequencies change in the way they are calculated in the analyses.

To characterise the stiffness modulation setup, the motor will be driven by a current stair function. The stair function will have a range from 0 A to 2.5 A, with steps of 0.5 A. The output force is measured using a spring scale. Measuring this force is done in two different ways, one is the static load, so when the current is stable. The other measurement is peak force, this peak occurs when the current is changed to the next step. This is measured because in the experimental setup the current will not be static; it will be modulated during the experiment. Therefore this linear force curve is more important than the static load curve. Both curves are shown in figure 3.10.

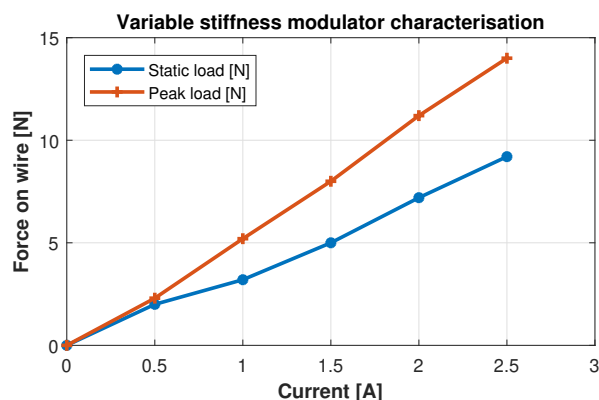


Figure 3.10: Characterisation of the load on the wire

With the maximum of 2.5 A supply current, the 15 N load could almost be reached. This is above the critical buckling load from the Solidworks simulations and the Euler-type softening calculation, see Appendix B. This is happening because the current is set at 2.5 A and the motor controller used in the setup will produce a maximum current of 2 A. Therefore, this motor and pulley can be used to measure the eigenfrequency change, by the wire through the shaft and the bow wire.

3.4 Control

In figure 3.11 the schematic block diagram of the designed controller is shown. First, the signals of the sensors will have to be manipulated to become a useful input for the 'mode checker'. The mode checker is distinguishing the different eigenmodes, and therefore the sensor values can be fitted to the right eigenmode. In this case, there are 2 possible eigenmodes. Both modes have their own curvature and displacement. When the curvature and displacement of the whole beam are known, the control gain can be estimated using the derivative of the Hamiltonian. The control gain will be the input of the stiffness modulator. The block diagram of the controller is implemented in 20-Sim figure 3.12. 20-Sim helps to model dynamic systems and simulate their behaviour. A 20-Sim model can be exported to a C-code using 20-Sim 4C. The different design parts of the control loop are elaborated in this section.

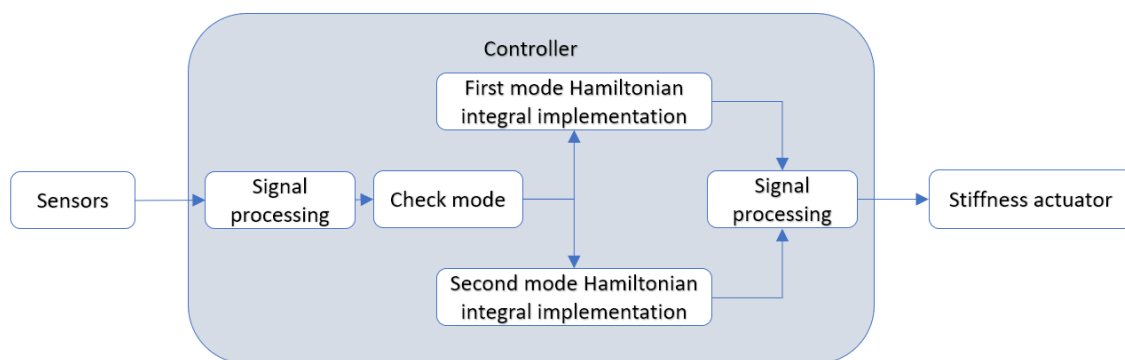


Figure 3.11: Schematic block-diagram of the control-loop

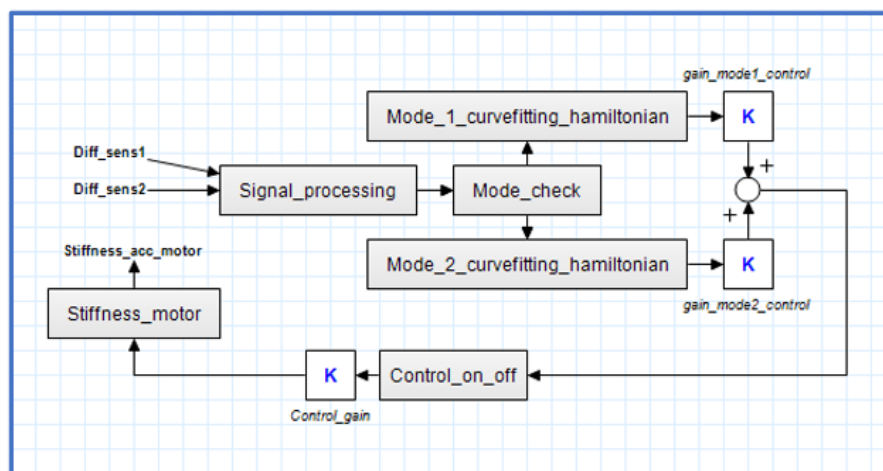


Figure 3.12: 20-Sim model of the schematic block-diagram

3.4.1 Pre-control signal processing

The control loop needs a clean input signal, because the differential of the curvature is used further on in the loop. The reason is explained in section 3.4.3. To prepare the loop, first the offset should be removed from both sensor signals, which is added by a small difference in resistance between the passive resistor and the strain gauge in the voltage dividers. The mean is calculated over the first second of the test and subtracted from the input signal. This is done in every test, because due to creep and drift the mean is changing over time. Now that the offset is removed from the signal, the signal will go through a low-pass filter. This low-pass filter is a build-in block of 20-Sim and is shown in figure 3.13. The second mode is measured at around 86.2 Hz, and must go through the filter. The used filter is a Butterworth second-order filter with a cut-off frequency of 105 Hz. The bode plot magnitude and phase-shift of this filter is shown in figure 3.14. Two differential sensors are embedded on the positions from figure 3.5. To understand the sensor signals, the raw data and filtered data are shown in figure 3.15. Now the signal can be used to check which eigenmodes are present in the beam.

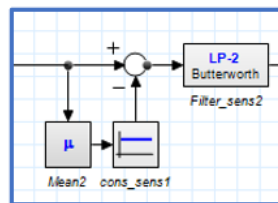


Figure 3.13: 20-Sim block-diagram of input signal processing

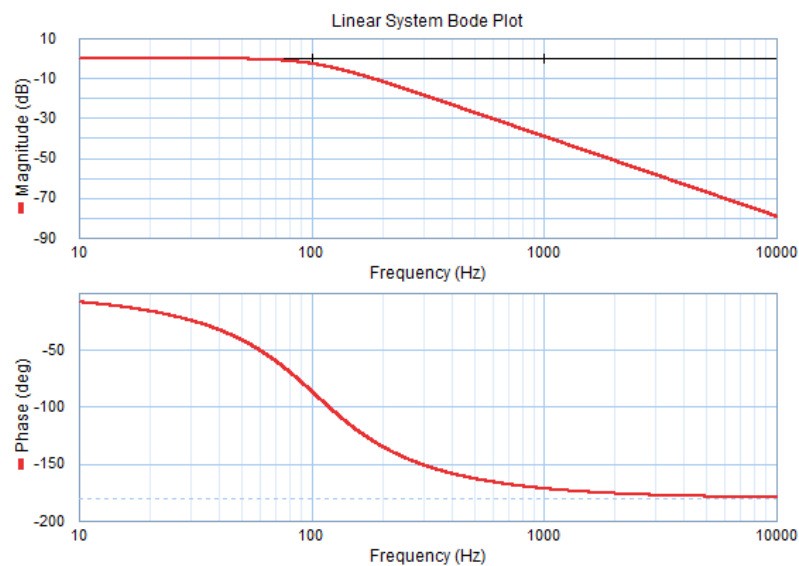


Figure 3.14: Bode plot of the Butterworth filter with a cut-off frequency of 105 Hz

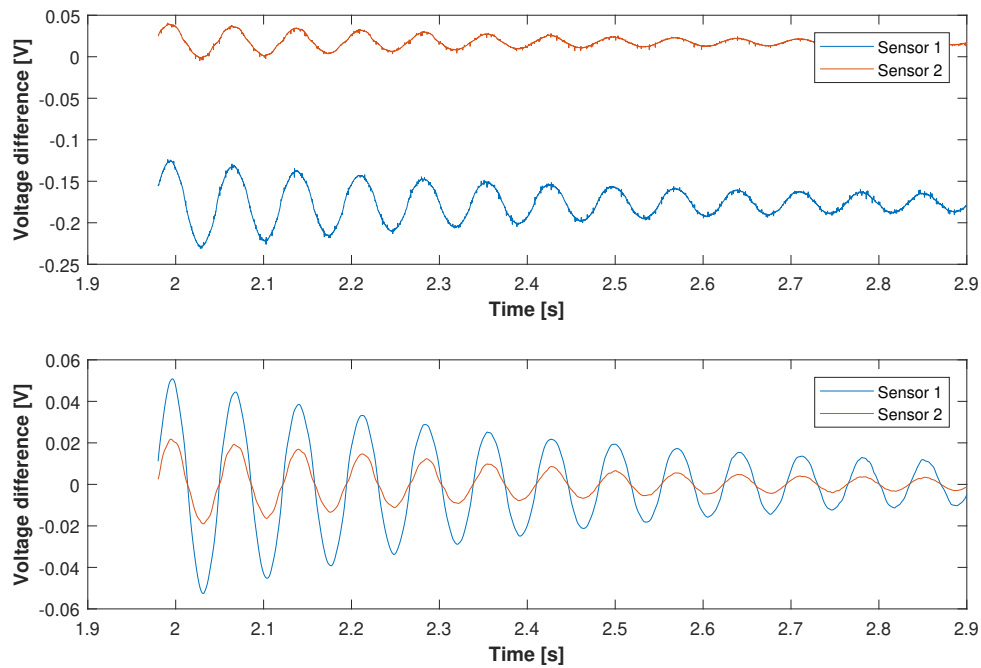


Figure 3.15: First mode (14.2 Hz) excitation response (A) Raw sensor signal (B) filtered sensor signal

3.4.2 Eigenmode check

As stated in the design requirements, the control loop should work at the frequencies of the different eigenmodes. From the third eigenmode on, it becomes extremely difficult to make accurate measurements. Therefore, the first 2 modes will be controlled. To distinguish the 2 modes, an eigenmode check has been implemented. The curvature and displacement curves of the first 2 eigenmodes are shown in figure 3.5. The strain gauges are measuring the curvature at 2 different places. Combining those results the eigenmodes of the beam can be predicted. When the beam is in the first mode, both signals will be simultaneously positive or simultaneously negative. When the beam is in the second mode, one sensor will measure a positive curvature while the other sensor will measure a negative curvature. Knowing this, logical operation built-in blocks are used as can be seen in figure 3.16.

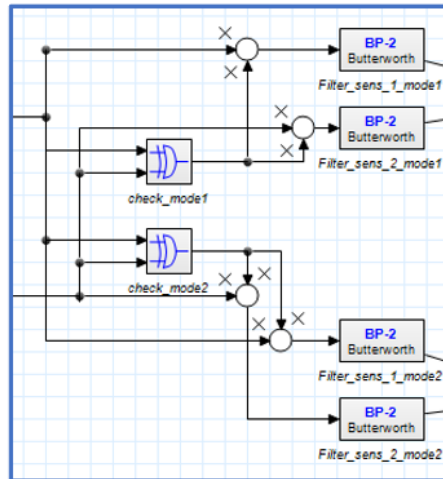


Figure 3.16: Schematic block-diagram of eigenmode checker. An Xor and NXor port are used to define the eigenmode.

Two operators are used, an Xor operator for the second mode and an NXor operator for the first mode. The measured signal is going through another filter. For the first mode this is a Butterworth second-order filter with a band pass between 10-20 Hz, because the peak of the bode plot is at exactly 14.2 Hz. For the second mode the band pass is changed to 70-100 Hz, because the peak is positioned at 86.2 Hz. The bode plots of the filters are shown in figure 3.17. The phase shift is also shown in this figure. Which is close to zero at the eigenfrequencies.

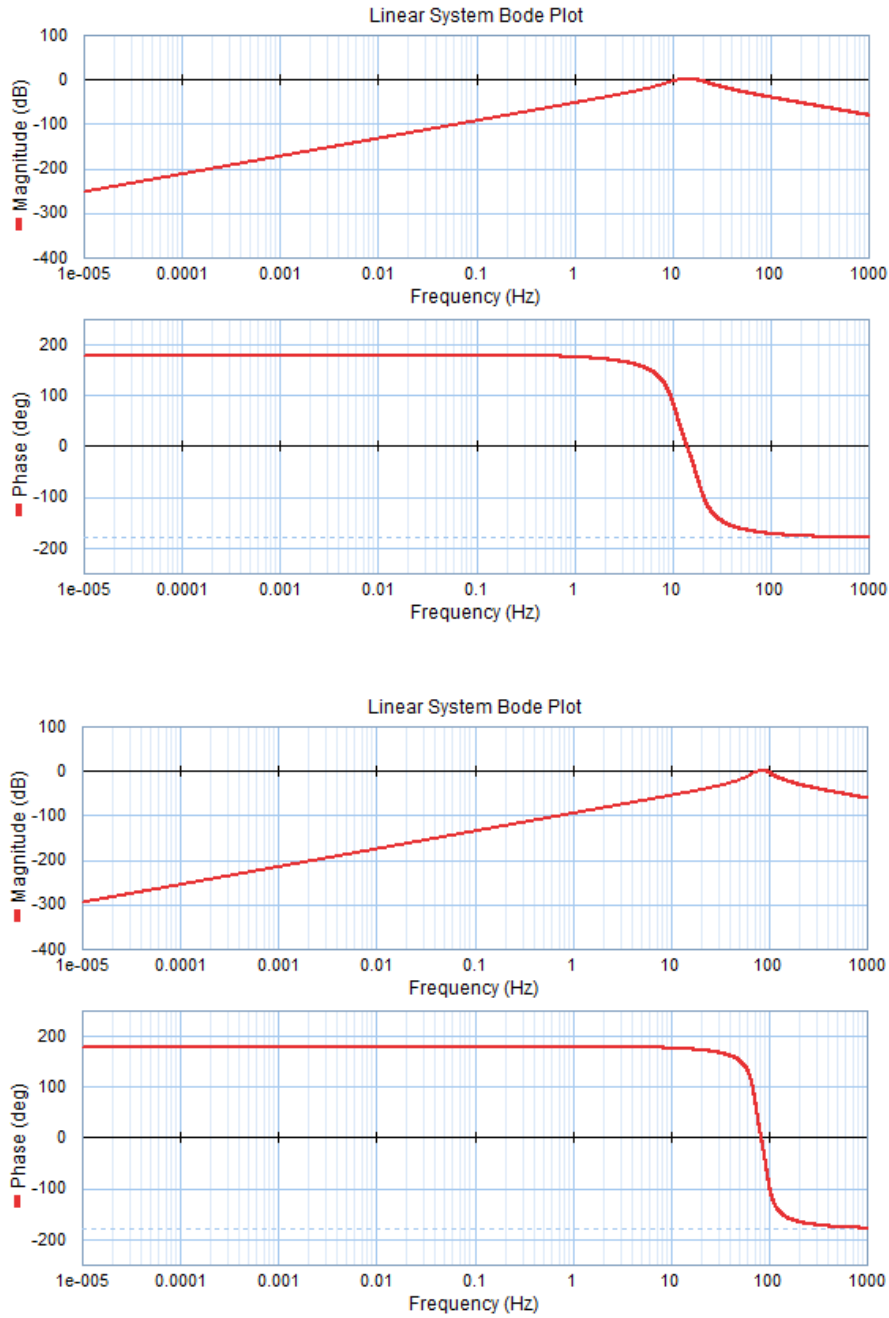


Figure 3.17: (A) Bode plot of first eigenfrequency band-pass filter (B) Bode plot of second eigenfrequency band-pass filter

3.4.3 Hamiltonian integral implementation

From chapter 2, it can be concluded that the derivative of the Hamiltonian should be negative to damp the system. The result of this equation is shown again:

$$k = -EI \int_0^L w_t w_{xx} \quad (3.7)$$

If removing energy from the system is desired, the sign of k should be opposite of the sign of the integral. EI is constant and always positive and is neglected in this equation. To get from the sensor data to the sign of k the next block diagram is used:

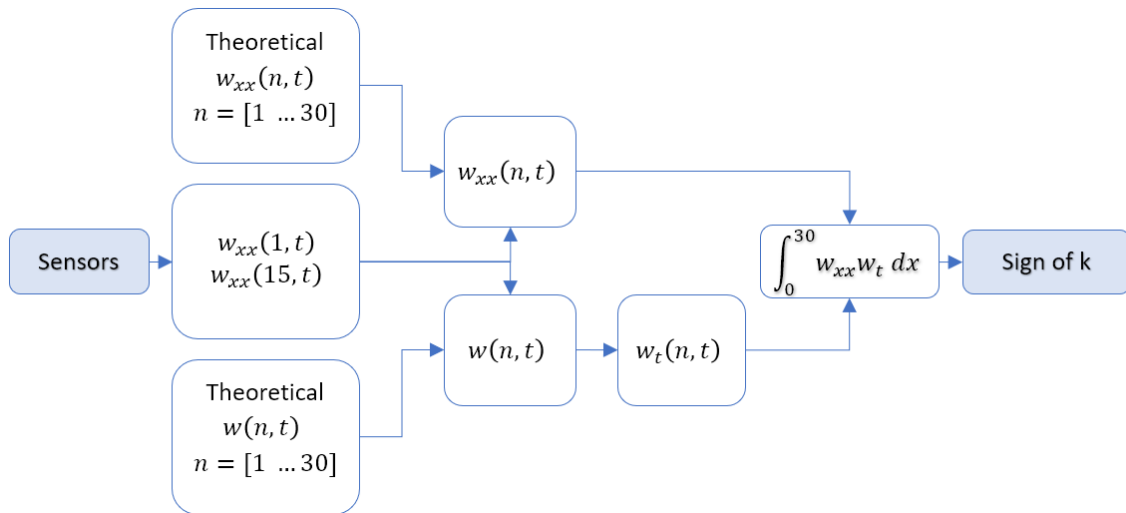


Figure 3.18: From the sensor signals to the control law design; n are the elements of the beam

The sensors are measuring the curvature of the beam at element 1 and 15 (shown in figure 3.5). The beam is divided in 30 elements. With the curvature sign known at element 1 and 15 the curvature sign and deflection sign of all elements can be approximated. the curvature sign can be used directly in the integral, however the deflection is differentiated over time to get the velocity sign. Which is also implemented in the integral. This results in the sign of k , this sign of k is used to vary the stiffness. A model is built in 20-Sim, see figure 3.19.

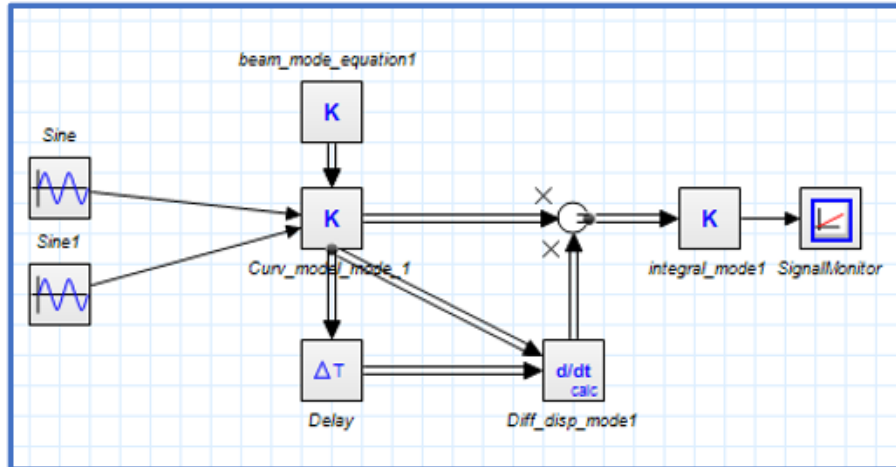


Figure 3.19: 20-Sim model from simulated sensors to integral output; beam mode equation code is shown in appendix C

An important note is that the precise gain is not needed for this damping-injection control-loop, but the sign of the curvature and displacement curve are. Also the curvature relation between those different finite elements is needed for the integral approximation.

Based on the displacement curve, the velocity curve can be approximated by differentiating the displacement curve over time. Normally noise will introduce high peaks when it is differentiated, but the signal is filtered digitally. Therefore high-frequency noise does not occur. Now $w_t w_{xx}$ can be integrated over the length of the beam. For the simulation 14.2 Hz is used, which is the first eigenmode. The simulation results of this model are shown in figure 3.20. In the first

plot the simulated sensor values are plotted, in the second plot the integral output is shown. The frequency of the integral output is doubled compared to the input signal. So the doubled frequency is the result of the multiplication of the two shifted harmonic signals with the same frequency.

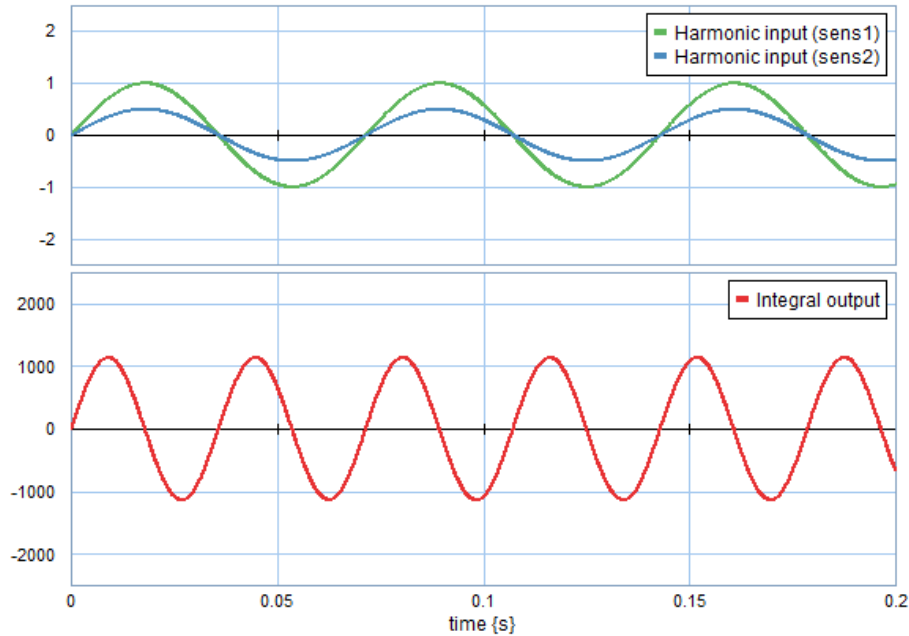


Figure 3.20: First mode simulation of the integral output, with the use of simulated curvature sensors

Control signal

The control signal is chosen to have a sinusoidal shape. Because only the sign of the integral is important to implement damping-injection, the control signal could also be a square wave. This is called a 'bang-bang' signal. It could be that the controller is more effective with a square wave than when using the sinusoidal wave, however the linearity of the signal would be lost. To keep a linear system, the sinusoidal signal is chosen.

Knowing that the curvature and velocity of the beam are correlated, the control integral could be simplified by removing the velocity approximation. In a harmonic system, the velocity can also be estimated by the curvature, because the velocity is a quarter period delayed compared to the curvature. The magnitude of the velocity will be lost. However the error which occurs by differentiating the beam shape is removed from the system when using this estimation. Because this estimation only works for controllers of harmonic systems, it is not chosen. To keep the controller as universal as possible, the velocity of the beam is thus approximated by differentiating the beam displacement shape.

Knowing the signal is sinusoidal and has a frequency twice the displacement frequency, the control signal is similar to parametric stiffness effects. The concept of damping with parametric stiffness is discussed in Appendix E. In the discussion the results of this control method and the parametric stiffness actuation method are compared.

3.4.4 Post-processing

The last step is processing the integrator output so it can be used as control input to the variable stiffness modulator. This process is shown in figure 3.21.

Control timing

The most important post-processing is the damping injection timing. Because the system has delays, the timing will be slightly off. Those delays occur at the digital filters, analog low-pass noise filters, digital processing (like differentiating), the motor controller, motor inertia and wire stretching. The digital filter delays can be found by the Bode-plots, but the other delays are mostly mechanical delays which are difficult to model. To compensate these delays, a lead-lag compensator can be used. A lead-lag compensator adds poles and zeros to the system. To do this, a working model of the whole system is needed, and this is not available. As such, another method must be found.

Because the setup is based on a flapping motion, it is harmonic. In a harmonic system an artificial delay can be added to sync the controller output with the sensor signals. Thus, the output is calculated on one cycle and implemented on the next half cycle, because the control frequency is twice the flapping motion. Because the system delay is not known, a delay sweep is done to see when the damping-injection occurs. This will be shown in chapter 5.

Wire pre-tensioning

To make it possible to both stiffen and soften the beam, the control gain will have an offset of 0.5 V. This is called pre-tensioning the wire. Using this pre-tensioning the beam stiffness can vary in both directions, as now it is also possible to release tensioning of the wire. During characterization pre-tension will also be used, because the eigenfrequency of the beam is different than when no tension is applied to the wire.

Control gain

The output of the integrator should be negated, as shown in equation 3.7. This negation is done in the control gain block. In this block the gain is tuned so that the maximal control is 1 V and the lowest gain is 0 V. This is chosen due to the motor controller using an input voltage of 0 to 1 V. A limiter is also set from 0 to 1 V to avoid the peak voltages. The limit is in a normal test not reached. The variable stiffness actuator can not implement a load which brings the beam into buckling.

With this last step the control-loop is finished, and therefore can be implemented into the setup.

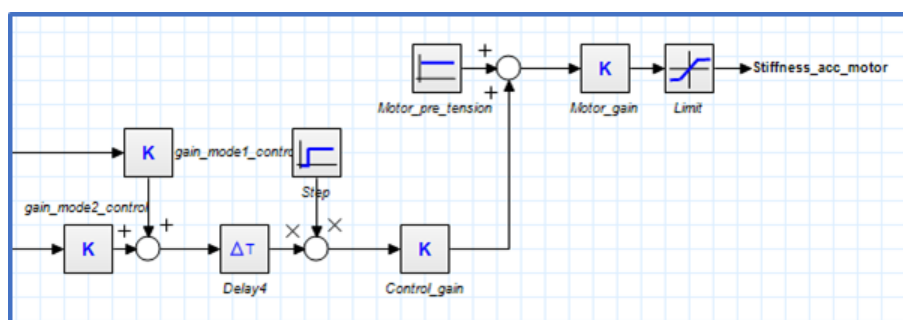


Figure 3.21: 20-Sim model for post-processing the integral output to the variable stiffness modulator

3.5 Conclusion

In this chapter the designs for the three sub-objectives, the 3D-printed beam with embedded sensors, variable stiffness actuator and energy-based controller, are introduced. The 3D-printed beam is designed such that the first eigenfrequency is at 14.2 Hz and the second mode at 86.2 Hz (as determined in the results, chapter 5.2). The differential sensors are positioned

such that the highest curvature can be measured. For the variable stiffness actuator, two different principles will be tested. One is the bow principle, the other one is the wire through a shaft. After the characterisation, the final design will be used in the experiments. The controller is tested in simulations, which show a positive result. Now the three different parts will be implemented in a setup, to test if the parts, and their combination, work as expected.

4 Implementation

In the implementation, the different parts of the design chapter are combined into an experimental setup. Fabricating and experimenting the combination of 3D-printing, energy-based control, and stiffness modulation is a state-of-the-art setup. The fabrication of the setup is explained in the first section of this chapter. In the second section, the experimental plans are discussed.

4.1 Fabrication & Assembly

The experimental setup consists of multiple connected parts of hardware. This section is divided into multiple sub-sections based on each component: RaM-stix (4.1.1), a shaker (4.1.2), a variable stiffness actuator (4.1.3), and the 3D-printed beam (4.1.4). First the complete setup is shown in figure 4.1. Also a block-diagram of the setup is shown in figure 4.2.

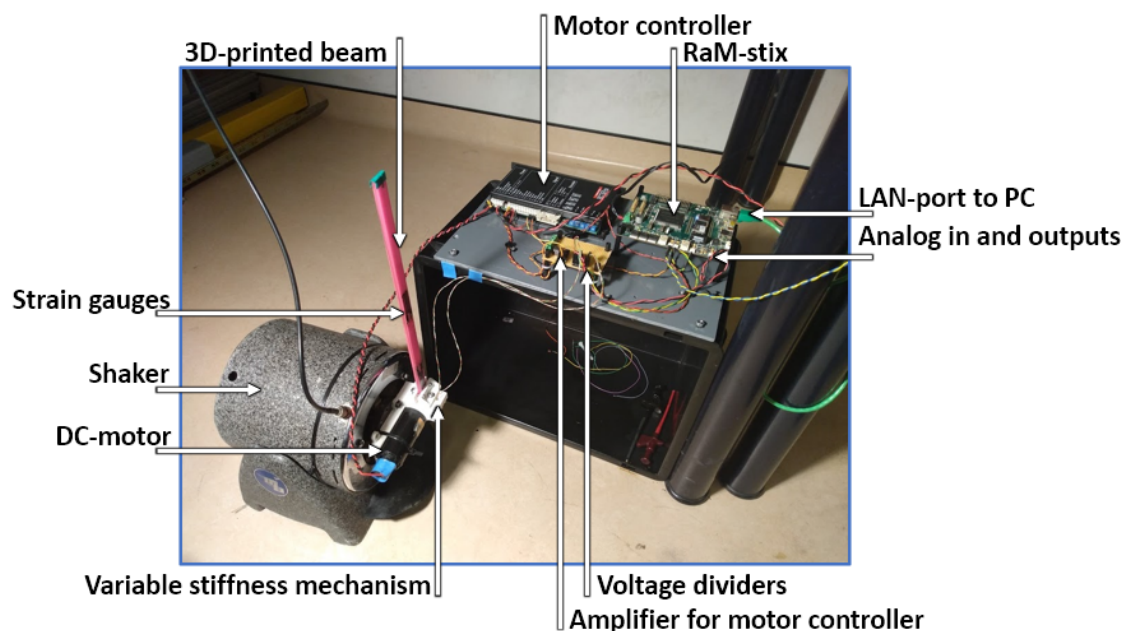


Figure 4.1: The experimental setup

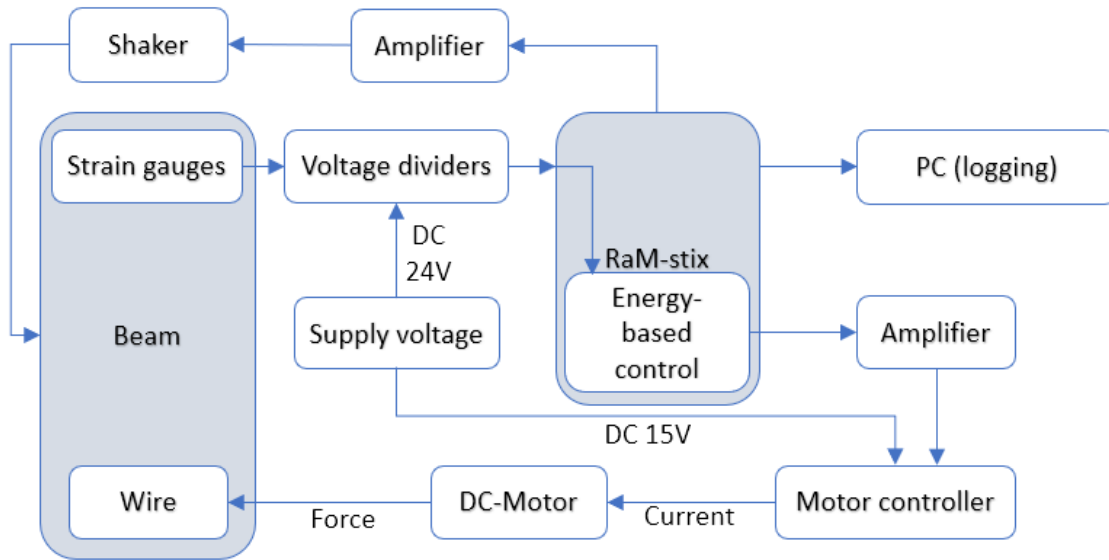


Figure 4.2: Block-diagram of the experimental setup, with all hardware components (except the amplifier for the shaker)

4.1.1 The RaM-stix board

The heart of this setup is the RaM-stix board, a piece of hardware connecting and controlling all the separate components. This baseboard is built by the University of Twente RaM group. This board is used for several reasons. The first one, the board has a sufficient number of analog inputs and outputs to connect all hardware. The second reason is that the board is compatible with 20-Sim. In 20-Sim the complete control-loop can be built and the data can be extracted from the RaM-stix. The third reason is that a high sample frequency can be used due to the fast internal calculations. As the control and data logging is done at the field-programmable gate array (FPGA), the data will not be transmitted through the LAN-port. By avoiding the slow transmission through the LAN-port, the processing time of the control-loop is decreased. Due to these reasons the RaM-stix is chosen over alternatives such as the NI MyDAQ and the Arduino Mega.

The processor, Gumstix Overo [Gumstix, 2020], of this board can be programmed using 20-Sim with the 20-sim 4C plug-in. 20-Sim 4C is an open-source real-time Linux, which helps running c-code on hardware (RaM-stix) to control setups. The RaM-stix is an expansion board for Gumstix Overo modules and, therefore connects the Gumstix with the FPGA. Digital and analog inputs/outputs are also built-on the RaM-stix, the board is shown in figure 4.3.

The C-code based control-loop, which is elaborated on in chapter 3, is exported to the RaM-Stix. The analog output ports of the RaM-stix are connected to the shaker and the variable stiffness modulator. The analog input ports are connected with the strain gauges. The variables of the input ports, output ports and state parameters of the control-loop can be logged. The logging can be done at high sample frequencies. With the used control-loop the maximum sample frequency is 5000 Hz, otherwise data drops out.

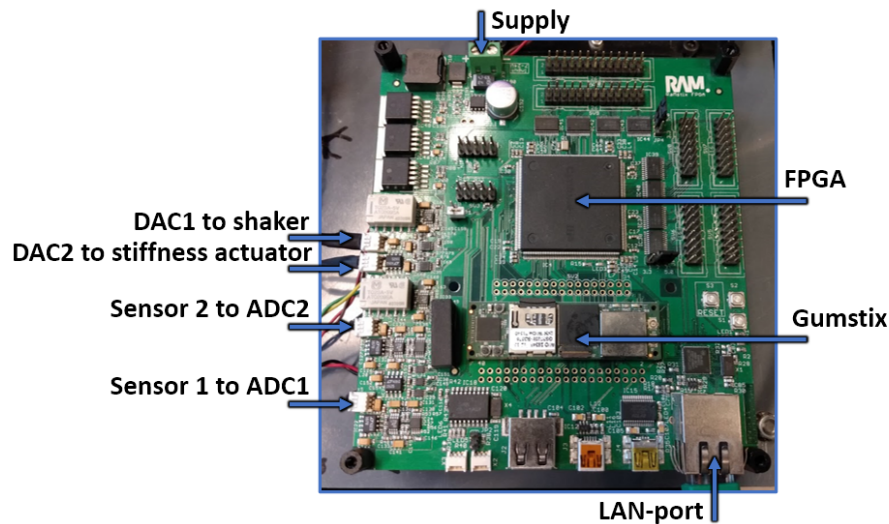


Figure 4.3: The RaM-stix board, all used ports are marked

4.1.2 The shaker

The beam can be excited using a shaker. The shaker applies a vibration on the variable stiffness actuator and the beam. The stiffness actuator has to vibrate in tandem with the beam, else the wires will tension related to the displacement when the beam is displaced by vibration. This is not desired, as it leads to uncontrolled changes in tension and thus beam stiffness. Because the stiffness actuator and the beam must be harmonically excited, a shaker is required with enough power to vibrate the entire mass of this system. The MB PM-50A shaker is able to do this [MB Dynamcis, 2020]. The resonance frequency of the shaker is at 8000 Hz, which is far above the second mode (86.2 Hz).

The shaker is used in the experiments to excite the beam harmonically to the specific eigenfrequencies, a minimum of 46 V was found to be required for the MB PM-50A shaker to do this. The analog output of the RaM-stix is only 1 V, thus this signal is amplified 46 times. With the amplified signal the shaker can excite the whole setup. The RaM-stix, controlled by 20-Sim, is used to tune the amplitude, frequency, phase, start time and stop time.

4.1.3 Variable stiffness actuator

In figure 3.9 the variable stiffness actuator is already shown. To implement the stiffness actuator, the motor must be driven using current control as the motor will be actuated in stall mode. This is done via a motor controller, with the only requirement being that the current is linear to the voltage input. The used controller is a Maxon ADS50/5 4-Q-DC [Maxon motors, 2020], which meets this requirement. This motor's input voltage should be between 0 and 12 V to produce minimum and maximum current. However the analog output of the RaM-stix is 1 V, therefore the signal should be amplified. A 12x amplifier circuit is designed and shown in appendix F.

4.1.4 The 3D-printed beam

Printer restrictions

A beam with embedded sensors is made of at least two materials, so the 3D-printer should have at least two different extruders. Also, the bed of the printer should be large enough to print the beam. Therefore the Diabase H-series printer is used for its multi-material capabilities in combination with its large printing volume. The Diabase printer is shown in figure 4.4

The Diabase H-series 3D printer has a printing volume of 416 mm x 186 mm x 210 mm ($X \times Y \times Z$) [Diabase Engineering, 2020]. The beam will be printed horizontally because this is the largest dimension.

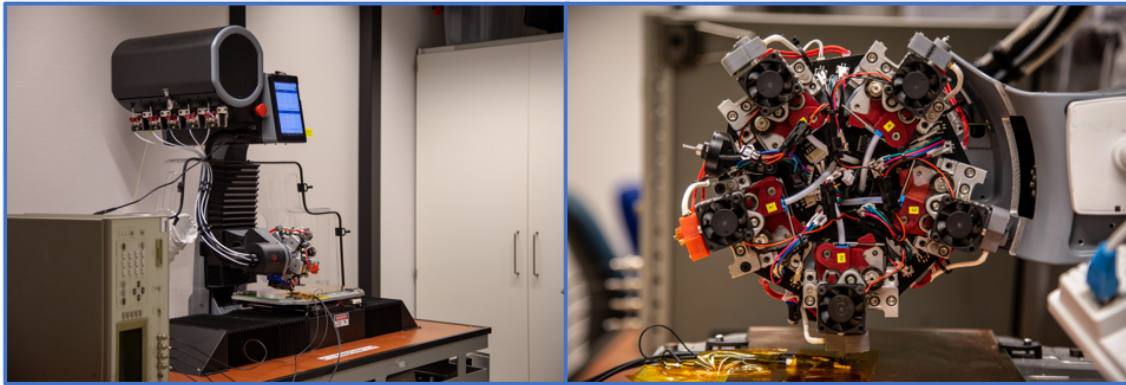


Figure 4.4: (A) Diabase 3D-printer (B) the five extruders of the printer ©Gerjan Wolterink

In chapter 3.2.1 shafts for electric wires were incorporated into the design. The electric wires connect the strain sensors to the RaM-stix. The electric wires are implemented inside the beam instead of on top of the surface. This is done because it means the wires are at the midline of the bending beam, where the stress during bending is minimal. Therefore the wires do not come under tension and do not influence the stiffness of the beam. Another advantage is that the wire is surrounded by the beam, effectively acting as a continuous clamp, and therefore the wire connections to the sensor pads are tensionless. When a connection is tensionless the results are expected to be more reliable. The electric wire is melted into the contact pads of the sensor using a solder iron at 200 °C.

The dimensions of the beam are 300 x 15 x 5 mm, as discussed in chapter 3.2.1. When the beam is printed and removed from the printer bed, the beam is not completely straight. Residual stress is present inside the beam. To reduce the residual stress the beam is heated to 150 °C for ten minutes. The result is shown in figure 4.5.

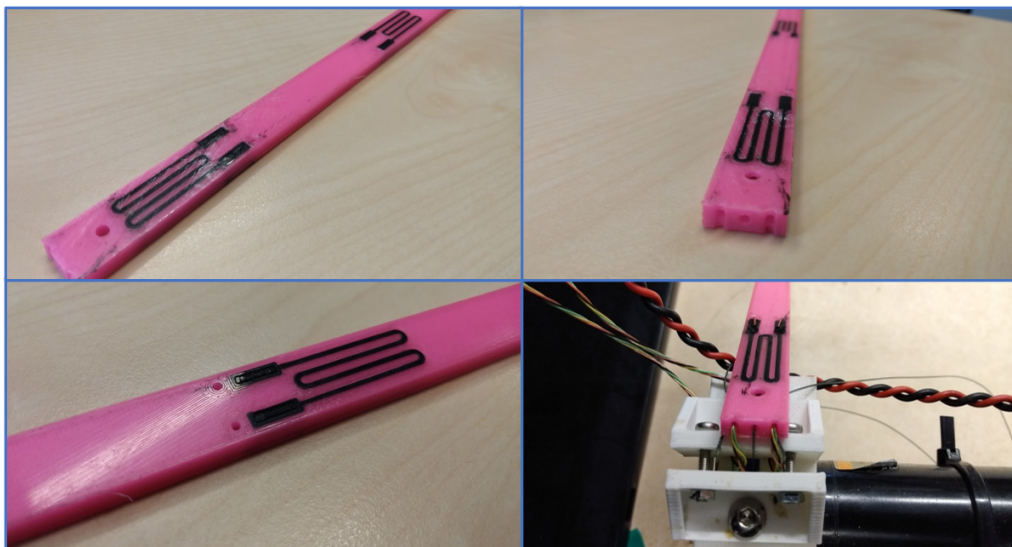


Figure 4.5: 3D-printed beam with embedded gauges and internal shafts

4.1.5 Total setup

The complete 20-Sim model, which is uploaded to the RaM-stix, is shown in figure 4.6. The setup is the same as figure 3.11, only the shaker is added. The RaM-stix with the 20-Sim model from figure 4.6 will be connected to the hardware using the analog ports. The two inputs are connected to the voltage dividers of the strain gauges. One of the outputs is connected to the amplifier of the shaker. And, last, the output of the control-loop is connected to the stiffness modulation motor. The other blocks, which are part of the control-loop, are already explained in chapter 3.4. The sensor values are processed so the present eigenmode can be found. Knowing the eigenmode the eigenshape can be estimated. Therefore the sign of the velocity and curvature are known and the integral can be solved. This result will be processed to go into the stiffness actuator.

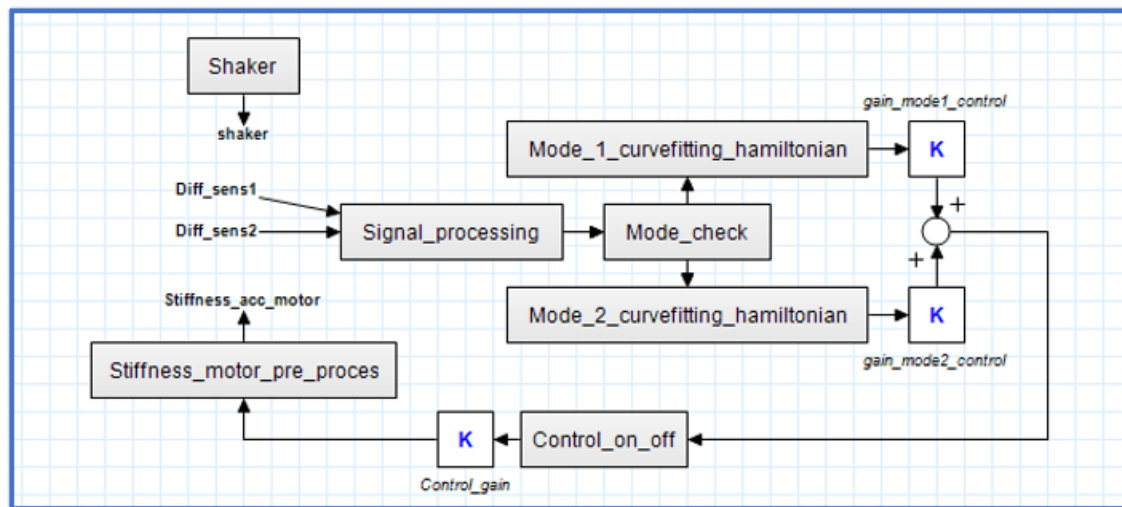


Figure 4.6: 20-Sim model used for the experiments

4.2 Experimental structure

To characterise the setup and validate the theory, the experiments are divided in five sections: Sensor characterisation, dynamics of the beam, effect of damping-injection, adaptability using control timing and video validation. Those five experiments give insight into the answers to the research questions.

4.2.1 Sensor characterisation

The sensor characterisation can confirm research question two "*How can 3D-printed embedded sensors be used to determine the flapping dynamics?*". As mentioned in chapter 5.1, the curvature of the beam can be measured differentially using two sensors. The sensors are positioned at the same x -position of the beam, with a displacement from the midline in the positive and negative y -direction. This measuring manner will be tested during the sensor characterisation, to see if the quality of the sensor output signal is high enough to be used for the control input. Therefore, the SN-ratio, symmetry of the signal, non-linearity, hysteresis and creep are measured to assess the sensor output signal quality.

The sensors can be characterised by position controlling the tip of the beam while measuring the sensor output. For this test a single differential sensor is printed in a smaller beam, which is connected with a nylon bolt to a linear actuator (SMAC LCA25-050-15F). See figure 4.7. The linear actuator is controlled using a sinusoidal position as setpoint trajectory. If the beam is connected directly to the SMAC-actuator, the beam will be clamped at both tips. This will in-

duce stiffening in the beam. To counteract this behaviour a nylon bolt is used with a diameter of 5 mm. This bolt is stiff in the axial direction but compliant for bending. The bolt is used as flexure to release rotational stiffness at the tip. Therefore the beam behaves like a cantilever.

Using the voltage dividers, explained in chapter 5.1, the output voltage and position of the SMAC-actuator are logged using a TiePie oscilloscopes.

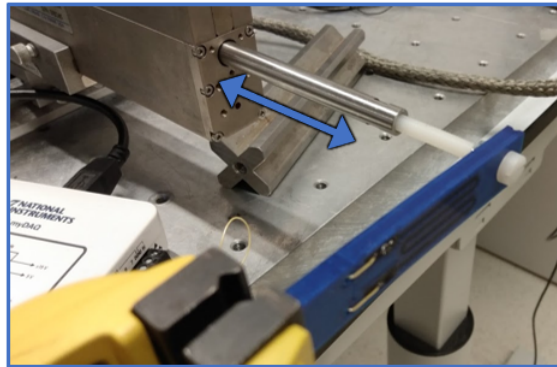


Figure 4.7: SMAC-actuator upper left corner, driven by a sinoidal position trajectory. In the middle the blue beam with embedded sensors, which will be characterised.

4.2.2 Dynamics of the beam

As discussed in chapter 2.1 the stiffness of the beam can be quantified by the change in eigenfrequency. A lower eigenfrequency corresponds to a softer beam, which leads to an answer on research question one "*How can stiffness variations of a beam be influenced?*". The first and second eigenfrequency of the beam can be found by applying a static axial load on the beam and performing a frequency sweep. The experimental setup of figure 4.1 will be used, except the control will be open-loop so the axial load is static. This means that a frequency sweep is done with the shaker while having a fixed axial load. The RaM-stix will be used to actuate and log.

This is also a suitable way to test whether the wire through the shaft beam construction generates enough stiffness variation for the desired effects. If this is not the case, this will also be assessed for the bow principle to determine which setup should be used in the final experiments.

4.2.3 Effect of damping-injection

As part of research question four "*Can port-Hamiltonian modelling be used to design a stabilising control law for flexible beams and how?*", the effect of the control law on the damping of the system must be analysed, in order to discover how control-loop output correlates to the system's damping-coefficient. If this can be found, the proposed control law holds true in practice and can be used to control the system as desired.

A method to measure the damping of a system is by measuring the decay of the excitation response. The system should be excited, and by natural damping the beam vibrations will decrease over time. If damping-injection is applied, the exponential decay will increase. With the curve fitting toolbox of Matlab the exponential decay can be approximated, and therefore also the effect of damping-injection.

To excite the beam to one of the eigenmodes, the shaker will vibrate at the corresponding eigenfrequency, after two seconds the shaker is stopped. At this point the beam can be damped naturally or by damping-injection. The behaviour of the beam after the shaker is stopped is called the excitation response. The input signal of the shaker is shown in figure 4.8. Also the natural

excitation response of the beam in first mode, as measured by the embedded strain gauges, is shown.

To understand how the beam vibrations behave when the proposed control is applied, the damping should be investigated by running multiple excitation response tests with different control gains. The control gain will be tuned using 20-Sim, between 0 and 1 with steps of 0.2. The control-loop calculations are done through the whole experiment. Only from two seconds the output is connected to the variable stiffness mechanism. By approximating the different damping coefficient, the effect of the damping-injection can be quantified.

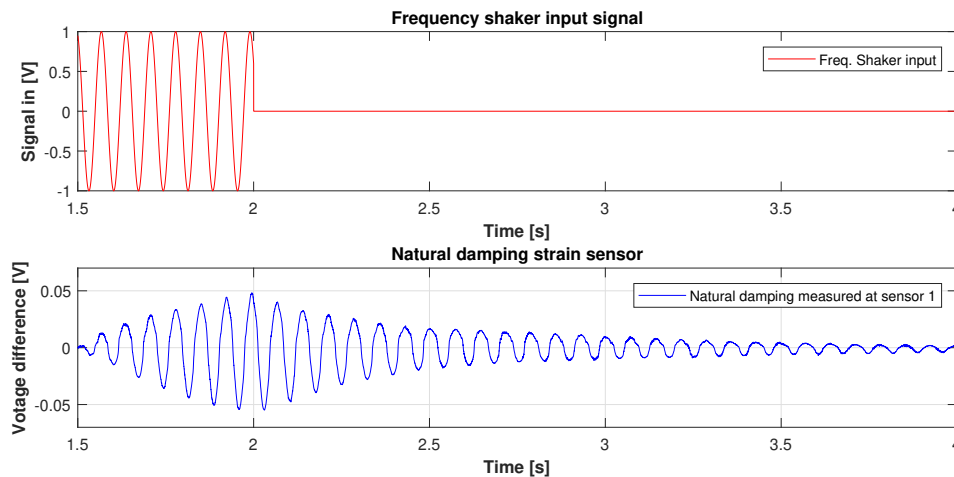


Figure 4.8: Shaker input and measured sensor signal (beam curvature)

4.2.4 Video validation with different eigenmodes

The sensors, variable stiffness actuator and control-loop injection-damping have been tested separate from each other. To validate whether the entire system works as expected in practice, sensor measurements should be compared to observed beam behaviour. Two methods can be used: an accelerometer at the tip of the beam or a high-speed camera. If an accelerometer is added, the dynamics of the beam are changed due to the added mass on the tip and wires which can influence the stiffness of the beam. Using a camera will not change the dynamics. A big disadvantage is that it can not be logged like an accelerometer, and only provides a visual indication of displacement, which is correlated with the curvature of the beam. Luckily, for validating the damping-injection exact logging is not needed. Using a natural damped system and a controlled system, the difference in displacement between the two can be seen over time. The visual difference in displacement between the video and the difference in curvature as measured by the sensors can then be compared. Not only should the sensor measurements correspond to the visual displacement, the differences between the natural damped and damping-injection systems should be proportionally similar for both the sensor measurements and visual displacement.

The video validation will be done using the Casio Exilim ex-zr200 camera. This camera has a high-speed setting, which increases the fps (frames per minute), but decreases the image format. The maximum fps is 1000 with an image format of 224x64 pixels. This is used for the second eigenfrequency (86.2 Hz). With 1000 fps around 12 images are taken in one cycle. This is the bare minimum to investigate the damping behaviour of the beam, because the maximal deflection should be captured every cycle. For the first eigenfrequency (14.2 Hz) 480 fps are used, so around 34 images are taken in one cycle. When a lower framerate is used the image quality increases to 224x160 pixels. This is desired because the data is compared visually. The

naturally damped and damping-injection responses are video-layered on top of each other in the video footage. This way the difference in displacement becomes visible.

4.2.5 Adaptability using control timing

By changing the timing the beam behaviour can be modified, this will help to get to understand research question 4 "*What beam behaviour (modifications) can be obtained using controlled beam stiffness variations?*". In the post-processing of the control (section 5.5) an artificial delay is implemented to ensure the right timing of the stiffness actuation with the signal cycle. This effectively neutralizes the delays added by the filters, amplifiers and mechanical system. The system delays plus the artificial delay should cause the signal output to shift exactly one cycle. The cycle length is known, but as the system delay is unknown due to its complexity, the artificial delay can not be determined analytically. Instead, this is determined experimentally through testing the effectiveness of damping with different artificial delays. Damping should be most effective when the total delay equals exactly one cycle.

The control frequency is twice the vibration frequency of the beam. In figure 3.20 the vibration and control signals are shown. Therefore a shift of 180 deg at the eigenfrequency equals a shift of one cycle of the control frequency.

The first eigenfrequency is at 14.2 Hz (experimental data 5.2) and the RaM-stix sample frequency is set at 5000 Hz (sample time is 0.2 ms). Therefore every beam cycle yields 352 data samples. If a beam cycle of the first eigenmode has 352 samples, the control cycle of the first mode will have 176 samples. This means that for the first mode a delay sweep between 1 and 176 sample delays is tested.

The damping-injection delay which corresponds to the maximum effective damping in the system is the desired delay. For the first mode delay steps of 25 are used so in total there are eight excitation responses, from 1 to 175. The excitation responses are processed in Matlab by using the curvefit toolbox. This results in a damping coefficient - delay time plot.

4.3 Conclusion

In this chapter the three objectives, a 3D-printed beam with embedded sensors, variable stiffness actuation and the controller are implemented in a setup. This setup can be excited using a shaker. The various experiments are elaborated. The experimental results are shown in the next chapter.

5 Experimental Results

In chapter 3, different design choices are elaborated. Those designed parts are: a 3D-printed beam, a variable stiffness mechanism and the control; they are combined into a final setup in chapter 4. The final setup is tested by a test sequence which proves if the beam vibrations can behave as desired. The performance of the proposed system will be evaluated along the following lines:

- *Characterization of the sensors* by measuring both the displacement and the sensors individually, as well as combined. Also the hysteresis, creep and drift are analysed.
- The *Dynamic behaviour of the beam* is tested using a frequency sweep to find the eigenfrequencies. Multiple tests are done with different axial loads to see if this results in a shift in eigenfrequencies. This test will be done with two different setups, one with the wire inside the shaft and one with the wire outside.
- *Validation by video* first and second mode sensor-values are compared with high-speed video footage. This is done to see if the damping increases when the control is implemented.
- *Effect of damping-injection*, exciting the beam in the first mode a sequence of different control gains is tested to understand how the damped system behaves.
- *Adaptability using control timing*, the timing is important to increase the damping of the system.

5.1 Characterization of the sensors

In chapter 3.2, a differential voltage measurement setup is found to be preferred to measure the curvature of the beam. The curvature is needed as input for the control-loop. To control the effective stiffness of the beam, the sign of the curvature and the frequency are important. This could be tested by logging the sensor values and the displacement at the tip.

To measure the behaviour of the sensors, a test has been executed. The test setup of chapter 4.2.1 is used. The linear actuator (SMAC) is moving the tip of the beam in a sinusoidal translation between -2.3 mm and 2.3 mm for 10 s. The individual strain sensor outputs are logged and are also subtracted from each other. The results are shown in figure 5.1. Because a nylon flexure between the beam and the SMAC-actuator is used, the beam behaves like a cantilever. However the vibration frequency is set at 2 Hz. Because the SMAC-actuator can not drive at a frequency of 14.2 Hz while maintaining a displacement-amplitude that is measurable.

As can be seen, the individual sensors do not respond in a linear manner. When the sensor is compressed first the voltage increases and at a certain moment, it stops increasing and even decreases. This behaviour is also concluded in [Christ et al., 2017]. The signal is not symmetric, however the time between zero crossings is the same every half cycle. So the sign can be measured and can be used as controller input.

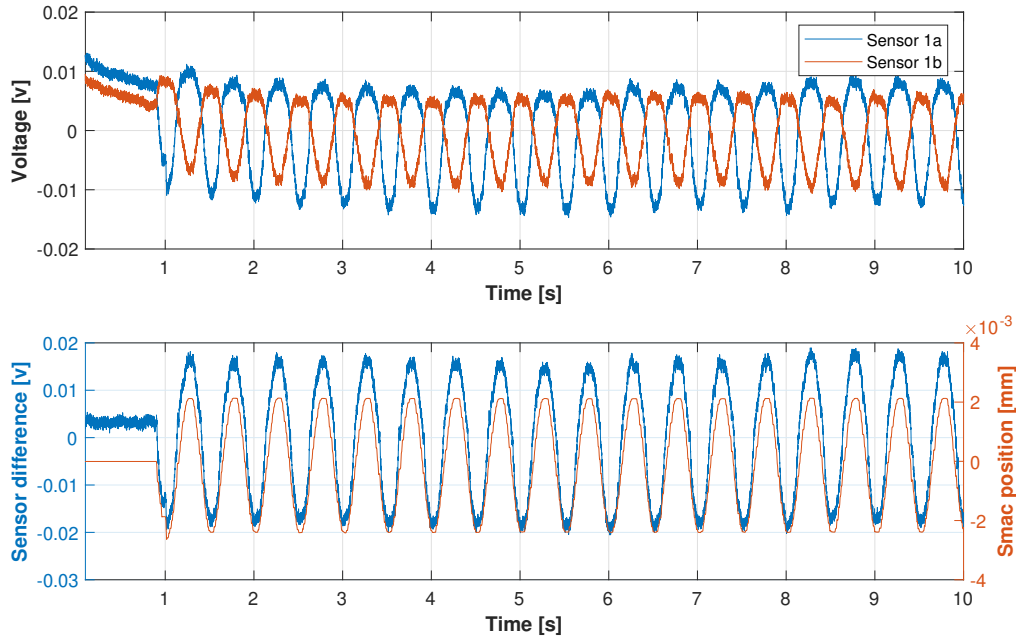


Figure 5.1: (A) The two signals of the difference sensor with a low pass filter cut-off frequency at 105 Hz, same as in the control-loop. And the offset is removed (B) Signals combined and plotted with the tip displacement

Another uncertainty of the sensor is the signal-to-noise ratio. If this ratio is too low, the control-loop can not distinguish the curvature of the beam from the noise. To investigate the noise intensity, the frequency spectrum plot is shown in figure 5.2. In this test the data is not filtered, therefore all peaks are visible. It can be seen that the peak at 2 Hz is the highest peak. This is as expected, because the SMAC-actuator is vibrating at 2 Hz. The 2 Hz signal peak is way above the SNR of 3 (see equation 5.1). In the controller the signal will also be filtered and therefore it can be used in the control-loop.

$$SNR = \frac{P_{\text{desired}}}{P_{\text{noise}}} = \frac{0.8053}{1.5692e^{-6}} = 5.1319e^5 \quad (5.1)$$

There are some smaller fundamental frequency peaks up to 12 Hz, which are the non-linearities of the sensor, to reduce those peaks differential sensing is used. Now the tip position - sensor difference voltage can be analysed, as shown in figure 5.3. A filter of 12 Hz is used to remove the high frequency noise. The curve does not show hysteresis, drift, or creep. But other non-linearity is visible close to the zero crossing, this could influence the curvature sign measurement. However, the non-linearity is small, therefore no further research was deemed to be required for the application of the sensors in this work.

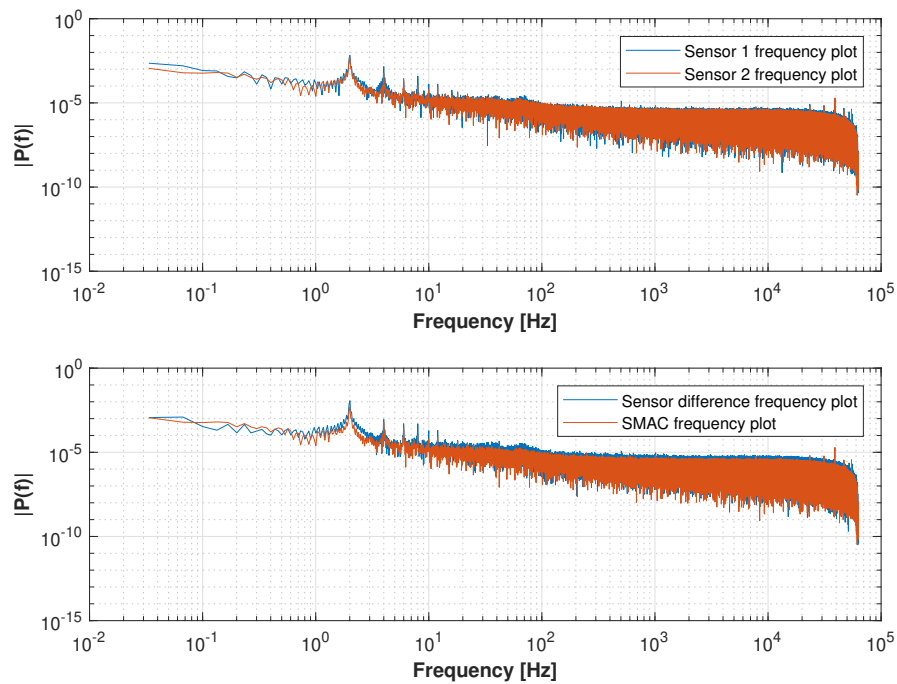


Figure 5.2: The frequency spectrum is plotted, to give insights for the signal to noise ratio. This is unfiltered data

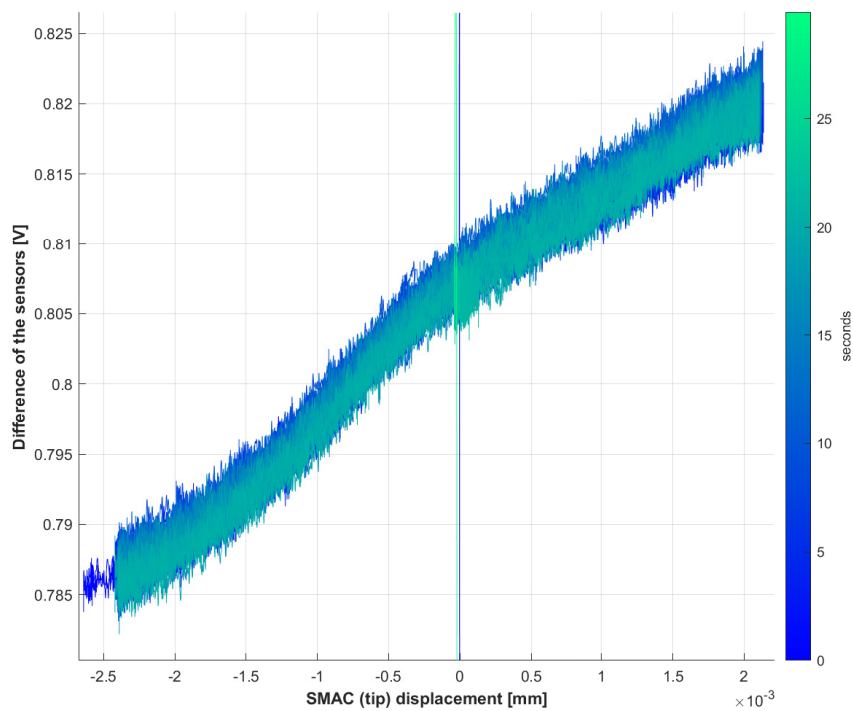


Figure 5.3: The sensor voltage difference plotted against the tip displacement to check the hysteresis, drift, creep and other non-linearities. The signal has been filtered by a lowpass-filter, with a cut-off frequency of 12 Hz.

5.2 Dynamic behaviour of the beam

To measure the effective stiffness change of the beam, the shift of eigenfrequencies can be analysed by running a frequency sweep. Multiple frequency sweeps from 0- 120 Hz are performed with different axial loads. This is done with two setups, in the first setup the wire is inside the beam (through a shaft), section 3.3. In the second setup the wire is outside the beam (bow principle), see figure 3.6.

The frequency sweep is done with five different load gains from 0 to 1. If a gain of 1 is used, a current of 2.0 A flows through the motor. From the static load curve of figure 3.10, the axial load is 7 N. The frequency domain plot of the wire through the shaft at the middle line is shown in figure 5.4. The frequency plot of the bow principle is shown in figure 5.5. In both setups the first two eigenfrequencies are shown. For each load gain the eigenfrequencies are found and plotted against each other. Those results are shown in figure 5.6. The eigenfrequencies are found in the frequency spectrum using the findpeaks tool of the Matlab toolbox.

In both tests, bow principle and wire through a shaft, at sensor 1 a peak is visible around 43 Hz, this is the first eigenmode in the z -direction. With linear strain sensors, this mode in z -direction could not have been measured. Because the 3D-printed sensors are not linear, as shown in figure 5.1, this mode is also exposed.

For the wire through the shaft, the results are different than expected. The first eigenfrequency should increase by the Beck-type softening. But it decreases by 0.1 Hz over 7 N. The difference between theory and experiments may be explained by at least two reasons. First, the shaft has a diameter of 1 mm. Therefore the wire is not exactly at the mid-line, and therefore a small bow-type softening occurs. The second clarification could be that when the beam is curved, the wire will apply not only a force on the tip of the beam in axial direction, but also a force against the wall of the shaft. This theory should be researched in future work. However, the second eigenfrequency is decaying as expected from the analysis.

Looking at the second setup, when the wire is implemented at the outside of the beam, a shift in eigenfrequencies is visible. The decrease of the first eigenfrequency is around 0.5 Hz and the second eigenfrequency decreases around 4 Hz, going from no to maximum axial load. This is less than expected from the analysis when looking at the Euler-type softening. But with the bow principle not only a force in the x -direction is applied, like the theoretical Euler-type softening theory. But also a small component is applied on the y -direction.

The stiffness change is less than expected. In this particular experiment a static load is applied. In the other experiments the axial load varies. This results in peak loads. In figure 3.10 the peak loads are also shown. The applied force is higher than when only using a static load. For this reason the stiffness will vary more in modulation than is shown in the static test. Therefore, the bow principle is used in the final experiment.

Knowing that the bow principle will be used in further tests, the first and second eigenfrequencies are determined. The wire will be pre-tensioned at 0.5 'motorgain'. If pre-tensioning is used the beam's stiffness can be made both stiffer and softer, whereas without pre-tensioning the wire can only be tensioned. The eigenfrequencies are found using the findpeaks tool from the Matlab toolbox.

The bow principle test at 0.5 pre-tension gain shows that: the First eigenfrequency is at 14.2 Hz and the second eigenfrequency is at 86.2 Hz

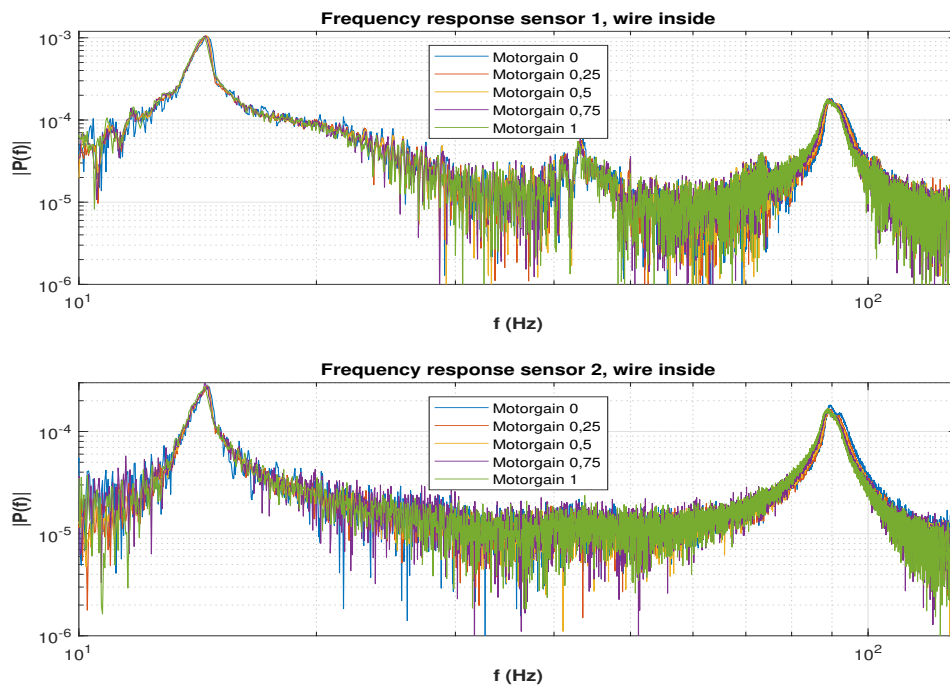


Figure 5.4: Power versus frequency response with static stiffness, with the inside wire. The first two eigenfrequencies are shown at around 14 Hz (first order mode) and around 86 Hz (second order mode).

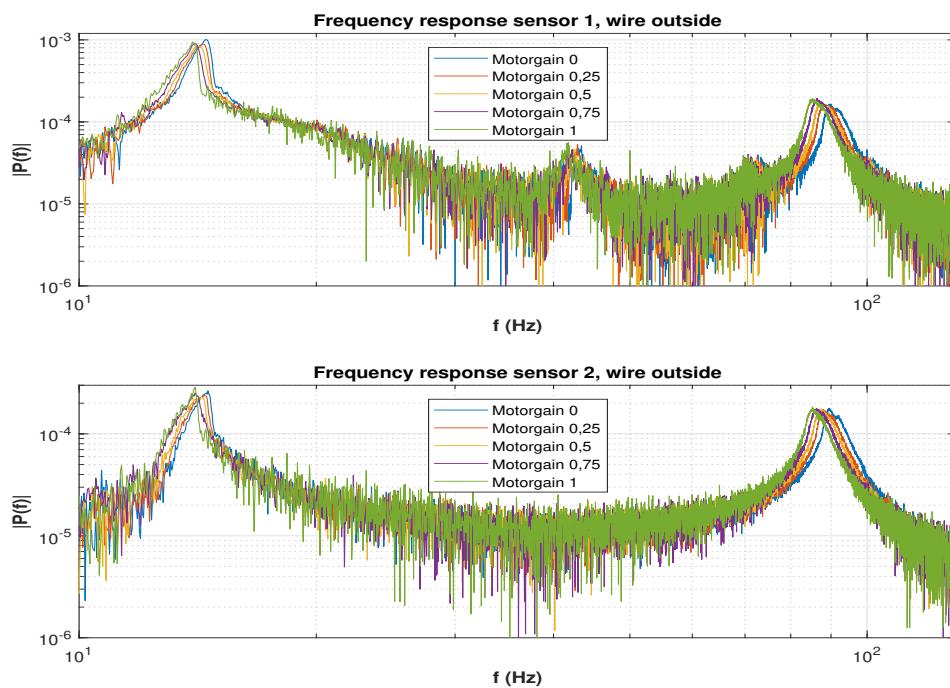


Figure 5.5: Power versus frequency response with static stiffness, with the outside wire. The first two eigenfrequencies are shown at around 14 Hz (first order mode) and around 86 Hz (second order mode).

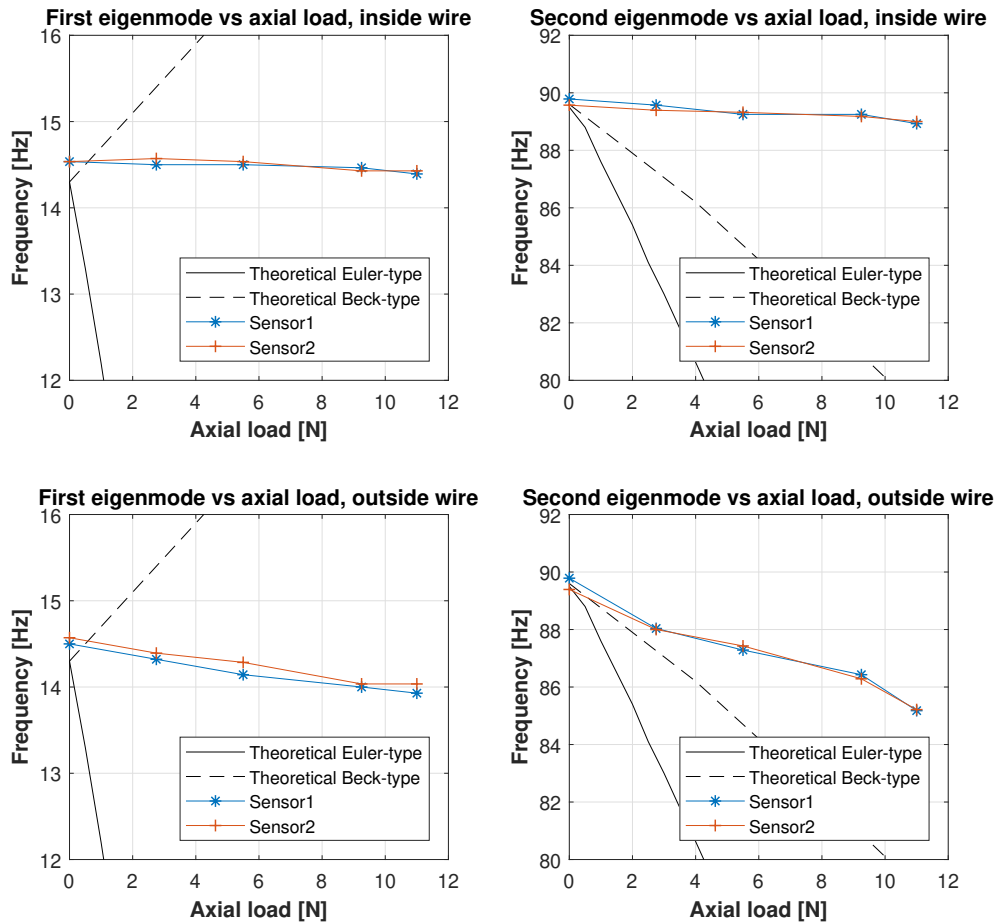


Figure 5.6: The axial load is plotted versus the eigenfrequency, with a different wire setup

5.3 Validation by video

The video validation is done in two different sub-sections, the first one will evaluate the results of the first mode damping-injection. The same is done in the second sub-section for the second mode.

5.3.1 First eigenmode

To verify damping-injection two tests are done. The beam will be excited in the first eigenfrequency. At 2 s in the test, the shaker input signal is stopped. After 2 s the system will damp naturally in the first test. In the second test damping-injection is applied. In both excitation responses the lateral curvature is measured by the strain gauges. The result of this is shown in figure 5.7. The input of the stiffness modulation system is shown in figure 5.8.

Especially looking at the first sensor, the one closest to the clamped-end, the additional damping is clearly visible in the measurement. This is so because the first sensor is at the position where the curvature is maximal. The blue line shows a faster decay of the amplitude.

The videos of both tests are superimposed, this is shown in figure 5.9. The orange beam is the naturally damped system. The green beam is the exciting response with damping-injection. Visible is that at the start, the beams are exactly on top of each other. At the maximal displace-

ment positions (peaks of the curvature), the green beam has reduced deflection. This indicates an increase in damping.

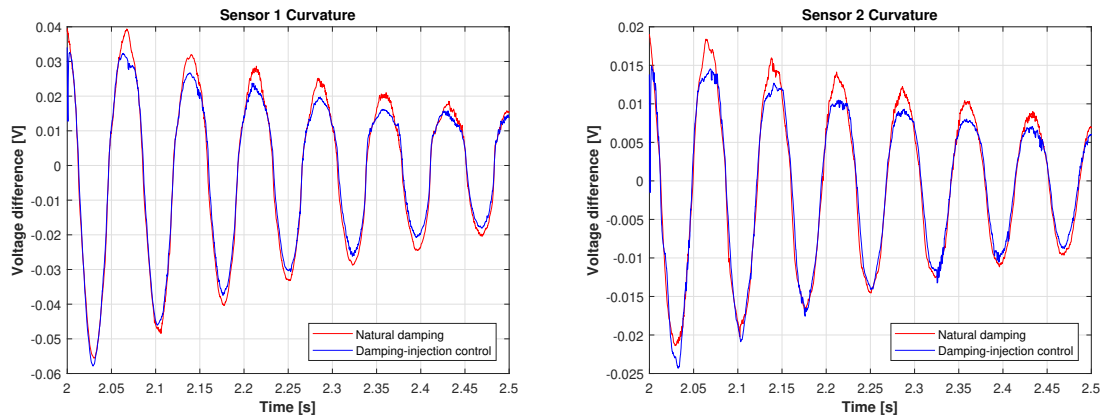


Figure 5.7: First eigenfrequency excitation response (14.2 Hz) (A) First curvature sensor (B) Second curvature sensor ; Voltage differential measurement in the case of natural damping and damping-injection with control gain 1 (video validation)

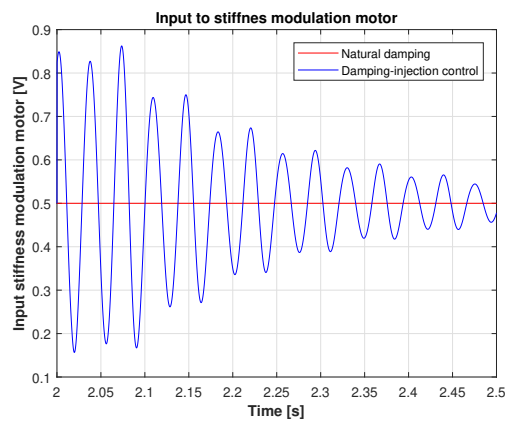


Figure 5.8: Input of the variable stiffness actuator, in the case of natural damping and damping-injection control (video validation)

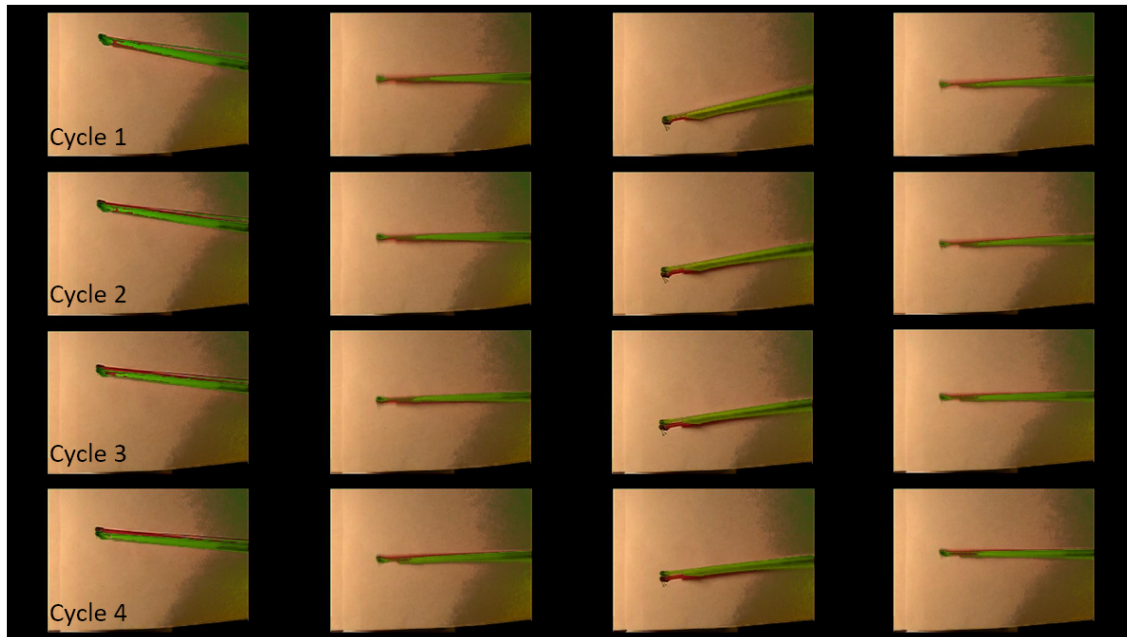


Figure 5.9: First mode video frames captured at zero- and peaks-curvature; orange beam is without control; green beam is with damping-injection control. In the left column the green beam is less deflected than the orange one. This is also the case in the third column. Only three quarter of the beam is captured

5.3.2 Second eigenmode

Two tests are done to test the second mode excitation response, one with control and one without. But now the shaker excites the second mode. The sensor signal results are shown in figure 5.10. The stiffness actuation input is shown in figure 5.11. In the second order excitation response of sensor 1 not only the second eigenfrequency occurs. Also the first eigenfrequency occurs, probably due to the suddenly stop of the shaker. This coupling of different modes was not encountered by simulations of the control-loop. However the dynamics of the beam behave differently when controlled compared to the natural damped system. Visible is that the first eigenmode is amplified by the control. In section 5.5 the delay sweep is shown, when the timing is 11 delay samples (which is used in this test), the controller damping coefficient is lower than a natural damped system. This shows that the first mode is amplified. Looking at the second sensor the influence of the first mode is less. This is as expected, because the curvature of the first mode is higher at the first sensor.

This mixed frequency response is also visible in the video. In the first mode every displacement peak was reduced by the damping-injection, this is not the case in the second mode test. The sensor's values and video are matching, however it was not possible to capture video frames and implement them in the report. To see the video, see the digital attachments. But the damping-injection control lacks the ability to damp first and second mode at the same time. This is confirmed with the frequency spectrum analysis of the sensors (figure 5.12). When the damping-injection is implemented the peak at the second eigenfrequency decreases, however the first eigenfrequency increases.

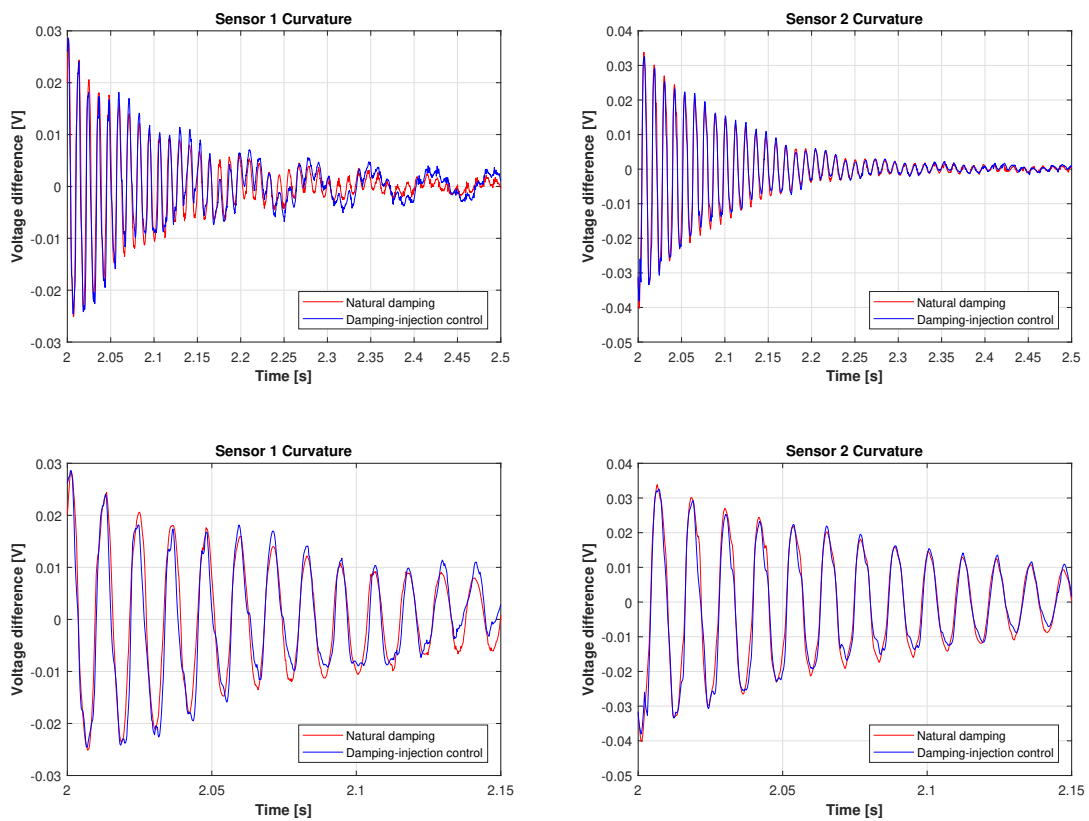


Figure 5.10: Second eigenfrequency excitation response (86.2 Hz) (A) First curvature sensor (B) Second curvature sensor; Voltage differential measurement in the case of natural damping and damping-injection control (video validation)

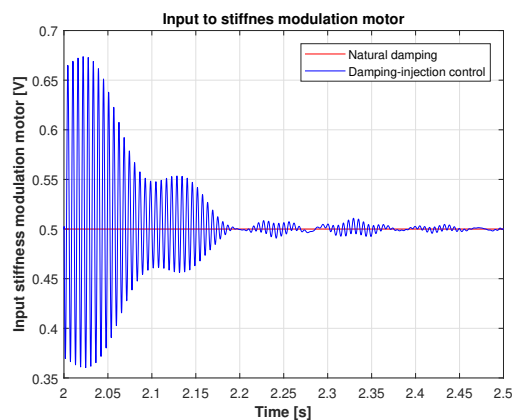


Figure 5.11: Input of the variable stiffness actuator, in the case of natural damping and damping-injection control (second eigenfrequency with video validation)

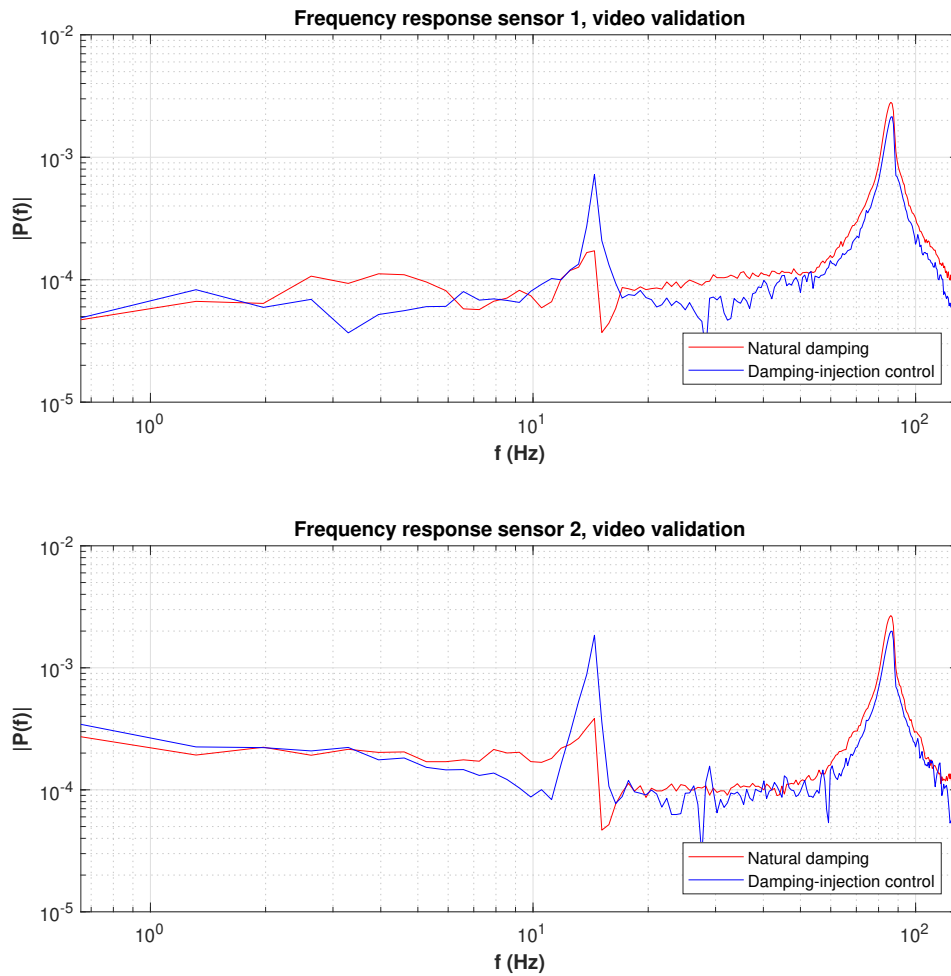


Figure 5.12: Frequency response from the sensors for the second mode. With damping-injection the second mode decreases and the first mode increases.

5.4 Effect of damping-injection

To understand how the vibrating beam behaves under damping-injection, the effect of the controller is tested. As explained in chapter 4.2.3 the damping coefficient quantifies the damping and for that reason will be approximated in this section.

The intention is to test the effect of the controlled system by tuning the gain of the control-loop. This can be tested by running multiple excitation responses with different control gains. The control gain is varied between 0 and 1. When the control gain is zero the control loop is turned off. When the control gain is at 1, a maximum current of 2.0A is allowed into the variable stiffness modulator. The test results are plotted in the same graph, figure 5.13. The differences between the signals is clearly visible from this plot. When the control gain increases, the curvature of the beam decreases and therefore also the deflection. This indicates that the control-loop is successfully applying damping-injection.

In the bottom graph of figure 5.13 the voltage difference between the natural response and controlled response is shown. At 2.1 s there is a difference of 0.012 V between the natural damped system and the highest control gain response. The voltage amplitude of the natural damped

system is 0.048 V, measured by the strain sensors. At 2.1 s the curvature amplitude is decreased by 25%.

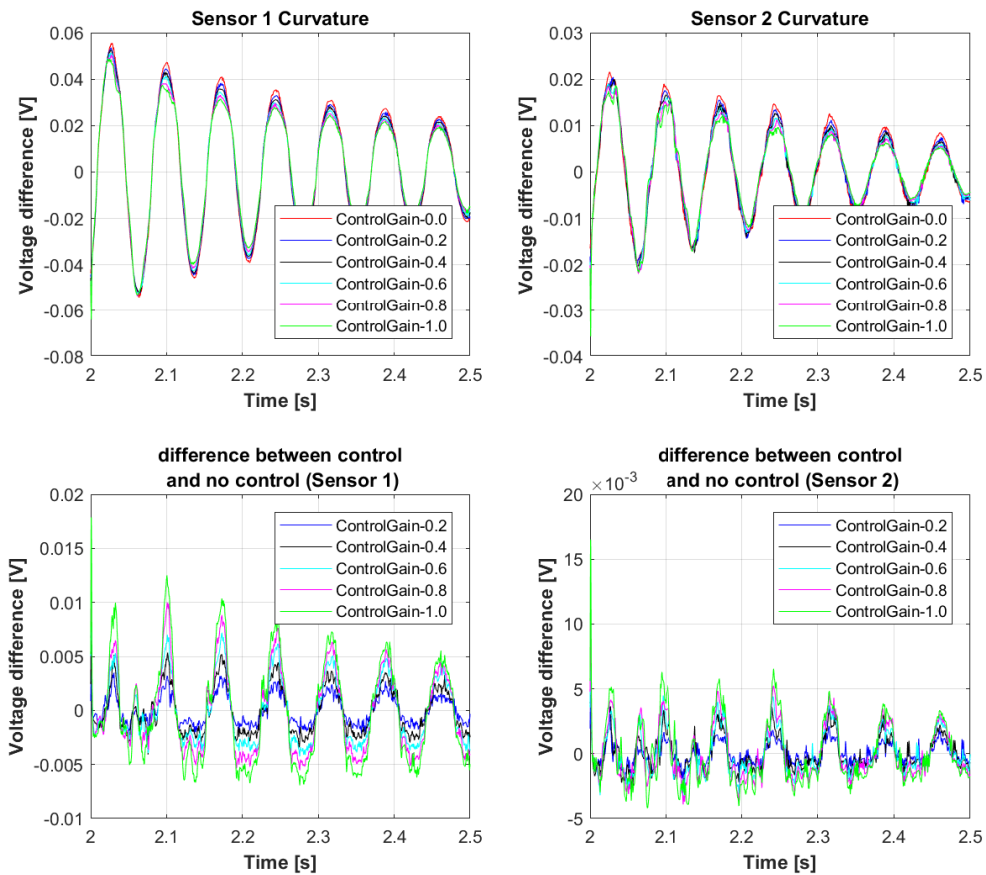


Figure 5.13: (A) Six excitation responses with different control gains (B) control signals subtracted by the natural damping signal (0 control gain)

As explained, the damping coefficient is desired. To get from the excitation response to the damping coefficient, first the envelope of the curvature peaks is needed. The envelope of the peaks is found by using the *envelope* function from the Matlab toolbox. This function determines the peak envelope using the spline interpolation to find the local maximums and minimums. The results is shown in figure 5.14.

From the envelope, the exponential decay of the signals can be approximated. Using the *Curve Fitting App (cftool)* from the Matlab toolbox, the exponential function is approximated. To see if the controlled system still results in an exponential decay, a logarithmic scale is used, to see if the resulting graph is linear. This result is shown in 5.15 The envelope will be fitted to the following exponential function:

$$y = ae^{bs} \quad (5.2)$$

With y the damping curve, a amplitude of the signal before damping, s is time in samples and b the damping coefficient. The damping coefficient results are shown in figure 5.16. The damping coefficient is linearly related to the control gain. This is very interesting, it means that the axial load and damping are related in a linear fashion. However when the control gain increases, the R^2 decreases (from 0.9939 to 0.9196), this means that the curve fitting error

increases. Because the error increases when the control gain increases, the exponential decay probably is changing differently than expected in equation 5.2.

Without control the damping coefficient is $3.6 \times 10^{-4} \text{ N s m}^{-1}$. When the control gain is one, the damping coefficient is $4.7 \times 10^{-4} \text{ N s m}^{-1}$ this is change of 16.7%.

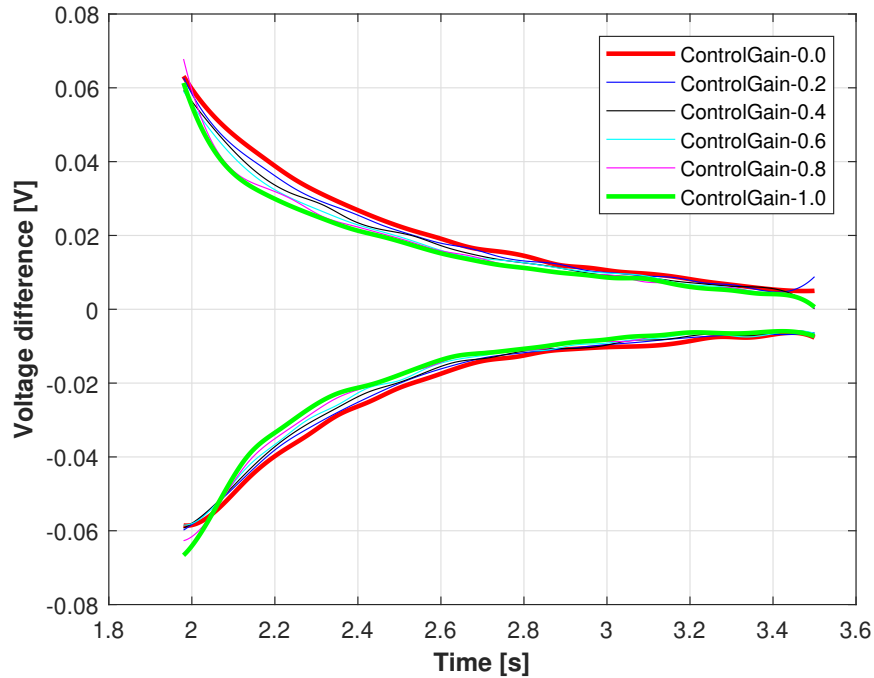


Figure 5.14: the envelope of the six different excitation responses

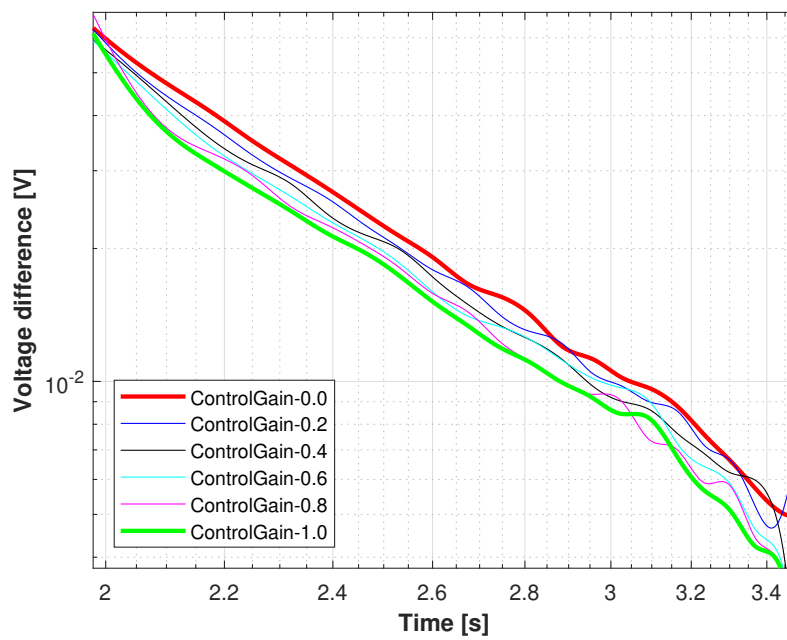


Figure 5.15: The envelopes of the six different excitation responses with logarithmic vertical axis. In the first 0.2 s the damping is the damping higher than in the natural situation. Close to zero the controller does not apply damping-injection

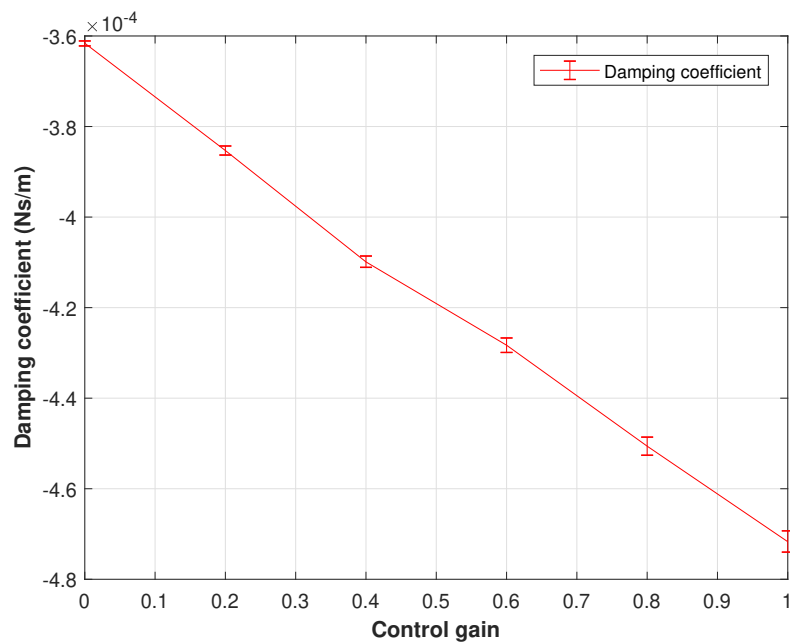


Figure 5.16: The damping coefficients plotted by the control gain; R^2 value left to right [0.9939, 0.9809, 0.9723, 0.9566, 0.9414, 0.9196]

5.5 Adaptability using control timing

The last experiment focuses on the adaptability by changing the control timing. This is done by varying the added delay in the control-loop. One control cycle in the first loop has 176 samples.

Therefore a delay sweep is done from 1 to 175 with steps of 25 samples and one test is done without control, which is used as reference. 25 samples is a delay of 0.005 s.

The first mode excitation response of the nine tests is shown in figure 5.17. The bold red line is the excitation response without control. The delay sweep results show, an increase in damping, but also a decrease in damping. With a sample delay of 75 samples the damping is the highest. From the upper curve-fit of the peaks a logarithmic plot is made, to check the exponential decay, shown in figure 5.18. The exponential decay is found and plotted in figure 5.19. Analyzing those figures shows that the controller can increase or reduce the natural damping, depending on the delay. The amplification is not within the scope of this project, but it can be interesting for future work. Figure 5.19 can also be compared with figure E.2. In this figure the damping-injection is simulated using parametric stiffness effects. In this figure only for a small timing window, damping-injection can be applied. This is also the case using the control law.

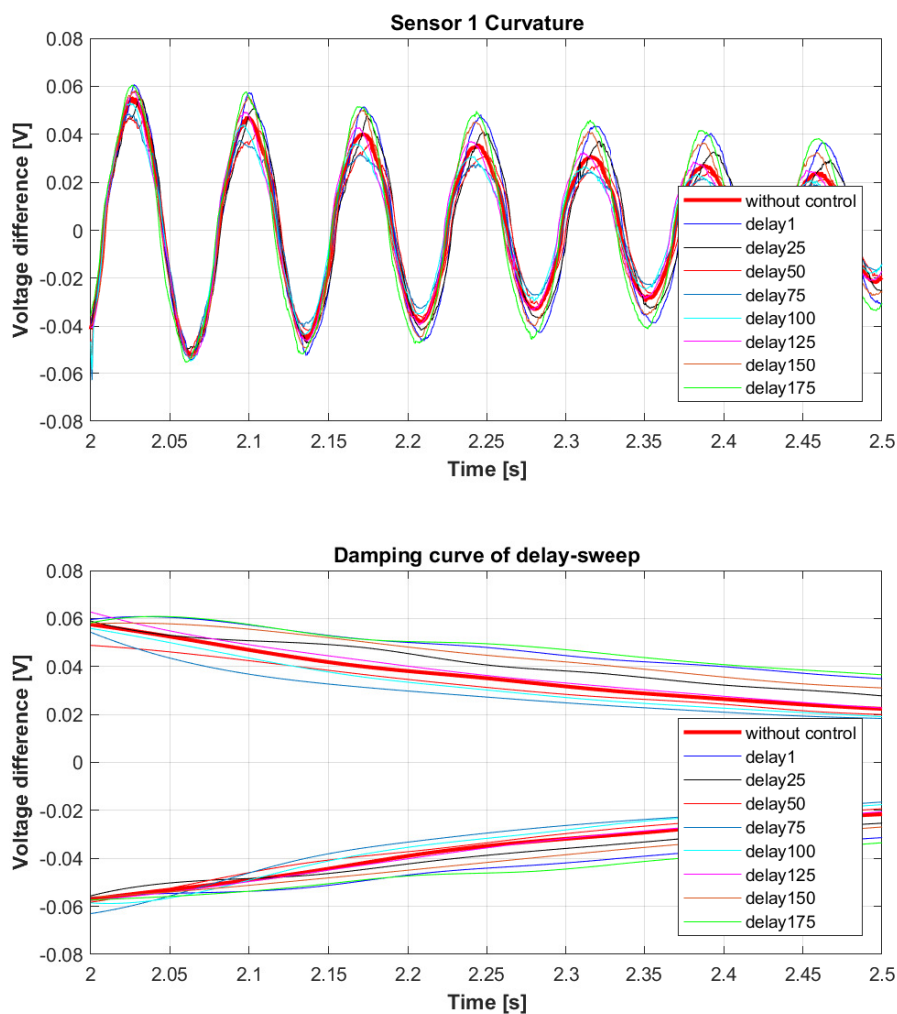


Figure 5.17: Top figure: Nine first mode excitation responses with time delay sweep; Bottom figure: Damping curve-fit using the peaks of the top figure

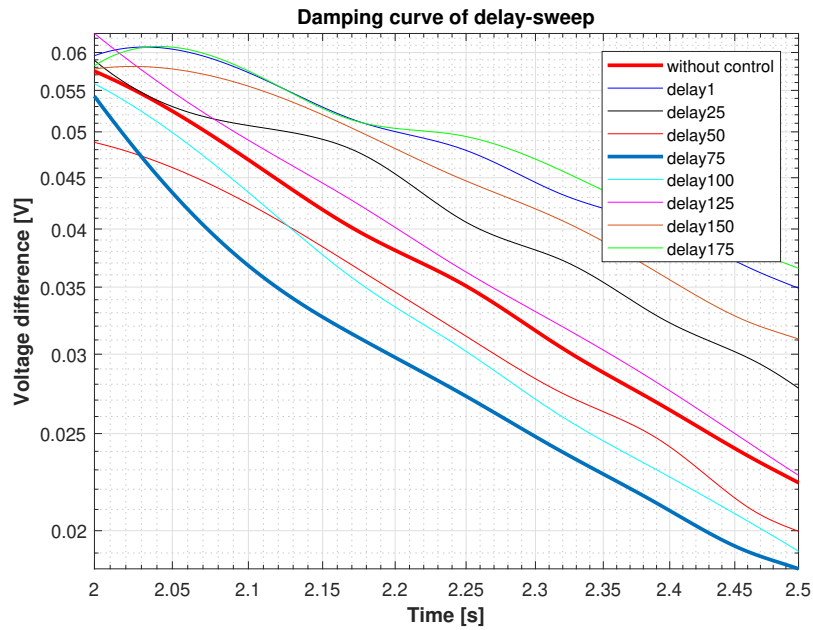


Figure 5.18: Upper damping curve-fit of the peaks in a logarithmic plot, to see exponential decay

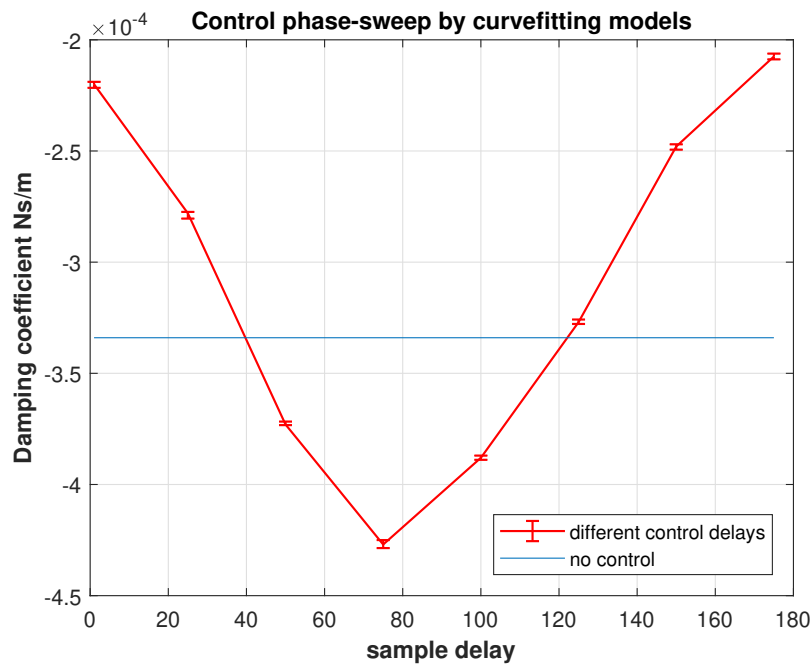


Figure 5.19: The damping coefficient of the delay-sweep; Error bars are the 95% confidence bound of the curve-fit tool

5.6 Conclusion

Various experiments have been performed and analysed. The goal of these tests is to answer the research questions. First the sensors are characterised. The performance of the sensors is sufficient to use them in the control-loop. Also the variable stiffness actuator is tested. The

last goal was to implemented damping-injection in different ways, varying the control gain and control timing. Those results will be discussed and concluded in the next chapter.

6 Discussion & Conclusion

The final part of this report is discussing and concluding the system. Which leads to recommendations for future work.

6.1 Discussion

In this chapter the analysis, design and test are discussed. The theories and models will be connected and motivated with the test results.

6.1.1 Control law by an axial load

In the analysis (chapter 2) two different types of longitudinal load induced softening are explored, the Euler- and Beck-type. From the variable stiffness analysis, the Beck-type boundaries are implemented into the port-Hamiltonian equation. This type was favored over the Euler-type, because then the wire could be implemented in a wing through a shaft. But after testing, the stiffness did not change as much as desired. Therefore the bow principle was introduced, which results in a change of the proposed control equation:

$$-\frac{Q(t)}{EI} w_t(L) \cdot \tan^{-1} \frac{w(L)}{L} - EI k \int_0^L w_t w_{xx} dx < 0 \quad (6.1)$$

However, this equation is not used in the tested controller. The shear boundary is different, as it depends on the variables: axial load, velocity and displacement. The value of this boundary will stay close to zero, because of the \tan^{-1} value. This value will always be small, due to small deflections. Therefore the controller accuracy could be further improved by implementing this equation in the setup. This could result in a better damped system.

6.1.2 Approximating the sign using embedded sensors

The tip position - sensor curve in figure 5.3 shows a sensor with minimal hysteresis. The curve still has non-linearities, but this does not influence the sign approximation for the control law. This is different from what was expected beforehand, the position - sensor curves of TPU are far more non-linear than those of PLA.

6.1.3 Port-Hamiltonian model in combination with imperfect sensors

So, it is known is that the sensors are not perfect; there are non-linearities in the signal. Therefore models are researched to compensate for those non-linearities [Kosmas et al., 2020]. However, in this research those models are not used. The small non-linearities are not a problem because the control law is only depending on the sign of the curvature. Thus, an error can only occur when the curvature is close to zero by measuring the wrong curvature sign. But when the curvature is close to zero, the gain of the sinusoidal control output is also close to zero. Therefore the proposed control law still works well despite the imperfect sensors .

6.1.4 First and Second mode interference

The video validation of the second mode experiment did not work as expected. This test was not as accurate as expected because the first mode was interfering. This mode is probably excited due to the suddenly stop of the shaker. Because the control timing could only be tuned to the first or second mode, a combination of modes is not possible with the built controller. However, in the frequency spectrum a decrease of the second eigenfrequency is visible. This shows that the second mode could also be damped.

6.1.5 Effect of damping-injection

The damping-injection was tested by varying the control gain. The damping coefficients of the different control gains is plotted in figure 5.16. At the maximum the damping is 25%. This shows that the controller works, however the controller should be improved to get critical damping. This has multiple reasons like: differences in boundary conditions, the change of effective stiffness in the beam is lower than analysed and the imperfect sensors.

6.1.6 Control timing

The timing of the controller at the beam vibration is very important to apply damping-injection. If the timing is off, the damping coefficient decreases, which leads to a less damped system. However, this can also be used as an advantage. This shows that the control law can also work to increase the amplitude. So this delay sweep shows not only damping increasing behaviour, but also damping decreasing behaviour. The non-linear sensors can affect the control timing. However, the non-linearity of the embedded sensors can be compensated by changing the time delay. But a mixture of modal excitations is not possible in the setup used in this research.

6.1.7 Parametric stiffness effects

In the design a comparison between the control law and parametric stiffness effects is mentioned. Because both systems can implement damping-injection in the experimented system, by controlling the stiffness of the beam with a sinusoidal frequency twice the vibrating frequency. Comparing figure 5.19 and figure E.2 shows similarities in control timing. However introducing damping by parametric stiffness can only be applied on a harmonic signal, this is not the case for the control law. The control law can be implemented in a non-periodic signal, however the controller design should be changed. The delay, should be changed to a lead-lag compensator [Verma et al., 2015]. Therefore this method is more general.

6.2 Conclusion

This study tries to answer the following research questions, which are related to the Portwings project:

1. *How can stiffness variations of a beam be influenced?* The first part of the analysis is focused on how the longitudinal load is influencing the stiffness of the beam. The eigenfrequencies are used to see how the beam behaves in two different setups. The Euler-type and Beck-type induced softening. From this analysis two setups are designed and tested: the bow principle and the wire trough the shaft principle. The wire through a shaft principle was initially favored because this design can be directly implemented into the bird wing. However, after "the dynamic behavior of the beam experiment" it was shown that the wire through a shaft principle did not work as expected. Therefore the rest of the experiments was conducted using the bow principle. The bow principle did work, the stiffness could be changed and therefore, damping-injection is applied by changing the stiffness.
2. *How can 3D-printed embedded sensors be used to determine the flapping dynamics?* First the results of question one will be concluded. From existing 3D-printed projects, a lot of information has been used. This is used to print a beam with embedded sensors. A difference in previous work is the strain sensor lay-out: the side way paths have been printed in a single path to reduce the resistance. Also the differential sensing, which is researched in the work of [Schouten et al., 2020], improved the linearity of the sensors.

Looking at the tip position - sensor measurements, the hysteresis is minimal. However non-linearity is shown in results, which can affect the zero-crossing. The sign can be

measured incorrectly by measuring the wrong zero-crossing. This can be counteracted by changing the delay of the control-loop. Because the zero-crossing error will be constant over the experiment.

3. *What beam behaviour (modifications) can be obtained using beam controlled stiffness variations?* The controller gain can vary the stiffness actuation. The damping which is applied by the controller is linearly dependent on the controller gain. Therefore it is possible to modify the beam behaviour with stiffness variations. The timing of the controlled stiffness modulation is also important to apply damping-injection. The timing is critical for damping-injection, but it is also promising looking at decreasing damping. By changing the timing a decrease in damping is possible, which can be used in the closed-loop control for the mechanical bird.
4. *Can port-Hamiltonian modelling be used to design a stabilising control law for flexible beams and how?* The results of experiment "effect of damping-injection" conclude that energy-based control is a suitable method to model this complex setup. By using the derivative of the Hamiltonian, a control law is found, which can control the stiffness of the beam, by only using the embedded strain sensors. Looking at the results the controller damps the system.

The integral of the control law is dependent on the curvature and velocity of the beam. The curvature is measured at two positions at the beam. With the curvature shape of the first or second mode, the curvature of the beam is approximated. This is also done for the displacement. The displacement curve is differentiated to the velocity. Using those the control output is calculated. However attention should be paid to higher frequencies, because differentiating a noisy displacement signal ends up in a unusable velocity signal.

Looking at the whole project, the proposed control law is able to control the vibrating beam. Using damping-injection ensures stability [Melchiorri et al., 1999]. From here it is possible to improve the system, so not only damping-injection is applied on the system. Other possibility could be, to increase the flapping amplitude.

6.3 Future work

In future work, this study can proceed in different aspects:

- Increase the complexity of the wing model. In this research a 1D-beam is used as framework. If the model dimensions are increased, multiple loads can be applied, such as lift and twist by the aerodynamic foil shape.
- At this moment only damping-injection is researched. However in the control timing results (5.5) a decrease in damping is also found to be possible. Therefore it is interesting to dive deeper in the derivative of the Port-Hamiltonian model. Instead of damping, it could be possible to amplify the system. If this is possible the system could be more energy efficient than an open-loop system. However a study is needed to see if it is possible to overcome the natural damping of the system by means of the proposed. And also the amount of energy used by the variable stiffness actuation should be researched.
- In the design 3.3.2 it is already shown that the shear force boundary could be improved. In future work this difference can be studied and improved. This will increase the effect of the control law.
- In flapping flight control it is also interesting to look at parametric stiffness effects. If the parametric stiffness effects are used, the controller could be simplified even more. When using parametric stiffness to control the system, only the timing and frequency are

important, because the controller output is only a sinusoidal which does not depend on the measurement of a strain sensor. This could be measured using an encoder.

- From the frequency sweep, the first mode in the z -direction is measured. For the given symmetric structure relative to the midline of the beam, with linear sensors this can not be measured. Knowing this, the sensors could be used in different setups. It can also measure displacement in the z -direction. A problem occurs is, which component is measured.
- The controller signal is a sinusoidal signal, this is used so the system is linear. However, in theory a bang-bang controller could be more effective. This is because the stiffness change is maximal in both directions for a longer time.
- The variable stiffness actuator changes the stiffness. By using a DC-motor the axial load is applied to the beam. This motor is quite heavy and energy inefficient. If a variable stiffness mechanism is used which uses less energy and a higher stiffness change, the system can be improved. For instance by continuing the work of Melandri [Meleandri et al., 2020] on distributed variable stiffness mechanisms.
- In this work an artificial delay is implemented in the control-loop, so the control time is a cycle later. This works in a harmonic setup, however, in a non-harmonic system the artificial delay will not work. The delay by the system can be compensated using a lead-lag compensator.

A Euler-Bernoulli beam theory assumptions

The Euler-Bernoulli beam theory can model the deformations of a beam [Labuschagne et al., 2009]. This theory was developed around 1750 and is still one of the methods which is used most to analyse the behavior of bending beams.

In the Euler-Bernoulli theory it is assumed that the modelled beam is slender, therefore the shear deformations are neglected. To use the Euler-Bernoulli theory the next assumptions are made [Labuschagne et al., 2009]:

- The plane sections remain plane and normal to the longitudinal axis in every finite element of the beam.
- The beam is linear elastic, isotropic and the Poisson's ratio effects are ignored.
- The deformed angles (slope) of the beam are small. if x is the location along the beam length, and $w(x)$ is the displacement of the beam at position x the slope(α) will become:

$$\alpha = \frac{dw}{dx} \quad (\text{A.1})$$

Knowing that the deformed angles are small, the square of the slope will even be smaller, and can be assumed as zero. See equation A.2

$$\alpha^2 = \left(\frac{dw}{dx}\right)^2 \approx 0 \quad (\text{A.2})$$

Now, referring back to angles looking at small changes using a Taylor expansion, the following assumptions can be made :

$$\begin{aligned} \sin \alpha &\approx \alpha \\ \cos \alpha &\approx 1 \end{aligned} \quad (\text{A.3})$$

Based on those assumptions the Euler-Bernoulli Theory results in the following equation:

$$-\frac{d^2w}{dx^2} = \frac{M(x)}{EI} \quad (\text{A.4})$$

Here $\frac{d^2w}{dx^2}$ is the second derivative of the deflection of the beam, M is the internal moment in the beam over the length, E is the Young's modulus and, lastly, I is the moment of inertia of the cross-section.

B Tables of eigenfrequency change by axial load

In this appendix the tables of Euler-type, Beck-type and Solidworks simulations of axial load - eigenfrequency are shown.

Load [N]	first eigenfrequency[Hz]	second eigenfrequency[Hz]
0	15.2	95.5
0.5	14.2	94.8
1	13.1	93.6
1.5	11.9	92.5
2	10.5	91.4
2.5	8.9	90.1
3	6.8	89
3.5	3.5	87.8
3.6	2.4	87.6
3.65	1.6	-
5	-	84.2
10	-	71.1
15	-	56.3
20	-	41.2

Table B.1: Euler-type softening calculated eigenfrequency change dependent on the axial load

Load [N]	first eigenfrequency[Hz]	second eigenfrequency[Hz]
0	15.2	95.6
4	16.8	92.2
8	18.4	88.2
12	20.8	84
16	23.2	79.3
20	26.2	74.2

Table B.2: Beck-type softening calculated eigenfrequency change dependent on the axial load

Load [N]	first eigenfrequency[Hz]	second eigenfrequency[Hz]
0	13.5	84.684
4	10.8	81.9
8	6.7	79.1
10	2.7	77.6
12	-	-

Table B.3: Solidworks simulations of the Euler-type softening; eigenfrequency change dependent on the axial load

C 20-Sim code

Block: *beam_mode_equation1*

```

parameters
  real global L;          // beam length [cm]
  real global M1;        //mode of the beam
  real global initial;   // initial value
  integer num_points = 30; //elements of beam

variables
  real x[num_points];
  integer i;
  real Lambda;
  real omega;
  real disp_mode[num_points];
  real curve_mode[num_points];
initialequations
  Lambda = (1.8751 / L) * M1; //mode
  omega = Lambda^2;

  for i = 1 to num_points do
    x[i] = L*i/num_points;
  end;
for i = 1 to num_points do

  disp_mode[i] = (cosh(Lambda*x[i])-cos(Lambda*x[i]) -
  (cos(Lambda*L)+cosh(Lambda*L)) / (sin(Lambda*L)+
  sinh(Lambda*L)) * (sinh(Lambda*x[i])-sin(Lambda*x[i])));
  //theoretical displacement shape
  curve_mode[i] = Lambda^2*cos(Lambda*x[i]) +
  Lambda^2*cosh(Lambda*x[i]) - ((cos(L*Lambda) +
  cosh(L*Lambda)) * (Lambda^2*sin(Lambda*x[i]) +
  Lambda^2*sinh(Lambda*x[i])))/(sin(L*Lambda) + sinh(L*Lambda));
  //theoretical curvature shape

  curv[i]= curve_mode[i];
  disp[i]= disp_mode[i];
end;

```

Block: *curve_model_model*

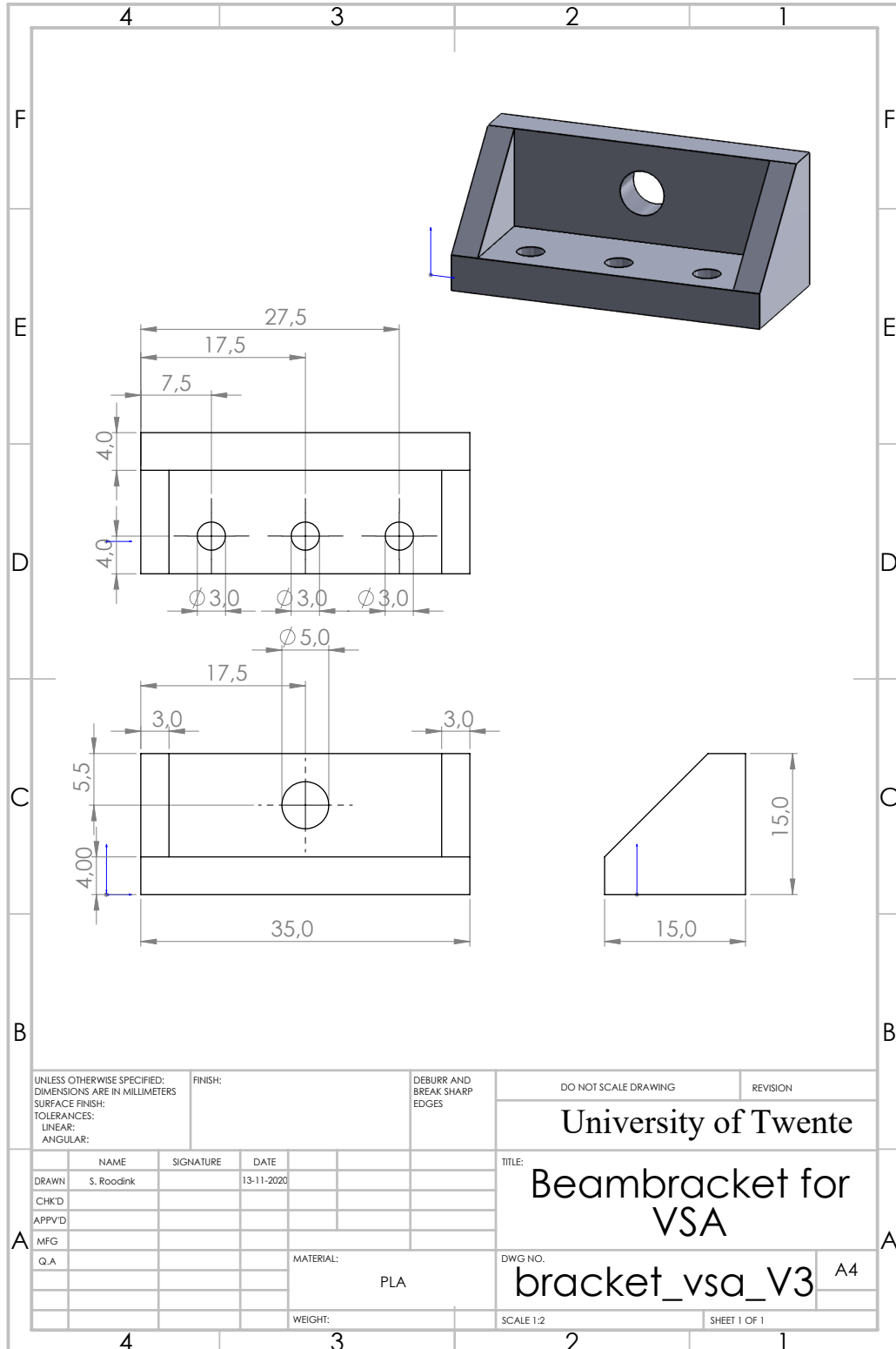
```
parameters
  integer global Position_sens1;
  integer global Position_sens2;
  integer global Sensors_number;
  integer num_points = 30;
variables
  real gain_sens1;      //sensor value1
  real gain_sens2;      //sensor value2
  real gain;
  real curv_sens_model[num_points];
  real disp_sens_model[num_points];

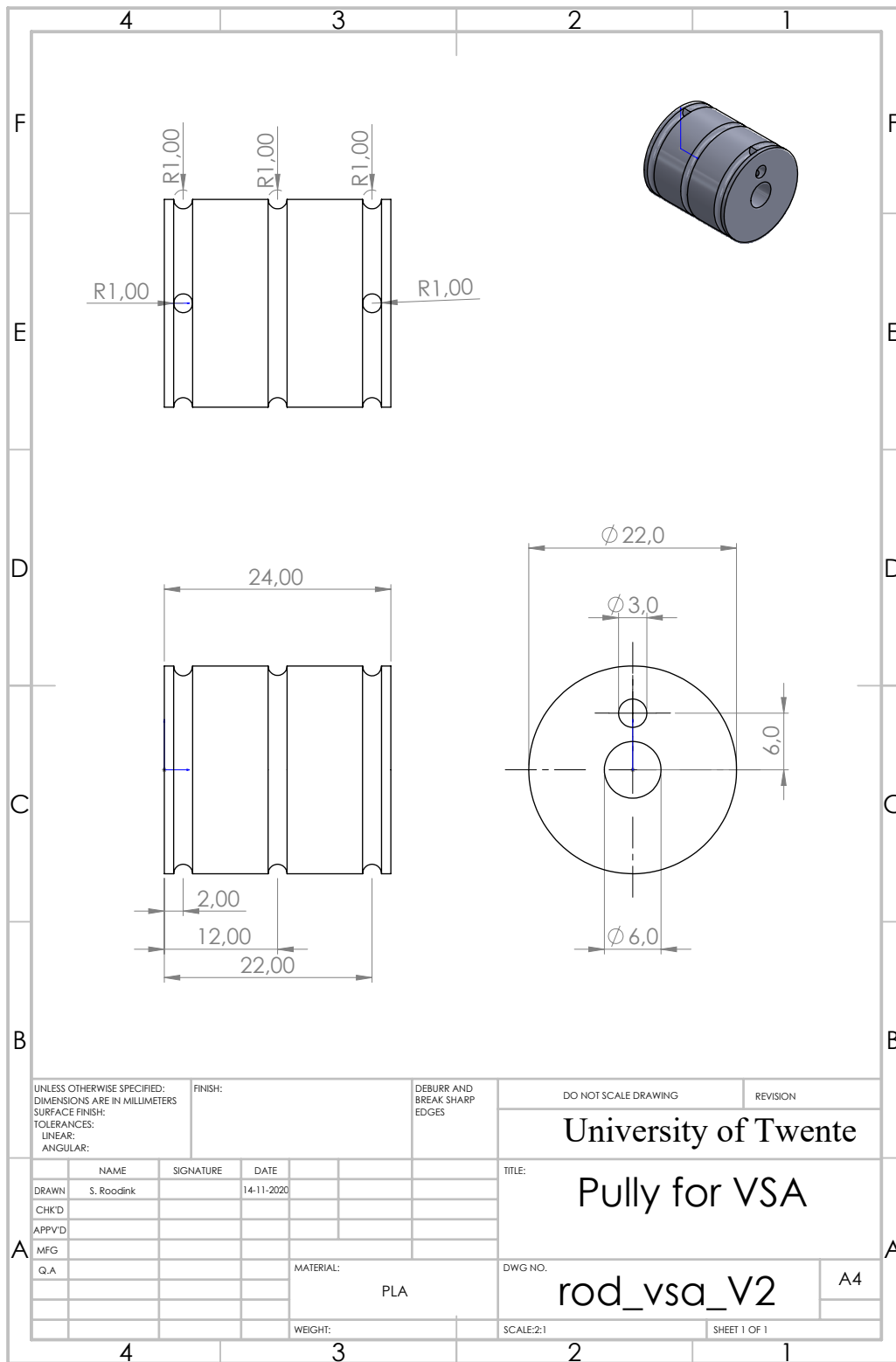
equations

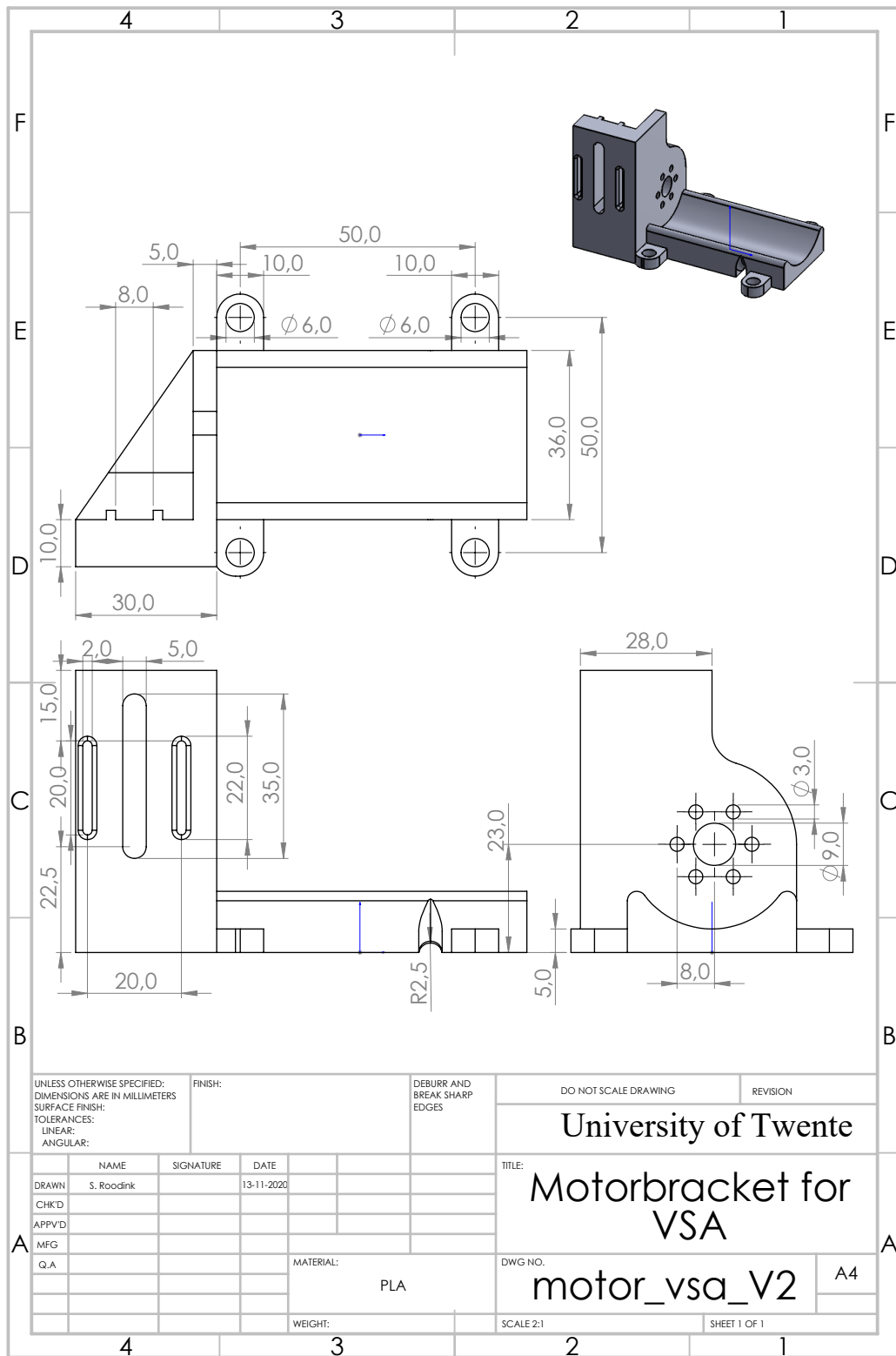
gain_sens1= input_sens1 / Curv_model[Position_sens1];
gain_sens2= input_sens2 / Curv_model[Position_sens2];
av_gain= (gain_sens1+gain_sens2)/Sensors_number;
// find sign gain of two positions

curv_sens_model=Curv_model*gain; //curve model
disp_sens_model=Disp_model*gain; //displacement model
Output_curv=curv_sens_model;
Output_disp=disp_sens_model;
```

D CAD drawings







E Damping of a beam by parametric stiffness

In this report damping injection by means of varying the stiffness through applying an axial load is researched. However, it is also possible to parametrically vary the stiffness for periodic excitation. This is studied for damping among others by Dohnal, with parametric anti-resonance [Dohnal, 2012]. This appendix presents a brief study of damping through parametric stiffness.

E.1 1 Degree of Freedom approximation cantilever

A one degree of freedom (DoF) approximation is used to model the first eigenmode vibration of the cantilever beam (figure E.1). A simple approximation of a harmonic oscillator is found in [vlab.amrita, 2011]. The deflection h of the tip of the cantilever can be modelled by:

$$m_{\text{eff}}\ddot{h} + \gamma\dot{h} + k_0h = F_0 \cos(\omega_s t) \quad (\text{E.1})$$

$$m_{\text{eff}} \frac{\partial^2 h}{\partial t^2} + \gamma \frac{\partial h}{\partial t} + k_0 h = F_0 \cos(\omega_s t) \quad (\text{E.2})$$

With:

- The effective mass of an oscillating cantilever in first mode can be approximated as a mass at the tip by: $m_{\text{eff}} \approx \frac{33}{140} m_{\text{beam}}$
- The stiffness of a cantilever is approximated through beam theory by (assuming the effective mass acts at the tip of the cantilever): $k_0 = \frac{3EI}{L^3}$
- A linear damping of γ is assumed
- The system is excited by a harmonic force with amplitude F_0 and angular frequency ω_s

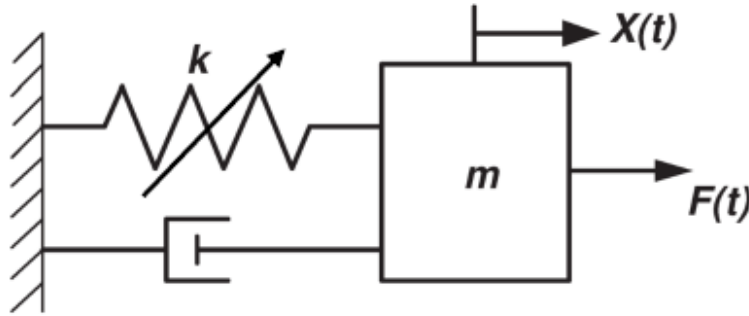


Figure E.1: 1 DoF model of the cantilever beam

E.2 Parametric stiffness

The parametric pumping (varying the stiffness) in this example is applied by an axial load, to increase or decrease the stiffness of the beam. For parametric damping, the pumping frequency should be twice as high as the cantilever vibration frequency. Important parameters are:

- k_p , the pumping stiffness variation

- ϕ , is the delay of the pumping frequency with respect to the period of the vibration frequency. The control timing gets into the equation through substituting a shift in time Δt , which results in:

$$2\omega_s(t + \Delta t) = 2\omega_s t + 2\omega_s \Delta t = 2\omega_s t + 2\phi \quad (\text{E.3})$$

The parametric oscillator will have the form of the damped Mathieu equation:

$$m\ddot{h} + \gamma\dot{h} + (k_0 - k_p \cos(2\omega_s t + 2\phi)) h = F_0 \cos(\omega_s t) \quad (\text{E.4})$$

this is rewritten to e by Euler's formula:

$$m\ddot{h} + \gamma\dot{h} + \left(k_0 - \frac{k_p}{2} \left(e^{j2\omega_s t} e^{2\phi} - e^{-j2\omega_s t} e^{-2\phi} \right) \right) h = \frac{F_0}{2} \left(e^{j\omega_s t} + e^{-j\omega_s t} \right) \quad (\text{E.5})$$

The interaction of the vibration signal and the pumping signal causes parametric frequency mixing in the solution. Besides the driving frequency $\pm\omega_s$, also the frequency $\pm 3\omega_s$ will be present. Therefore the Mathieu equation cannot be expressed in terms of solutions for a second-order linear ordinary differential equation. To find an analytical approximation, the method of harmonic balancing will be used.

E.3 Harmonic balancing

The parametric mixing introduces higher harmonics into the system. However, due to the attenuation above the resonance frequency of the system, only the first higher modes have to be considered. Harmonic balancing is a method for approximating the analytical solutions by limiting the analysis only to the most important frequencies (so higher order frequency terms are truncated). Due to the linear nature in h of the Mathieu equation, the oscillations at different frequencies are a linear combination and therefore the analytical approximation can be found by "balancing" the frequency terms $\pm\omega_s$ and $\pm 3\omega_s$. A nice application of this method on an electromechanical system with parametric stiffness can be found in [Droogendijk et al., 2013].

The solution h will be of the following form:

$$h(t) = h_1 e^{j\omega_s t} + h_2 e^{-j\omega_s t} + h_3 e^{j(3\omega_s t)} + h_4 e^{-j(3\omega_s t)} \quad (\text{E.6})$$

The system of equations can be written as a linear system of coupled differential equations, with one equation for every frequency i . Which leads to:

$$\begin{aligned} (-m\omega_i^2 + j\gamma\omega_i + k_0) h_i - \frac{k_p}{2} \left(e^{j2\omega_s t} e^{2\phi} - e^{-j2\omega_s t} e^{-2\phi} \right) h_i \\ = \frac{F_0}{2} \left(e^{j\omega_s t} \delta(\omega_i - \omega_s) + e^{-j\omega_s t} \delta(-\omega_i + \omega_s) \right) \end{aligned} \quad (\text{E.7})$$

The δ -function is required to only express the driving force at the excitation frequency. Furthermore the following constants are defined: $g_i = -m\omega_i^2 + j\gamma\omega_i + k_0$, $a_1 = \frac{k_p}{2} e^{j2\phi}$, $a_2 = \frac{k_p}{2} e^{-j2\phi}$, $b = \frac{F_0}{2}$. This simplifies the equations to:

$$g_i h - a_1 e^{j2\omega_s t} h - a_2 e^{-j2\omega_s t} h = b e^{j\omega_s t} \delta(\omega_i - \omega_s) + b e^{-j\omega_s t} \delta(-\omega_i + \omega_s) \quad (\text{E.8})$$

The matrix of linear equations becomes:

$$\begin{bmatrix} g_1 & -a_1 & -a_2 & 0 \\ -a_2 & g_2 & 0 & -a_1 \\ -a_1 & 0 & g_3 & 0 \\ 0 & -a_2 & 0 & g_4 \end{bmatrix} \begin{bmatrix} h_1 \\ h_2 \\ h_3 \\ h_4 \end{bmatrix} = \begin{bmatrix} b \\ b \\ 0 \\ 0 \end{bmatrix} \quad (\text{E.9})$$

To determine the coefficients h_i , $\mathbf{h} = [\dots]^{-1} \mathbf{b}$ needs to be solved:

$$\begin{bmatrix} h_1 \\ h_2 \\ h_3 \\ h_4 \end{bmatrix} = \frac{\mathbf{b}}{a_1^2 a_2^2 - a_1 a_2 (g_1 g_3 + g_4 (g_2 + g_3)) + g_1 g_2 g_3 g_4} \begin{bmatrix} -a_1 a_2 g_3 + a_1 g_3 g_4 + g_2 g_3 g_4 \\ -a_1 a_2 g_4 + a_2 g_3 g_4 + g_1 g_3 g_4 \\ a_1^2 (-a_2) + a_1^2 g_4 + a_1 g_2 g_4 \\ -a_1 a_2^2 + a_2^2 g_3 + a_2 g_1 g_3 \end{bmatrix} \quad (\text{E.10})$$

This equation is solved in Matlab, using the parameters from the table 2.1 and the amplitude of $k_p = 7,32$. This results in the following, which will be compared to the control timing plot in figure 5.19:

The gain due to parametric stiffness is determined with:

$$\text{Gain} = \frac{|h_1|}{|h_1(k_p = 0)|} \quad (\text{E.11})$$

The solution can be found in figure E.2 (the magnitude of h_3 was also calculated, but is very small compared to h_1). It becomes clear that the parametric stiffness can give rise to both damping and amplification, depending on the phase of the stiffening with respect to the harmonic excitation.

Looking at the two methods, damping by parametric stiffness and damping by the control law, both are dependent on the timing of stiffness varying compared to the vibration frequency. However the parametric stiffening is only applicable at sinusoidal harmonic signals. This is not the case using the control law, this can also be implemented in a more general case. However in the test setup a harmonic signal is controlled.

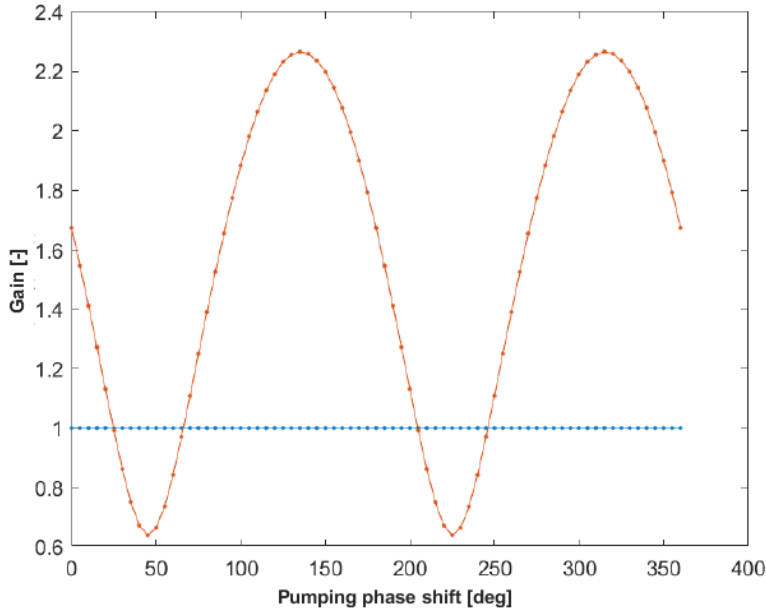


Figure E.2: Simulated gain of the amplitude with parametric stiffness divided by the amplitude without parametric stiffness

F Amplifier circuit

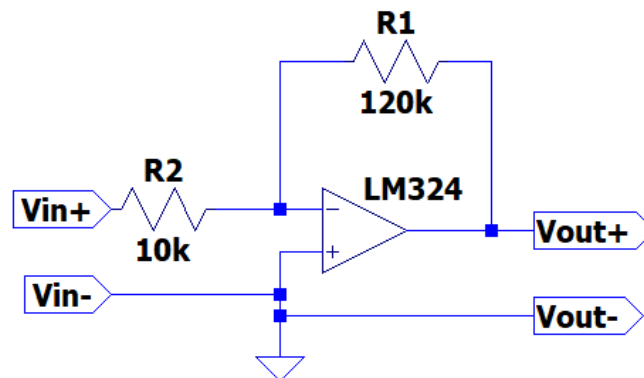


Figure F.1: 12x Amplifier circuit for the variable stiffness actuator; the LM324 op-amp is used as amplifier

Bibliography

- [3Dilla, 2020] 3Dilla (2020), Fused deposition modeling.
<https://fr.3dilla.com/imprimante-3d/fused-deposition-modeling/>
- [Bruno Bruderer, Dieter Peter, Andreas Boldt, Felix Liechti, 2010] Bruno Bruderer, Dieter Peter, Andreas Boldt, Felix Liechti (2010), Wing-beat characteristics of birds recorded with tracking radar and cine camera.
<https://doi.org/10.1111/j.1474-919X.2010.01014.x>
- [Chamil Abeykoon, 2020] Chamil Abeykoon, Pimpisut Sri-Amphorn, A. F. (2020), Optimization of fused deposition modeling parameters for improved PLA and ABS 3D printed structures.
<https://www.sciencedirect.com/science/article/pii/S2588840420300196>
- [Christ et al., 2017] Christ, J. F., C. J. Hohimer, N. Aliheidari, A. Ameli, C. Mo and P. Pötschke (2017), 3D printing of highly elastic strain sensors using polyurethane/multiwall carbon nanotube composites, in *Sensors and Smart Structures Technologies for Civil, Mechanical, and Aerospace Systems 2017*, volume 10168, Ed. J. P. Lynch, International Society for Optics and Photonics, SPIE, pp. 70 – 76, doi:10.1117/12.2259820.
<https://doi.org/10.1117/12.2259820>
- [Diabase Engineering, 2020] Diabase Engineering (2020), *Diabase H-series*.
<https://www.diasemachines.com/hseries>
- [Dijkshoorn et al., 2020] Dijkshoorn, A., M. Schouten, G. Wolterink, R. Sanders, S. Stramigioli and G. Krijnen (2020), Characterizing the Electrical Properties of Anisotropic, 3D-Printed Conductive Sheets for Sensor Applications, *IEEE sensors journal*, ISSN 1530-437X, doi:10.1109/JSEN.2020.3007249.
- [Dijkshoorn et al., 2018] Dijkshoorn, A., P. Werkman, M. Welleweerd, G. Wolterink, B. Eijking, J. Delamare, R. Sanders and G. J. M. Krijnen (2018), Embedded sensing: integrating sensors in 3-D printed structures, **vol. 7**, no.1, pp. 169–181, doi:10.5194/jsss-7-169-2018.
<https://jsss.copernicus.org/articles/7/169/2018/>
- [Dohnal, 2012] Dohnal, F. (2012), Dissipative Energy Flow in Systems at Parametric Anti-Resonance, doi:10.1115/DETC2012-70864.
- [Douglas et al., 2015] Douglas, A., J. Bahlman, R. Dakin, A. Gaede, B. Goller, D. Lentink, P. Segre and D. Skandalis (2015), The biophysics of bird flight: Functional relationships integrate aerodynamics, morphology, kinematics, muscles, and sensors, *Canadian Journal of Zoology*, **vol. 93**, doi:10.1139/cjz-2015-0103.
- [Droogendijk et al., 2013] Droogendijk, H., R. Sanders and G. Krijnen (2013), Uncovering signals from measurement noise by electro mechanical amplitude modulation, *New Journal of Physics*, **vol. 15**, p. 053029, doi:10.1088/1367-2630/15/5/053029.
- [Dumstorff et al., 2014] Dumstorff, G., S. Paul and W. Lang (2014), Integration Without Disruption: The Basic Challenge of Sensor Integration, **vol. 14**, no.7, pp. 2102–2111, doi:10.1109/JSEN.2013.2294626.

- [E. Cheynet, 2020] E. Cheynet (2020), ECheynet/eigenBeam v1.6, doi:10.5281/ZENODO.3817909.
<https://zenodo.org/record/3817909>
- [Folkertsma and Stramigioli, 2017] Folkertsma, G. and S. Stramigioli (2017), Energy in Robotics, **vol. 6**, no.3, pp. 140–210, ISSN 1935-8253, doi:10.1561/23000000038.
- [Gumstix, 2020] Gumstix (2020), *Gumstix Overo Hardware*.
<https://www.gumstix.com/community/support/hardware/overo/>
- [H. Jayasinghe, 2013] H. Jayasinghe, M. T. Kashani, S. H. (2013), THE EFFECTS OF AXIAL LOAD AND END MOMENT ON THE FLEXURAL – TORSIONAL VIBRATIONAL AND STABILITY CHARACTERISTICS OF BEAMS.
https://www.researchgate.net/publication/260002138_THE_EFFECTS_OF_AXIAL_LOAD_AND_END_MOMENT_ON_THE_FLEXURAL_-_TORSIONAL_VIBRATIONAL_AND_STABILITY_CHARACTERISTICS_OF_BEAMS
- [Han et al., 2016] Han, J., G. Waddington, R. Adams, J. Anson and Y. Liu (2016), Assessing proprioception: A critical review of methods, **vol. 5**, no.1, pp. 80 – 90, ISSN 2095-2546, doi:<https://doi.org/10.1016/j.jshs.2014.10.004>.
<http://www.sciencedirect.com/science/article/pii/S2095254615000058>
- [Kosmas et al., 2020] Kosmas, D., M. Schouten and G. Krijnen (2020), Hysteresis Compensation of 3D Printed Sensors by a Power Law Model with Reduced Parameters, in *2020 IEEE International Conference on Flexible and Printable Sensors and Systems (FLEPS)*, pp. 1–4, doi:10.1109/FLEPS49123.2020.9239580.
- [Labuschagne et al., 2009] Labuschagne, A., N. van Rensburg and A. van der Merwe (2009), Comparison of linear beam theories, doi:<https://doi.org/10.1016/j.mcm.2008.06.006>.
<http://www.sciencedirect.com/science/article/pii/S0895717708002112>
- [Makeitform, 2020] Makeitform (2020), PLA Properties.
<https://www.makeitfrom.com/material-properties/Polylactic-Acid-PLA-Polylactide>
- [Malzer et al., 2019] Malzer, T., H. Rams and M. Schöberl (2019), Energy-Based In-Domain Control of a Piezo-Actuated Euler-Bernoulli Beam**This work has been supported by the Austrian Science Fund (FWF) under grant number P 29964-N32., **vol. 52**, no.2, pp. 144 – 149, ISSN 2405-8963, doi:<https://doi.org/10.1016/j.ifacol.2019.08.025>, 3rd IFAC Workshop on Control of Systems Governed by Partial Differential Equations CPDE 2019.
<http://www.sciencedirect.com/science/article/pii/S2405896319303453>
- [Maurizi et al., 2019] Maurizi, M., J. Slavič, F. Cianetti, M. Jerman, J. Valentinčič, A. Lebar and M. Boltežar. (2019), Dynamic Measurements Using FDM 3D-Printed Embedded Strain Sensors., , no.12, p. 15, doi:10.3390/s19122661.
<https://doi.org/10.3390/s19122661>
- [Maxon motors, 2014] Maxon motors (2014), Maxon DC motor and Maxon EC motor.
https://www.maxongroup.com/medias/sys_master/8815460712478.pdf
- [Maxon motors, 2020] Maxon motors (2020), *Maxon ADS 50/5 4-Q-DC*.
<https://www.maxongroup.com/maxon/view/product/145391>

- [MB Dynamcis, 2020] MB Dynamcis (2020), *PM-Series shakers*.
<https://www.mbdynamics.com/products/shaker-systems/pm-series/>
- [Melchiorri et al., 1999] Melchiorri, C., S. Stramigoli and S. Andreotti (1999), Using damping injection and passivity in robotic manipulation, in *1999 IEEE/ASME International Conference on Advanced Intelligent Mechatronics (Cat. No.99TH8399)*, pp. 979–984, doi:10.1109/AIM.1999.803305.
- [Meleandri et al., 2020] Meleandri, G., V. P. Castelli, S. Stramigoli, A. Dijkshoorn, R. Vertechy and N. Sancisi (2020), Study of novel solution to obtain controllable stiffness for beam-like elements.
<https://amslaurea.unibo.it/id/eprint/20196>
- [Nassar et al., 2018] Nassar, H., M. Ntagios, W. T. Navaraj and R. Dahiva (2018), Multi-Material 3D Printed Bendable Smart Sensing Structures, in *2018 IEEE SENSORS*, pp. 1–4, doi:10.1109/ICSENS.2018.8589625.
- [NinjaTek, 2020] NinjaTek (2020), Ninjaflex datasheet.
<https://ninjatek.com/wp-content/uploads/2019/10/NinjaFlex-TDS.pdf>
- [Ortega et al., 2001] Ortega, R., A. van der Schaft, I. Mareels and B. Maschke (2001), Putting energy back in control, **vol. 21**, no.2, pp. 18–33, ISSN 1066-033X, doi:10.1109/37.915398.
- [Pecho et al., 2019] Pecho, P., V. Ažaltovič, B. Kandra and M. Bugaj (2019), Introduction study of design and layout of UAVs 3D printed wings in relation to optimal lightweight and load distribution, *Transportation Research Procedia*, **vol. 40**, pp. 861 – 868, ISSN 2352-1465, doi:<https://doi.org/10.1016/j.trpro.2019.07.121>, tRANSCOM 2019 13th International Scientific Conference on Sustainable, Modern and Safe Transport.
<http://www.sciencedirect.com/science/article/pii/S2352146519302881>
- [Peter Myler, Leslie M. Wyatt, 1994] Peter Myler, Leslie M. Wyatt (1994), *Mechanical Engineer's Reference Book (Twelfth Edition)*.
<https://doi.org/10.1016/B978-0-7506-1195-4.50012-9>
- [Rao, 2017] Rao, S. (2017), *Mechanical Vibrations*, Pearson Education, Incorporated, ISBN 9780134361307.
<https://books.google.nl/books?id=t6gHswEACAAJ>
- [Roodink, 2017] Roodink, S. (2017), Large-range active load for dynamic motor testing.
<http://essay.utwente.nl/74337/>
- [Schouten et al., 2020] Schouten, M., B. Prakken, R. Sanders and G. Krijnen (2020), Linearisation of a 3D printed flexible tactile sensor based on piezoresistive sensing, in *2019 IEEE Sensors*, IEEE, United States, doi:10.1109/SENSORS43011.2019.8956652, 2019 IEEE SENSORS ; Conference date: 27-10-2019 Through 30-10-2019.
- [Sun et al., 2020] Sun, J., B. Tighe and J. Zhao (2020), Tuning the Energy Landscape of Soft Robots for Fast and Strong Motion, in *2020 IEEE International Conference on Robotics and Automation (ICRA)*, pp. 10082–10088, doi:10.1109/ICRA40945.2020.9196737.
- [T. Iwatsubo, 1972] T. Iwatsubo (1972), Stability and non-stationary vibration of columns under periodic loads.
<https://www.sciencedirect.com/science/article/pii/0022460X72905640#!>

- [Tony R. Kuphaldt, 2006] Tony R. Kuphaldt (2006), Lessons In Electric Circuits Vol. I - Direct Current (DC).
<https://www.allaboutcircuits.com/textbook/direct-current/chpt-9/strain-gauges/>
- [University of Twente, 2020] University of Twente (2020), portwings.
<http://www.portwings.eu/>
- [Verma et al., 2015] Verma, G., V. Verma and S. Jhambhulkar (2015), Design of a lead-lag compensator for position loop control of a gimbaled payload, pp. 394–399, doi:10.1109/SPIN.2015.7095358.
- [vlab.amrita, 2011] vlab.amrita (2011), *Free Vibration of a Cantilever Beam with a Lumped Mass at Free End*, Pearson Education, Incorporated.
vlab.amrita.edu/?sub=3&brch=175&sim=1078&cnt=1